SEARCH FOR NEW PHYSICS IN THE EXCLUSIVE DELAYED $\gamma + \not{E}_T$ FINAL STATE IN $P\bar{P}$ COLLISIONS AT $\sqrt{S} = 1.96$ TEV

A Dissertation

by

ADAM JUDE AURISANO

Submitted to the Office of Graduate Studies of
Texas A&M University
in partial fulfillment of the requirements for the degree of

DOCTOR OF PHILOSOPHY

Approved by:

Chair of Committee,	David Toback
Committee Members,	Bhaskar Dutta
	Teruki Kamon
	Sherry Yennello
Department Head,	George Welch

December 2012

Major Subject: Physics

ABSTRACT

This dissertation presents a search for heavy, long-lived, neutral particles that decay to photons in proton anti-proton collisions with a center of mass energy of 1.96 TeV at the Collider Detector at Fermilab (CDF) experiment. Such particles are typical of models of Gauge Mediated Supersymmetry Breaking (GMSB). We select events with a single photon, missing transverse energy, and little other activity in the detector. We model the photon arrival time for Standard Model and non-collision sources using a data-driven method and consider photons which have a time of arrival at the detector which is significantly delayed relative to predictions. Using 6.3 fb^{-1} of data collected from December 2004 to June 2010, we observe 322 events in the signal region compared to a background prediction of 287 ± 24 events. While the data are consistently above predictions, we report a model excess with a significance of 1.2 standard deviations from the null hypothesis.

ACKNOWLEDGEMENTS

Many people have helped me along my way toward finishing this research, and I owe them all my deepest thanks. All accelerators are delicate machines which contain immense energy stored both in their magnets and in the circulating beams. Countless technicians, engineers, and accelerator physicists designed, built, and maintained the Fermilab accelerator complex. Their tireless efforts kept the Tevatron running amazingly well to provide the proton antiproton collisions necessary to study this final state. Similarly, the detector, CDF, which collected the data used here is the work of far too many people to mention here; however, their work allowed it to continue taking high quality data for decades.

This analysis was unusually difficult and complex, and there were many times when it was not clear how we would finish it. Without Dave Toback, my advisor and committee chair, it is likely it never would have been finished. His willingness to boldly pursue interesting physics no matter how hard is an inspiration to me. I truly enjoyed our long phone calls in which we struggled with each new set of confusing results.

I must also recognize a number of graduate students and post-docs who were indispensable in completing this analysis. Maxim Goncharov started all of this off by being the first to look at this final state. Jonathan Asaadi worked on this project with me from the beginning, and I will never forget the long nights at Fermilab with the two of us trying to see how we would ever finish. This analysis is as much his as it is mine. Two post-docs in the Texas A&M group, Daniel Goldin and Jason Nett, also contributed invaluable work which sped up this analysis considerably.

Finally, I have to thank my family. My parents, Maria and Richard, made me

who I am today, and they have been constant sources of encouragement. When I was not sure that I wanted to continue, they reminded me why I started in the first place. My brother, David, taught me to have strong convictions and to never be afraid of an argument. Last, but certainly not least, I must thank my wife, Jillian. She has always been my biggest cheerleader. She is my best friend and an inspiration.

TABLE OF CONTENTS

LIST OF FIGURES

LIST OF TABLES

1. INTRODUCTION

The current best understanding of fundamental particles and their interactions is known as the Standard Model of particle physics (SM) [1]. In the decades since it has been proposed, the SM has been extraordinarily successful. In fact, the last particle in the SM, the Higgs boson, may have recently been observed at the Tevatron [2], and the LHC [3].

However, the success of the SM is tempered by a number of experimental results. The $g-2$ collaboration observed a possible deviation of the anomalous muon magnetic moment from the SM prediction [4]. Neutrinos have been shown to oscillate between flavors which indicates that neutrinos have mass, contrary to the prediction of the SM [5]. Perhaps most interestingly, a measurement of the cosmic microwave background by the WMAP experiment estimates that currently known particles only make up $\sim$5% of the universe's energy content [6]. A large component of the unknown energy content is believed to be due to dark matter, an entirely new sector which does not exist in the SM.

In addition, a preliminary result (not released to the public) from the Collider Detector at Fermilab (CDF) [7] that considered the production of new particles in proton antiproton collisions showed an excess of events with a single photon and nothing else where the photon appears to arrive at the face of the detector surrounding the collision a few nanoseconds later than expected. Since the resolution of the timing measurement could not explain this excess, and it was statistically significant, this dissertation seeks to understand this excess and determine whether it is evidence of new physics or can be explained by a systematic misunderstanding of the analysis of the data. Before describing the final analysis that emerged, we begin by

discussing the theory that motivated the original analysis, which will act as a guide for this analysis. We will then give an overview of how delayed photon searches are performed, and show results which inspired this search.

1.1 Theory

If the discovery of the Higgs boson is confirmed, it validates a key prediction of the SM and electroweak theory [1]; however, its existence with a small mass is one of the primary reasons to believe that there must be physics beyond the SM. To quickly summarize, we note that, as discussed in Reference [8], the Higgs mechanism dynamically generates mass by acquiring a non-zero vacuum expectation value (VEV) at the minimum of its potential $V = m_H^2|H|^2 + \lambda|H|^4$ where H is the Higgs field, m_H is the Higgs mass, and λ is the quartic Higgs coupling. This corresponds to a VEV of $\langle H \rangle = m_H^2/2\lambda$. For electroweak theory to be consistent with experimental measurements, $\langle H \rangle$ must be $\sim$174 GeV, which corresponds to m_H^2 on the order of $-(100\text{ GeV})^2$.

However, m_H^2 gets quantum corrections for every particle it couples to, even indirectly. For instance, for a fermion that couples to the Higgs with strength λ_f, the leading correction to the Higgs mass from that fermion is given by $\Delta m_H^2 = -\frac{|\lambda_f|^2}{8\pi^2}\Lambda_{UV}^2$ where Λ_{UV} is the ultraviolet cutoff scale. The ultraviolet cutoff allows the calculation to be finite and is assumed to come from new, but unspecified, physics at a higher scale. If that scale is the Planck scale ($\mathcal{O}(10^{19})$ GeV), the energy at which gravity is thought to become important quantum mechanically, the correction terms can be $\sim$30 orders of magnitude bigger than what is consistent with the $\sim$125 GeV observation [8] without the addition of an ad-hoc counter-term tuned to cancel these corrections. The fact that the Planck scale is so large compared to the electroweak scale is known as the "hierarchy problem".

Since it is unlikely that the Planck scale provides the ultraviolet cutoff, people have considered other options for reducing the divergence in the Higgs mass. While it has been proposed that the role of the Higgs be played by composite particles [9], the most common solution, favored theoretically, is the introduction of a new symmetry to cancel of terms in the Higgs mass correction.

1.1.1 Supersymmetry

Supersymmetry (SUSY) provides just such a set of cancellation terms to deal with the hierarchy problem [8, 10]. SUSY posits the existence of an operator in nature which converts a bosonic state into a fermionic one (and vice-versa) approximately doubling the number of fundamental particles from what is contained in the SM. Since, in the calculation of the Higgs mass correction terms, contributions due to virtual boson loops and virtual fermion loops have opposite signs, this symmetry can straightforwardly cancel the quadratic divergence in the mass corrections.

Irreducible representations of the SUSY algebra are called supermultiplets, and the fermionic and bosonic members of a supermultiplet are called superpartners of each other. The superpartners of SM fermions are scalars known as sfermions, and the superpartners of SM gauge bosons are known as gauginos. The model containing the minimal set of new SUSY particles is called the minimal supersymmetric Standard Model (MSSM). The MSSM is minimal because each SM fermion chiral state is partnered with a scalar sfermion in exactly one chiral supermultiplet, and each vector boson is partnered with a spin-1/2 gaugino in exactly one gauge supermultiplet.

Quarks and leptons have spin-0 partners called squarks ($\widetilde{q}$) and sleptons ($\widetilde{l}$). Gluons have spin-1/2 partners called gluinos ($\widetilde{g}$). The Higgs sector becomes more complicated in SUSY. Instead of a single particle, there must be at least two complex Higgs doublets to prevent electroweak gauge anomalies [8]. Before electroweak

symmetry breaking, the Higgs doublets are $H_u = (H_u^+, H_u^0)$ and $H_d = (H_d^0, H_d^-)$, and the electroweak gauge bosons are B^0, W^0, and $W^\pm$. The partners of these are the higgsinos ($\widetilde{H}_u^0$, $\widetilde{H}_u^+$, $\widetilde{H}_d^0$, $\widetilde{H}_d^-$) and the electroweak gauginos ($\widetilde{B}^0$,$\widetilde{W}^0$, and $\widetilde{W}^\pm$). After electroweak symmetry breaking, we get four scalar Higgs particles ($H^\pm$, h_0, and H_0) and one pseudoscalar Higgs particle (A_0), and the electroweak gauge bosons (γ, Z^0, and $W^\pm$). The charged higgsinos and gauginos mix to form mass eigenstates known as charginos ($\widetilde{\chi}_1^\pm$, $\widetilde{\chi}_2^\pm$) and the neutral higgsinos and gauginos mix to form mass eigenstates known as neutralinos ($\widetilde{\chi}_1^0$, $\widetilde{\chi}_2^0$, $\widetilde{\chi}_3^0$, $\widetilde{\chi}_4^0$), where the subscript indicates the mass ordering from lowest to highest. In some models, the graviton is included. In those models, its partner is the spin-3/2 gravitino ($\widetilde{G}$).

The most general supersymmetric theories allow terms which violate baryon or lepton number, which would allow proton decay. Since experimental evidence puts the lower bound on the lifetime of the proton between 10^{31} and 10^{33} years depending on the decay channel [11], if SUSY is correct, there must be some new mechanism that suppresses these terms. A common way is to assume a new conserved quantity called "R-parity". This is defined as $R = (-1)^{3(B-L)+2s}$ where B is baryon number, L is lepton number, and s is spin [8]. All SM particles and Higgs bosons have even R-parity while all supersymmetric particles have odd parity. Phenomenologically, this means that the lightest supersymmetric particle (LSP) is stable, and supersymmetric particles are always produced in even numbers at colliders. In some models, R-parity allows the LSP to provide a dark matter candidate [8].

If SUSY were a perfect symmetry in nature, superpartners should have the same mass. Since this is not observed [12], the symmetry must be broken somehow. There are many postulated ways for this to happen. If the breaking mechanism works in such a way that maintains the cancellation of the quadratic divergence in the Higgs mass, it is known as soft symmetry breaking [8], and there are many models that do

so.

It is generally assumed that the symmetry breaking occurs in some unspecified, high energy scale "hidden sector" which has little direct coupling to the visible MSSM sector, and thus, does not play a direct role in collider experiments. This breaking is communicated from the hidden sector to the visible sector by some mediating interaction. Depending on the nature of the mediating interactions, the phenomenology of the resulting model changes, which provides ways of testing if that mechanism is correct. Several supersymmetry breaking schemes exist such as: Supergravity (SUGRA) [13], Anomaly Mediated Supersymmetry Breaking (AMSB) [14] and Gauge Mediated Supersymmetry Breaking (GMSB) [15]. No evidence exists that indicates that one of these are true in nature, although none are completely ruled out [12].

In this dissertation, we focus on GMSB because it has many advantages of its own including providing a relativistic, neutral particle which could play a role in the early universe as favored by astronomical observations [6], and automatically suppressing flavor-changing neutral currents [8]. In addition, it has a particularly interesting phenomenology involving photons in the final state at collider experiments and thus, could be a possible explanation for the observation mentioned in the beginning of this chapter.

1.1.2 Gauge Mediated Supersymmetry Breaking

Gauge mediation refers to the mechanism of transmitting supersymmetry breaking to the MSSM through ordinary gauge interactions. For more detail, see Reference [8, 15]. This is done by adding new chiral supermultiplets called "messengers" which couple to the source of supersymmetry breaking in the hidden sector while also indirectly coupling to MSSM particles through gauge interactions.

Due the breaking of supersymmetry, there must be a Nambu-Goldstone particle called the goldstino [8]. When the breaking occurs, the supersymmetric partner of the graviton, the gravitino ($\widetilde{G}$) absorbs the goldstino as its longitudinal components and acquires mass. The mass of the gravitino can be written $m_{3/2} \sim \langle F \rangle / M_{Pl}$ where $\langle F \rangle$ is the symmetry breaking vacuum expectation value and M_{Pl} is the Planck mass. In GMSB, the symmetry breaking scale is typically low, so as long as the mass scale of the messenger particles is much smaller than the Planck mass, the gravitino is the LSP with a mass around 1 keV [8].

The $\widetilde{G}$ being the LSP is one of the hallmarks of GMSB models, and leads to particularly interesting and unique final states in collider experiments [8]. Since the $\widetilde{G}$ has gravitational strength interactions and is neutral, it will not interact much with regular matter and will leave any detector without interacting in any substantive way (similar to neutrinos). This also means that the production cross section for it in a collision of matter particles will be negligible. Thus, it will only be produced in the decays of other SUSY particles produced in collisions. However, due to R-parity conservation, if SUSY particles are created they will always decay to the $\widetilde{G}$.

Generally speaking, since the $\widetilde{G}$ has gravitational strength interactions, couplings to other particles will be very small, so decays to it will be very slow. However, the $\widetilde{G}$ also inherits non-gravitational interactions from the goldstino it absorbed allowing decay times to be faster. Typically, the $\widetilde{\chi}_1^0$ or a slepton is the next-to-lightest supersymmetric particle (NLSP) in GMSB, and the NLSP must decay to its superpartner and the $\widetilde{G}$ [8].

In the case that the NLSP is a neutralino, which is of particular interest here, if the neutralino is below the mass of the Z boson (91 GeV), its only allowed decay will be $\widetilde{\chi}_1^0 \to \gamma \widetilde{G}$. The lifetime of this decay can be written:

$$c\tau_{\widetilde{\chi}_1^0} = 48\pi \frac{m_{3/2}^2 M_{Pl}^2}{M_{\widetilde{\chi}_1^0}^5} \frac{1}{|P_{1\gamma}|^2} \tag{1.1}$$

where $m_{3/2} = \langle F \rangle / \sqrt{3} M_{Pl}$, M_{Pl} is the Planck mass, and $|P_{1\gamma}|$ is a suppression factor due to the fact that $\widetilde{\chi}_1^0$ is not the superpartner of the photon but a mixture of superpartners. Taking into account the range of allowed parameter variation, the value of $\tau_{\widetilde{\chi}_1^0}$ can range from 0.4 ns to 180 ns [16].

In some models, $\tau_{\widetilde{\chi}_1^0}$ on the order of a nanosecond is favored and can lead to striking signatures in collider experiments, which we can separate from SM final states [17]. Regardless of how the $\widetilde{\chi}_1^0$ is produced at the center of the detector, it is expected to travel from the collision point for some time (determined by its lifetime and boost) and then decay in flight to a photon and a gravitino as shown in Figure 1.1a. If the $\widetilde{\chi}_1^0$ decays inside the detector, and the photon is observed, we can measure its time of arrival and compare that to the expected time of arrival as if the photon came directly from the collision point. To separate these "delayed" arrival times from promptly produced photons, we use the variable, t_{corr}, which quantifies the time a photon arrived at the calorimeter relative to expectations a prompt photon (one coming immediately from the collision which produced it) [17]. We define t_{corr} as:

$$t_{corr} \equiv (t_f - t_i) - \frac{|\vec{x}_f - \vec{x}_i|}{c} \tag{1.2}$$

where t_f is the arrival time of the photon at the calorimeter, t_i is the time of the collision presumed to have produced the photons, and $\frac{|\vec{x}_f - \vec{x}_i|}{c}$ is the time-of-flight for the photon traveling immediately from the presumed collision point to the calorimeter. For perfect measurements, the observed value of t_{corr} for a promptly produced

photon will be zero.

However, for heavy, long-lived neutralinos these photons will have a t_{corr} value greater than zero for two reasons [17]:

- If the $\widetilde{\chi}_1^0$ is light enough, it will travel before decaying, and the true total path length of the neutralino-photon pair is much longer than the path length a prompt photon would have taken.
- If the $\widetilde{\chi}_1^0$ is heavy, the speed of the $\widetilde{\chi}_1^0$ is much smaller than the speed of light.

As shown in Figure 1.1b, the t_{corr} for photons from the decay of a long-lived $\widetilde{\chi}_1^0$ tends to be exponentially distributed [17]. In a real detector, this distribution would be smeared by the resolution of the detector, which is just over half a nanosecond.

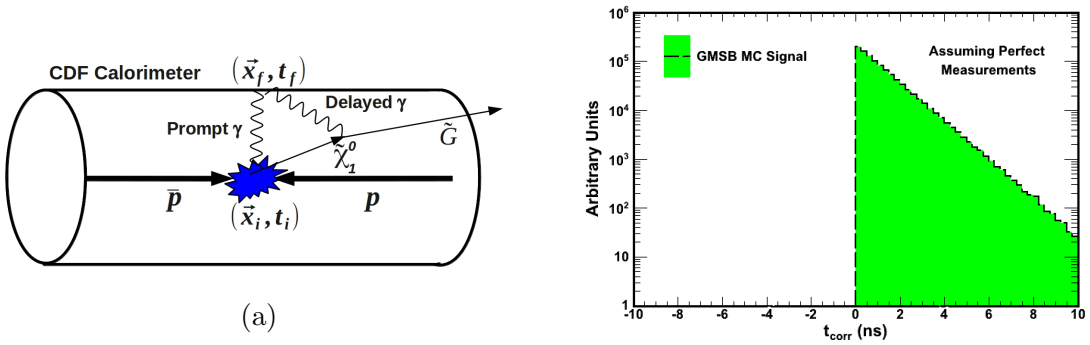

(a) (b)

Figure 1.1: Prompt photons have a measured time consistent with traveling from the collision point to the calorimeter at the speed of light. (a) Photons coming from the decay of long lived neutralinos come from a point displaced in space and time from the collision point. These photons tend to arrive late relative to expectations from prompt photons. (b) Photons coming from the decay of a long-lived $\widetilde{\chi}_1^0$ tend to be exponentially distributed [17]. This figure shows the results of a perfect timing measurement; however, in a real detector, this is smeared by the resolution of the detector.

There are two primary hallmarks of R-parity conserving models of GMSB production and decay in colliders. The first is that neutralinos must be produced in pairs in collider experiments either directly or through cascade decays of other particles. Each $\widetilde{\chi}_1^0$ decays to a photon and a $\widetilde{G}$, and since the resulting $\widetilde{G}$ do not interact in the detector, they are seen as an imbalance of energy in the transverse plane known as $\not\!\!E_T$ because of conservation of momentum. This imbalance is a typical signature in collider experiments to observe particles like neutrinos that do not interact significantly with the detector.

The second hallmark is from the photons resulting from $\widetilde{\chi}_1^0$ decays. The signature we see in the detector is highly dependent on the $\widetilde{\chi}_1^0$ lifetime. If $\tau_{\widetilde{\chi}_1^0} < 1$ ns, each $\widetilde{\chi}_1^0$ decays into a photon, and the photons appear essentially prompt within our ability to resolve. Therefore, in these states, one should look for two prompt photons and $\not\!\!E_T$. If 1 ns $< \tau_{\widetilde{\chi}_1^0} < 50$ ns, the photons can often appear late enough to be measured as delayed (many standard deviations from the predictions of promptly produced photons); however, due to the long decay time, one of the $\widetilde{\chi}_1^0$ is likely to exit the detector before decaying. Studies have shown that the optimal way to search for neutralinos in this lifetime regime is to look for a single delayed photon and $\not\!\!E_T$. If $\tau_{\widetilde{\chi}_1^0} > 50$ ns, typically both $\widetilde{\chi}_1^0$ exit the detector unobserved, and no photons are detected; therefore, we do not consider this case further.

Besides the lifetime of the $\widetilde{\chi}_1^0$, the final state depends on whether or not we expect $\widetilde{\chi}_1^0$ pairs to be produced alone or as part of a decay chain of SUSY particles. This is highly dependent on the mass hierarchy of SUSY particles, which is rigidly determined by the mechanism of SUSY breaking.

In minimal GMSB with a $\widetilde{\chi}_1^0$ NLSP, neutralinos are almost always produced at the end of decay chains leading to final states containing extra particles besides photons. This scenario is typically studied using a line in parameter space which is character-

ized entirely by the mass and lifetime of the $\widetilde{\chi}_1^0$ using a parametrization known as the SPS-8 relations [18]. In these scenarios, the production of sparticles is dominated by diagram as shown in Figure 1.2a for colliders such as the Fermilab Tevatron which collides protons and anti-protons at $\sqrt{s} \approx 2$ TeV. The presence of extra particles in the final state provides extra experimental handles which can make this type of search easier to perform; therefore, there have been many searches for this type of GMSB in the past. Searches with similar diagrams and production mechanisms have been performed at LEP [19], the Tevatron [20, 21], and the LHC [22], all with no evidence of sparticle production.

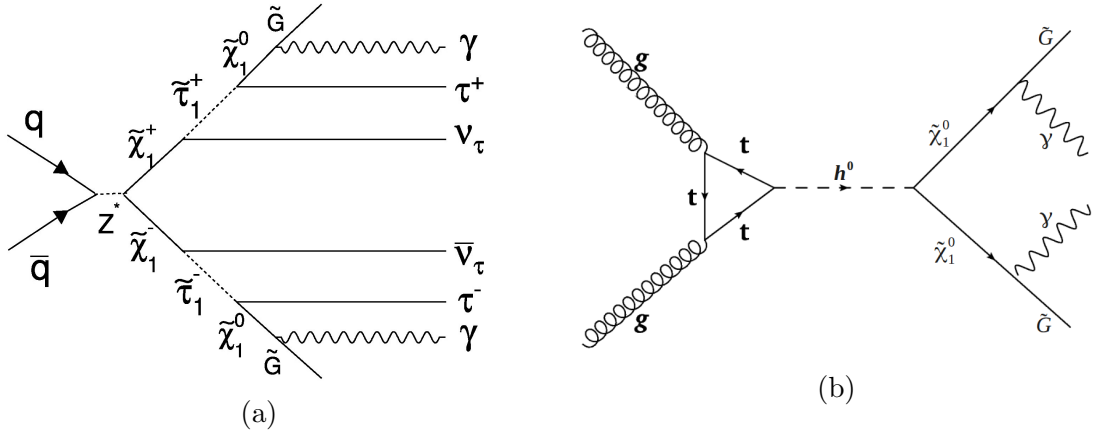

Figure 1.2: (a) Minimal GMSB models yield either $\gamma\gamma + \not\!\!E_T$ if the neutralino has a short lifetime or $\gamma_{delayed} + \not\!\!E_T$ with additional activity if the lifetime is long. (b) More general GMSB models can have sparticles only produced through the production and decay of a light higgs without associated particles. These models suggest exclusive $\gamma\gamma + \not\!\!E_T$ if the neutralino has a short lifetime or exclusive $\gamma_{delayed} + \not\!\!E_T$ if the lifetime is long.

However, since there is no evidence for these easier to observe final states of minimal GMSB models, we consider general gauge mediation (GGM) models [23]

which loosen these mass relations and allow for much more varied phenomenology. It has been found that in these models, it is possible for only the $\widetilde{\chi}_1^0$ and $\widetilde{G}$ to be kinematically accessible. These are known as light neutralino and gravitino (LNG) scenarios, and they easily evade the current experimental limits [24]. If direct pair production of $\widetilde{\chi}_1^0$ were the only option, the production cross section would be very low and unobservable with current techniques.

However, recent studies have shown that if the neutralino mass is less than half the Higgs mass, Higgs production and decay to $\widetilde{\chi}_1^0$ pairs can be significant [24]. Figure 1.2b shows production and decays in this scenario. Because the $\widetilde{\chi}_1^0$ are not produced at the end of cascade decays, there should be no additional activity in the event which makes it phenomenologically different from SPS-8-type scenarios. The final states due to $\widetilde{\chi}_1^0 \to \gamma\widetilde{G}$ decays considering SPS-8 or Higgs-type production are summarized in Table 1.1 for both the long-lived and short-lived $\widetilde{\chi}_1^0$ scenarios.

Model	$\tau_{\tilde{\chi}_1^0} \lessapprox 1$**ns**	$1 < \tau_{\tilde{\chi}_1^0} < 50$ **ns**
SPS-8 GMSB Production	$\gamma\gamma + \not\!\!E_T + H_T$	$\gamma_{\text{delayed}} + \not\!\!E_T +$ jets
Higgs-Type Production	Exclusive $\gamma\gamma + \not\!\!E_T$	Exclusive $\gamma_{\text{delayed}} + \not\!\!E_T$

Table 1.1: A breakdown of GMSB searches by lifetime as well as production model. SPS-8 refers to the Snowmass Points and Slopes model for benchmark points and parameters [18] and is dominated by $\chi_1^+\chi_1^-$ and $\chi_1^\pm\chi_2^0$ pair production. In the Light Neutralino and Gravitino (LNG) scenario [16], models where only the $\tilde{\chi}_1^0$ and $\tilde{G}$ have masses low enough to be preferentially produced in collider experiments are produced through a Higgs if the masses are kinematically favorable.

Although no limits have been set for LNG type scenarios, no evidence for short lifetime new physics was found in a previous study at CDF in the exclusive $\gamma\gamma + \not\!\!E_T$ final state [25]. Therefore, we consider LNG type scenarios with long-lived $\widetilde{\chi}_1^0$ as

described in Reference [16] using the exclusive $\gamma + \not\!\!E_T$ final state in this dissertation.

1.2 Overview of Searches for Delayed Photons

To understand how to perform a search for delayed photons from the decay of $\widetilde{\chi}_1^0$ produced in collisions between protons and antiprotons, either in SPS-8 or Higgs-type scenarios, we first must understand more about the t_{corr} variable and the characteristic shapes of the timing distributions of backgrounds. A search for delayed photons in SPS-8-like scenarios was published in 2007 [21], and we summarize the methods used there.

As previously mentioned, if we correctly identify the collision that produced the photon, it is clear from the definition shown in Equation 1.2 that any promptly produced photon will have a mean measured value of $t_{corr} = 0$ ns, but resolution effects smear out the measurement. As we will describe in more detail in Chapter 4, in our experimental apparatus, the these "right-vertex" events are well described by a Gaussian with a mean of zero and a width of $\sim$0.65 ns [26] as shown in Figure 1.3a. Photons from heavy, neutral, long-lived particles, like a GMSB $\widetilde{\chi}_1^0$, are distributed as a decaying exponential convoluted by the resolution of the detector. Figure 1.3b shows the combined distribution of right-vertex events and signal events. This strongly suggests that the ideal delayed photon search would look for photon candidates with $t_{corr} > \sim$2 ns.

Unfortunately, in collider experiments, many events contain multiple collisions, as shown in Figure 1.4a, so sometimes we do not pick the right collision. If we pick the wrong collision, the t_i and $\vec{x}_i$ we plug into Equation 1.2 have nothing to do with the collision that produced the photon. The t_{corr} distribution for this set of "wrong vertex" events is shown in Figure 1.4b and is directly related to the distribution of collisions in space and time. The end result is a broadening in the timing distribution

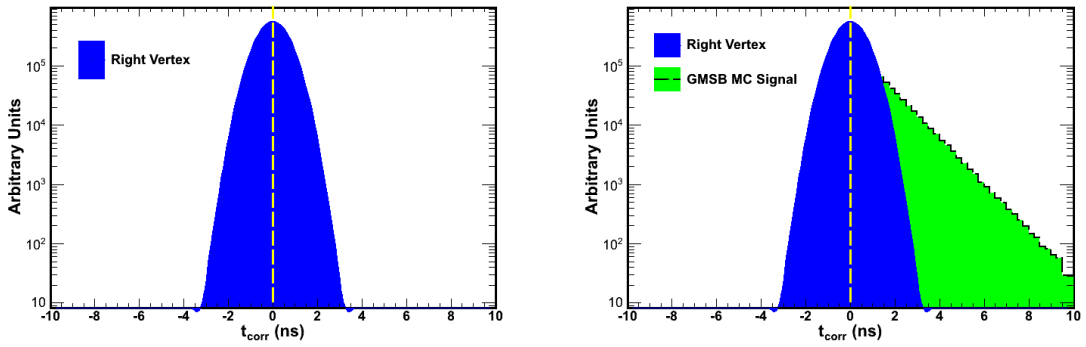

(a) (b)

Figure 1.3: (a) In a real detector, resolution effects increase the right-vertex RMS to ∼0.65 ns. (b) The expected signal distribution superimposed on the right-vertex distribution.

from ∼0.65 ns to ∼2.0 ns. This will be discussed in much more detail in Chapter 4.

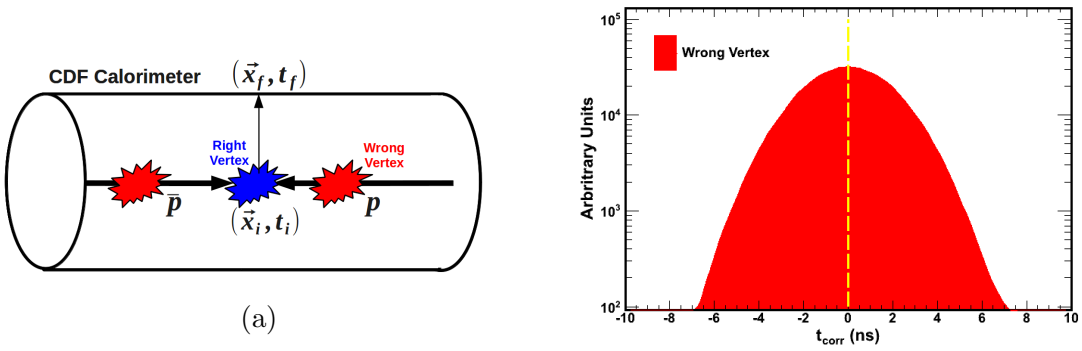

(a) (b)

Figure 1.4: (a) Many events have multiple vertices, and the right vertex is often not reconstructed. (b) If we choose a wrong vertex, the t_{corr} distribution is still Gaussian, but it has a larger width of ∼2 ns.

In addition to SM backgrounds, there are a number of non-collision backgrounds. The most important of these are events where a cosmic ray interacts with the detector

to imitate a photon in the calorimeter. Because cosmic rays originate from astrophysical sources, they are completely uncorrelated with the time structure of collisions. Therefore, they arrive randomly and have a flat t_{corr} distribution. Figure 1.5 shows background contributions from cosmic ray, right vertex, and wrong-vertex events together with a potential signal. These shapes further suggest a choice of signal region. To balance the backgrounds from regions dominated by collision and cosmic ray events, we choose a signal region of 2 ns $< t_{corr} <$ 7 ns.

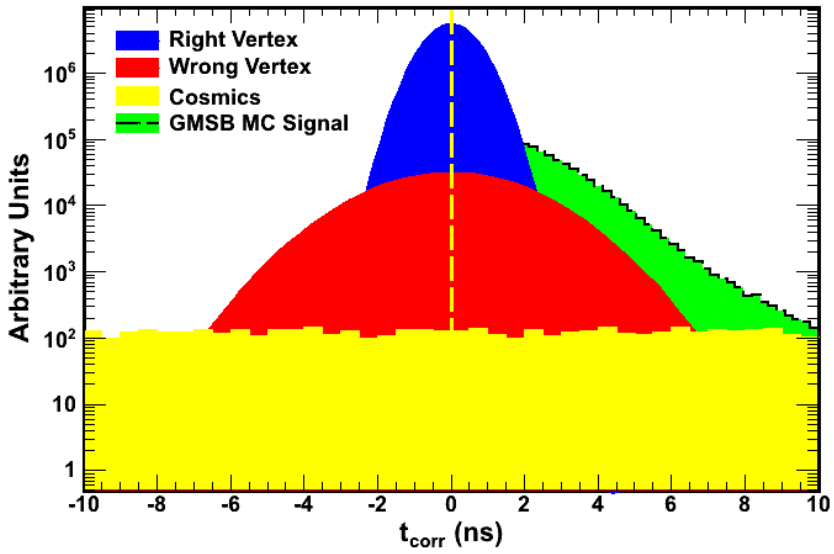

Figure 1.5: A toy description of the total t_{corr} distribution, including a potential signal.

1.3 2008 Preliminary Result

In 2008, following the suggestions of Reference [17], a preliminary analysis looking for a $\widetilde{\chi}_1^0 \to \gamma + \widetilde{G}$ signal in events with a single photon and nothing else in the first

4.7 fb^{-1} of data. The assumption was made that the t_{corr} distribution for right and wrong-vertex events was symmetric around zero as had been done in previous searches for delayed photons at CDF [21]. Using this assumption, the number of background events in the signal region, 2 ns $< t_{corr} <$ 7 ns, could be estimates from the number of events in the sideband region, -7 ns $< t_{corr} <$ -2 ns. The preliminary results are shown in Figure 1.6. Using the symmetric around zero background estimation, the analysis found 191 events in the signal region compared to an expectation of 124 events. The apparent excess of 67 events is both statistically significant, and visually striking.

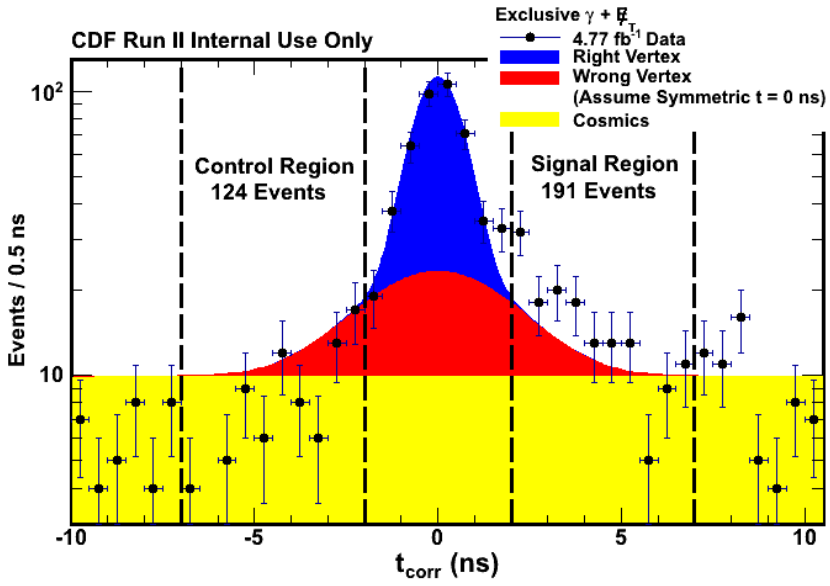

Figure 1.6: The t_{corr} distribution of events in the exclusive $\gamma + \not\!\!E_T$ final state from a preliminary analysis performed in 2008. Using the assumption that the backgrounds were symmetrical around zero, this analysis found a considerable excess of delayed photons in the region (2,7) ns. This dissertation seeks to reassess these assumptions.

Since the implications of the excess could be wide ranging, it was crucial that all

aspects of the analysis be revisited. In fact, more than any theoretical motivation, this dissertation was driven by the need to understand this result.

This analysis includes the addition of almost 50% more data to help rule out statistical fluctuations, the validation of the data to assure that it is well calibrated and free of detector artifacts, the examination of biases which could cause the backgrounds to have unusually large times, the development of ways to reduce any biases found, and the improvement of the background estimation method to account for any biases.

1.4 Outline of the Dissertation

Because this dissertation is a follow-up to an excess, we will reassess all the assumptions made in the previous analysis. We will begin in Chapter 2 by describing the experimental tools used to perform the analysis, including the Tevatron accelerator and the CDF detector. We will explain how we describe how CDF identifies the exclusive $\gamma + \not\!\!E_T$ final state and how the timing measurement is performed. Chapter 3 describes the three non-collision background sources, cosmic rays, beam halo, and satellite bunches, and new ways we have developed to reject them. Chapter 4 reassesses our understanding of SM collision backgrounds. Using many different Monte Carlo simulation and data-driven studies, we look for sources of bias which could cause collision backgrounds to have t_{corr} distribution which are not symmetric around zero or otherwise have biases towards large values of t_{corr}. We find that the mean of the wrong-vertex distribution is, in fact, generally not zero, and there are a number of effects which systematically bias t_{corr} to large values and push events into the signal region. We explain the origin of these biases and determine methods to reduce their impact. Having determined that the assumptions unpinning the old background estimation method are faulty, Chapter 5 discusses new, more robust

methods which properly estimate the background from collision events after all the new background rejection methods. We apply these new methods in Chapter 6 and validate them using Monte Carlo methods. We then use the newly validated background estimation method to produce an improved result. We conclude in Chapter 7 by summarizing the results and discussing possible future improvements.

2. EXPERIMENTAL TOOLS

In this chapter we describe the experimental tools we used to perform this analysis, including the series of accelerators at Fermilab which provide the proton and anti-proton collisions that we use to search for new physics and the detector that surrounds the collision point and records information about the collisions. We describe the methods for using the collected detector information offline to identify the particles that were produced, and measure their kinematic and other properties.

2.1 The Fermilab Accelerator Complex

The Fermilab accelerator complex is a chain of accelerators which converts hydrogen gas into high-energy beams of protons and antiprotons for use in high-energy collisions. The process begins, as described in Reference [27], when the Cockcroft-Walton pre-accelerator converts hydrogen gas to negative hydrogen ions with an average energy of 750 keV. These ions then enter a linear accelerator which further accelerates them to 400 MeV. From there, the electrons are stripped off of the ions to create protons which are feed into the first synchrotron of the accelerator chain called the Booster.

The Booster uses radio frequency (RF) resonant cavities to create an alternating electric field which accelerates the beam to 8 GeV. A useful side effect of RF cavities is called "phase focusing", where the phase of the beam is timing of the particles entering the RF cavity relative to the point in the oscillation of the electric field. If the proton enters when the field is zero, it experiences no acceleration. Similarly, if it enters early, it is decelerated, and if it enters late, it is accelerated. The net effect is to create a beam structure where particles tend to be concentrated around stable points in the RF oscillation. These concentrations of particles are known as bunches,

and the stable points in the RF oscillation, whether filled with particles or not, are known as buckets.

Proton bunches are transferred from the Booster to the next part of the accelerator chain known as the Main Injector, which serves several purposes. For example, it can accelerate protons to 150 GeV for injection into the Tevatron, or it can accelerate them to 120 GeV to be sent to the Antiproton Source where they are used in anti-proton creation. Specifically, 120 GeV protons are collided with a nickel alloy target, and from the spray of secondary particles, another system, known as the Debuncher, captures 8 GeV anti-protons and reduces the spread in momenta directions through a process called cooling. The anti-protons are then stored in a device known as the Accumulator until they are ready to be transferred into an accelerator called the Recycler which shares the same tunnel as the Main Injector and further cools and stores the anti-protons.

The Tevatron is the final accelerator in the chain, and the only one at Fermilab to use superconducting magnets. The Tevatron is filled in a number of stages, starting with protons at 150 GeV from the Main Injector. Next, anti-protons are transferred from the Recycler to the Main Injector, accelerated to 150 GeV and transferred into the Tevatron but going in the opposite direction. The Tevatron is filled with 36 bunches each of protons and anti-protons which counter-rotate within the same ring. Typically, the beam contains $\sim 3 \times 10^{11}$ protons/bunch and $\sim 8 \times 10^{10}$ antiprotons/bunch [28]. Both beams are then accelerated to 980 GeV using RF cavities operating at 53 MHz which creates buckets of length 18.8 ns. Although only buckets every 396 ns are intended to be filled, about 1% of the protons and anti-protons occupy adjacent buckets [29]. A single load of protons and anti-protons is known as a store which can remain in the Tevatron until the beam luminosity decreases to a point it is no longer useful for physics.

The beams are designed collide at two locations around the ring where the beam is focused with quadrupole magnets. These collisions occur every 396 ns with a center of mass energy of 1.96 TeV. Since the proton and anti-proton bunches have finite widths and it is not possible to focus the beams perfectly, collisions do not always occur at the center of the detector or at a fixed time. Rather, there is a distribution of collision times and positions as the bunches of protons and anti-protons pass through each other. These are approximately Gaussian distributed around the nominal collision point with a width in z (along the beam line) of $\sim$28 cm and in time with a width of $\sim$1.28 ns. There can be many interactions between protons and anti-protons in a single bunch crossing. We refer to the data collected during a single crossing as an event.

2.2 The Collider Detector at Fermilab

Around the two nominal collision points are two detectors which record information about the spray of particles created during collisions. This analysis uses data recorded by the Collider Detector at Fermilab (CDF) [7], which is shown in Figure 2.1. CDF is a general purpose detector that is azimuthally symmetric as well as symmetric about the nominal collision point, and is composed of multiple concentric sets of detectors to identify the final state particles as well as measure their 4-momentum. Like most modern collider detectors, it consists of tracking systems to measure the momentum of charged particles, calorimetry systems to measure the energy of electromagnetic and hadronic particles, and muon chambers. These detector components allow us to identify and measure the properties of particles like photons, electrons, muons, and showers of particles known as jets resulting from the hadronization of quarks and gluons.

We describe the collisions in an event, in the CDF detector using a cylindrical

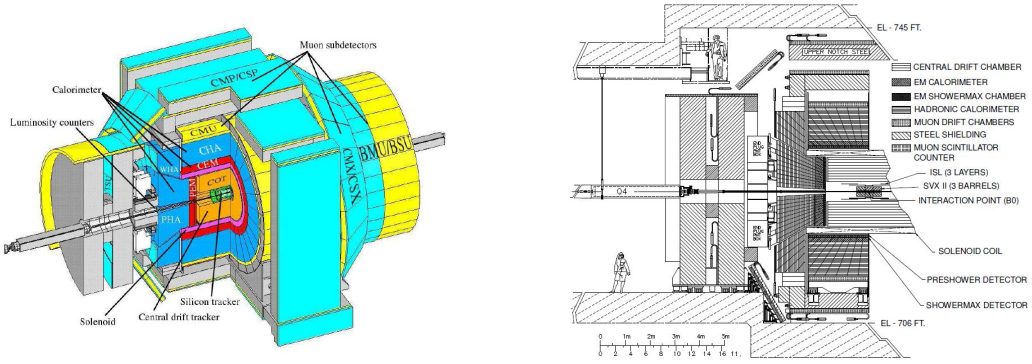

(a) (b)

Figure 2.1: Diagrams of the CDF detector: (a) isometric view and (b) elevation view. Taken from Reference [7].

coordinate system. The z-axis is defined to be the direction along the beam line, with positive z being in the direction of the incoming proton beam and z = 0 cm being at the center of the detector and the nominal collision point. The azimuthal angle is ϕ, the polar angle is θ, and the $\eta = -\ln\tan\theta/2$ is the pseudo-rapidity. The polar angle and pseudo-rapidity can be defined relative to the center of the detector or to the position of a collision (we will be explicit when using either). The transverse energy, E_T, is defined as $E\sin\theta$ where E is the energy measured by the calorimetry systems, and the transverse momentum, P_T, is defined as $p\sin\theta$ where p is the momentum measured by the tracking systems. The missing transverse energy, $\not\!\!E_T$, is a measure of the imbalance in energy in the transverse plane defined as the magnitude of the vector $\vec{\not\!\!E}_T = -\sum_i E_T^i \vec{n_i}$ where $\vec{n_i}$ is the unit vector in the transverse plane pointing to the ith calorimeter tower and E_T^i is the transverse energy of the ith calorimeter tower. While most analyses measure E_T and $\not\!\!E_T$ from the primary collision, in this analysis, we measure E_T and $\not\!\!E_T$ relative to the center of the detector for reasons to be discussed in Section 4.3.1. These variables will be identified as E_T^0 and $\not\!\!E_T^0$, respectively. We next describe the detector systems most relevant to this analysis in

more detail.

2.2.1 Tracking Systems

The tracking systems are capable of recording the trajectory of charged particles, which are used in many different parts of this analysis. For example, tracks are highly important because the presence of a track is the primary way of distinguishing a charged electron from a neutral photon that emanates from the collision. Since typical collisions produce many charged particles, tracks can be clustered to create vertices which indicate when and where a collision occurred. Because the tracking systems are embedded in a superconducting solenoid generating a 1.4 T magnetic field, charged particles travel in helical trajectories. The direction and radius of curvature allows us to determine the charge and momentum of charged particles. It is also possible to find the point of closest approach to the beam line to determine the starting position and time of origin for the particle.

The tracking system is composed of three silicon systems, Layer 00 (L00), the Silicon Vertex detector (SVXII), and the Intermediate Silicon Layers (ISL), as well as a drift chamber, the Central Outer Tracker (COT), listed in order of increasing radius. These can be seen in Figure 2.1. The silicon systems typically provide a high-precision, initial-position measurement, but not timing. The COT provides timing information and extends to a large radius, which allows for a precise P_T measurement; however, it only provides limited information about the point of origin of the charged particle. We discuss the most important systems for this analysis, SVXII and COT, here.

The SVXII is a silicon microstrip detector constructed in three 29 cm long barrels surrounding the beam line covering the range $|\eta| \leq 2.0$ [7, 30]. Each barrel contains five layers of sensors located between 2.4 cm and 10.7 cm radially from the beam

line. These layers are divided into 12 wedges in ϕ. To allow for precision measurements in z and 3-D track reconstruction, each layer is double sided. One side of all layers provides measurements in the $r - \phi$ plane while the other side provides stereo measurements. Three of the layers use 90° stereo while the other two use 1.2° stereo. Besides the five layers of sensor layers, there are bulkheads providing cabling and cooling at the boundaries between barrels, and at a radius of 14.1 cm, there is a layer of port cards which are in charge of initializing, controlling, and reading out the silicon sensors. We will see that these structures are important in Section 4.3.2. We note that the SVXII reads out precision position information (hits) for charged particles passing through it, but it does not read out the time of each hit. For tracks with timing information, we need information from the COT.

The COT is an open cell drift chamber surrounding the silicon detectors located between a radius of 44 cm to 132 cm [7, 31]. The length of the active region is 310 cm in Z, which covers the region $|\eta| \leq 1.0$. Individual cells consist of planes of 12 sense wires alternated with shape wires every 3.8 mm sandwiched between gold coated Mylar cathode planes. The entire chamber is filled with a mixture of argon and ethane, and as charged particles travel through a cell, the gas ionizes. The resulting electrons and ions are pulled by the electric field created by the cathode planes and shape wires. Charge collected by the sense wires is called a hit.

Each cell is arranged into concentric sets of wires known as superlayers. There are a total of eight superlayers which alternate between an axial configuration and a small angle stereo configuration. The configuration of superlayers can be seen in Figure 2.2.

Due to the geometric structure of superlayers, a charged particle can leave a pulse (hit) on a maximum of 96 sense wires. The pulses from the sense wires are read out through an amplifier-shaper-discriminator (ASD) and digitized by a time-

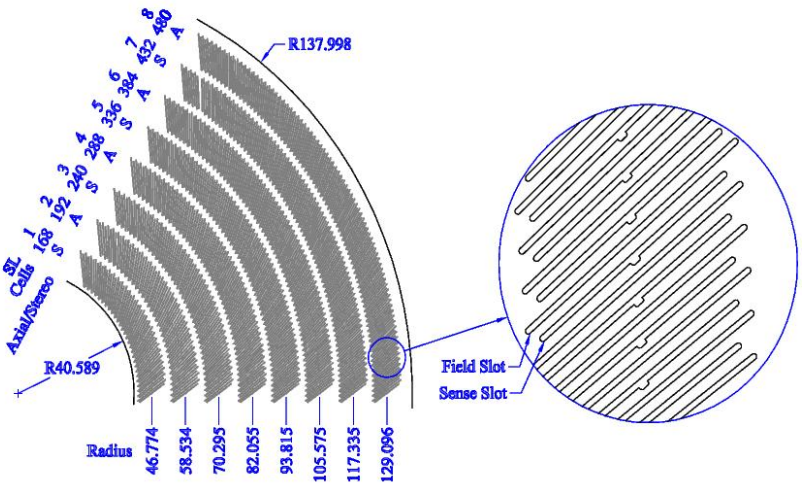

Figure 2.2: A diagram of a section of the Central Outer Tracker. Taken from Reference [7].

digital-converter (TDC). Pattern recognition software finds collections of hits with times consistent with a particle traveling through the detector and groups them into tracks. Using both axial and stereo hits, a full 3-D helix can be reconstructed which can measure the P_T with a resolution of $\sigma(P_T)/P_T = 0.15\% \times P_T$ as well as the position and time of closest approach to the beam line, with resolutions of $\sim$0.22 cm and 0.5 ns respectively.

2.2.2 Calorimeters

Outside of the tracking chambers and the solenoid lie sampling calorimeters to measure the energy of electromagnetic particles, such as electrons and photons, and hadronic particles found in jets [7, 32, 33]. These calorimeters also allow us measure the imbalance of energy, $\not\!\!E_T$, which indicates that a particle, such as a neutrino or gravitino, escaped the detector without being detected. There are five calorimeter components which cover up to $|\eta| \leq 3.64$, but we will just discuss the detectors most relevant to this analysis, the central electromagnetic (CEM) and the central hadronic (CHA) calorimeters which cover up to $|\eta| \leq 1.1$. These detectors are segmented in

a projective tower geometry pointing to z = 0 with each matched CEM and CHA tower covering 15° in ϕ and ∼0.1 in η.

Figure 2.3a shows one wedge (a collection of towers on one side of the detector in the same ϕ segment) of the CEM. The CEM is constructed of alternating layers of lead and scintillator with a depth of 18 radiation lengths. It has a resolution of $\sigma(E_T)/E_T = 13.5\%/\sqrt{E_T} \oplus 1.5\%$. Directly behind the CEM, the CHA is composed of alternating layers of steel and scintillator with a depth of 4.7 interaction lengths. It has a resolution of $\sigma(E_T)/E_T = 50\%/\sqrt{E_T} \oplus 3\%$. In both cases, the light from the scintillators is read out by two photo multiplier tubes (PMT) per tower which produce an analog voltage pulse with the total charge sent proportional to the energy deposited in the calorimeter. This pulse is integrated to determine the energy deposited in the tower.

Embedded six radiation lengths (184.15 cm) into the CEM is a proportional strip and wire chamber (CES) which measures the electromagnetic shower position and distribution at shower maximum. For each wedge, the chamber consists of 128 cathode strips oriented perpendicular to the beam line and 64 anode wires oriented parallel to the beam line as shown in Figure 2.3b. In local coordinates of Z (along the beam line) and X (the distance in the azimuthal direction along the face of the chamber at shower maximum) the CES measures the shower position with a ∼2 mm resolution. The energy of the shower is measured with a resolution of $\sigma(E)/E = 0.23$ [34].

2.2.3 EMTiming

Crucial to this analysis is the EMTiming system [26] which measures the time of arrival of particles to the electromagnetic calorimeter, the quantity t_f in Equation 1.2. Since this analysis only considers photons in the central region, we will only describe

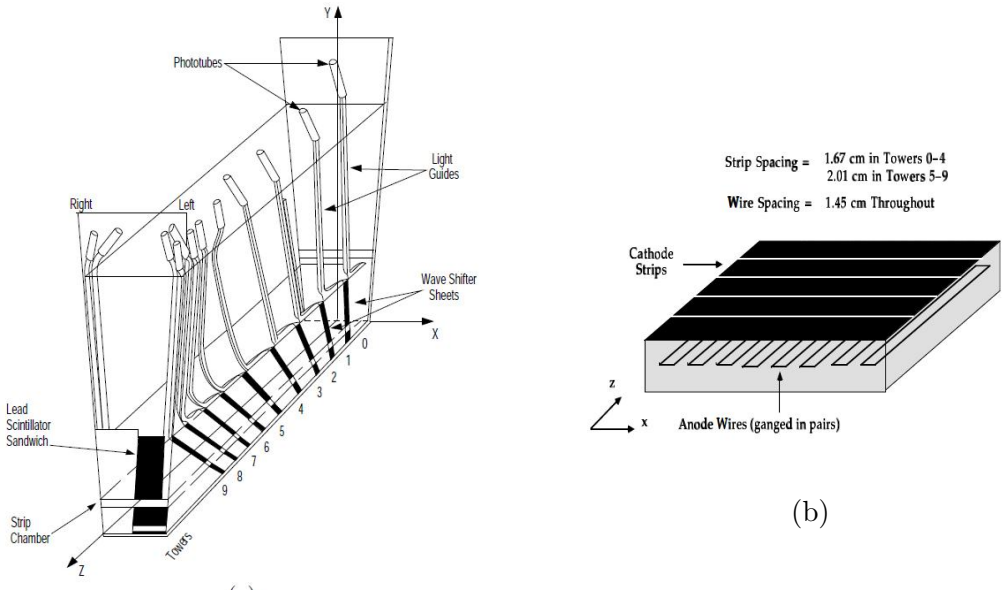

(a) (b)

Figure 2.3: (a) A diagram of a central electromagnetic calorimeter (CEM) wedge. (b) A diagram of the CES, a fine grained detector embedded in the CEM at shower maximum. Taken from Reference [7].

the configuration of EMTiming for the CEM. The PMT bases in the CEM only have one output, so an inductive splitter is used to route ∼15% of the pulse's energy for use in the timing measurement. This signal is fed into a custom ASD which combines the signal from the two PMTs reading out a single tower. If the combined pulse exceeds a fixed height, the ASD emits a 70 ns width monostable pulse which is then digitized by a TDC. Figure 2.4 shows a schematic of the data flow through EMTiming hardware. In the CEM, the EMTiming system is fully efficient for photons or electrons with energies about 6 GeV and has a resolution of ∼0.6 ns.

2.2.4 Muon Detectors

Because muons are highly penetrating particles, muon detectors [7] are placed at a radius outside the calorimeters. Typically, all hadronic or electromagnetically interacting particles have been absorbed by the time they reach these chambers. All

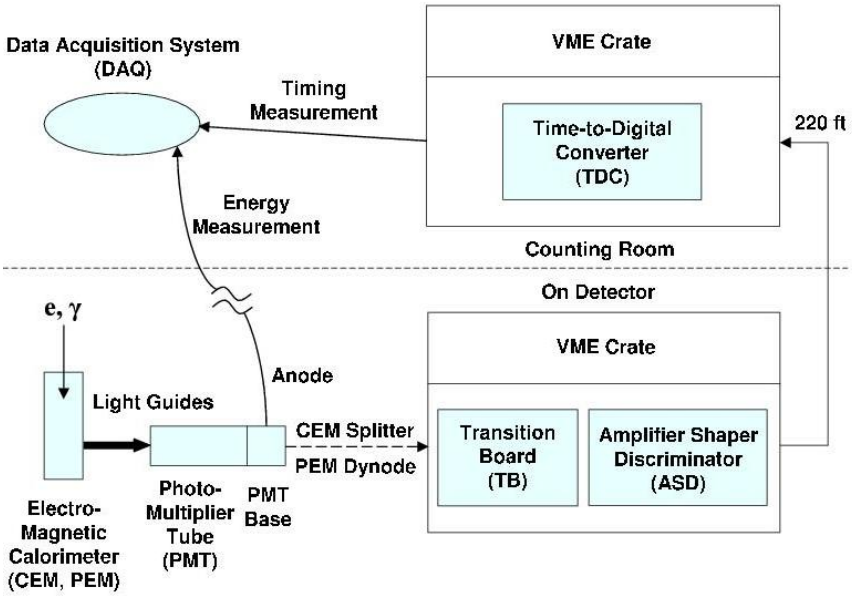

Figure 2.4: A schematic of the EMTiming system hardware. Taken from Reference [26].

the muon systems at CDF are composed of wire proportional chambers. Immediately outside the CHA is the CMU detector, which is composed of chambers arranged in a barrel configuration. These cover $|\eta| \leq 0.6$ and can detect muons with a minimum P_T of 1.4 GeV. At a further radius, outside the steel of the magnet return yoke, is the CMP, which is composed of chambers in a box configuration. These also cover $|\eta| \leq 0.6$, and the extra steel provides additional rejection against fake muons but is limited to detecting muons with a minimum P_T of 2.2 GeV. The CMX is composed of chambers in a conical configuration covering $0.6 \leq |\eta| \leq 1.0$. The BMU is composed of chambers mounted outside toroids and cover $1.0 \leq |\eta| \leq 1.5$. Since these chambers have slow drift times compared to the time between bunch crossings, scintillator tiles were added to cover the outside surface of the CMP, CMX, and BSU. Additional tiles were added to the inner surface of the toroids.

While we will not identify muons from the collision in the analysis, the muon

chambers are readily employed to reduce the rate of finding reconstructed photons which are due to cosmic ray muons. When a muon passes though a muon chamber, it leaves a series of pulses which are reconstructed as a "stub". Normal muons produced in collisions are identified by extrapolating a track from the tracking chamber out to match a stub; however, cosmic ray muons, which travel from outside the detector in, often do not produce a track. Therefore, we only look for a stub close to a reconstructed photon.

2.3 Data Acquisition and Triggers

Because beam crossings occur every 396 ns, the maximum event rate is $\sim$2.5 MHz; however, events can only be written to permanent storage at a rate of 30 to 50 Hz. The goal then becomes to sift through incoming data and quickly select the most interesting events. To do this, CDF uses a three level "deadtimeless" trigger system [7], as shown in Figure 2.5. All detector systems store their data in front-end electronics which contain a 42 bunch crossing pipeline. The front-end cards forward a small subset of their data to the Level 1 trigger implemented in custom hardware. Level 1 reduces the event rate to $\sim$40 kHz. Each decision is sent to the front-end cards by the time the event reaches the end of the pipeline. If it accepts the event, the front-end cards send more data to one of four Level 2 buffers implemented in custom hardware. Level 2 operates asynchronously and reaches a decision on average after 20 μs to further reduce the event rate to 300 Hz. If Level 2 accepts the event, the front-end cards are instructed to forward the full event data to a Level 3 node. Level 3 is implemented in software run on a CPU farm that assembles and analyzes the full event data. This reduces the event rate to 30 to 50 Hz, and every event accepted by Level 3 is written to disk for offline analysis. The system minimizes deadtime in the sense that almost no events are thrown out without at least a subset

of the full data being examined.

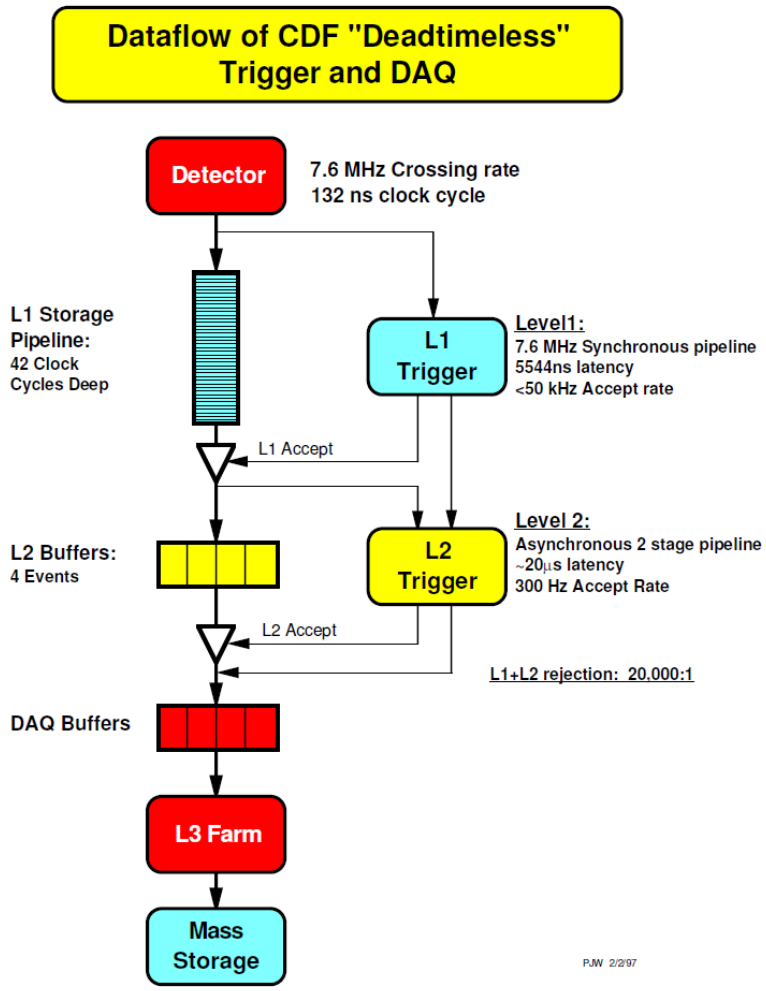

Figure 2.5: A diagram describing the data acquisition system (DAQ) at CDF. Multiple levels of triggers allow the data rate to be reduced while still retaining the most interesting events. Taken from Reference [7].

Each trigger level has a list of categories of events which, if all requirements were satisfied, would result in the event being forwarded to the next level. Each of these categories is known as a trigger. The events used in this analysis are those

which pass the set of triggers listed in Table 2.1. The primary trigger is known as "WNOTRACK," and it requires only that there be at least one energy deposit in the calorimeter with primarily electromagnetic energy and a significant amount of $\not\!\!E_T$. This trigger was originally intended as a backup route to accept $W \to e\nu$ events where the electron track was not reconstructed because of a tracking failure. This makes it an excellent monitoring trigger for tracking, but it is also highly efficient for collecting $\gamma + \not\!\!E_T$ candidates. It is particularly useful for us since it does not make a requirement on the shower shape in the CES, $\chi^2_{\rm CES}$. This variable is intended to reduce $\pi^0 \to \gamma\gamma$ backgrounds by looking for CES clusters with unusually broad shapes, but it has been found to cause problems for identifying photons with large incident angles (such as delayed photons) [21]. To enhance our trigger efficiency, we also allow events which pass any of the full set of triggers listed in Table 2.1.

The data used in this analysis was collected from December 2004 (when the EMTiming system was commissioned) to June 2010. In addition to the trigger requirements, we only accept events from runs which contain at least 100 $\rm nb^{-1}$ of integrated luminosity (so that there is sufficient statistics to calibrate the detector for each run) and for which all the necessary detectors (CEM, CES, COT, SVX, muon systems, and EMTiming) were fully functional. After all these requirements, the datasets listed in Table 2.2 contain an integrated luminosity of $(6.3 \pm 0.4)\rm fb^{-1}$.

2.4 Object and Event Reconstruction

Data as read out from the detector is simply a series of hits in the tracking chambers, muon chamber, and integrated charge pulses in the calorimeters For any physics analysis, the first step is to infer what particles created the detector output. This process is known as event reconstruction, and both online in the trigger as well as offline, during reconstruction, high level objects are created. We next describe the

Object Type	Trigger		
	Level 1	**Level 2**	**Level 3**
WNOTRACK			
EM cluster	≥ 1 Central EM cluster $E_T^0 > 8$ GeV $\frac{E_{\rm Had}}{E_{\rm EM}} < 0.125$	$\lvert\eta\rvert < 1.1$ $E_T^0 > 20$ GeV $E_T^{\rm SeedTower} > 8$ GeV	≥ 1 EM cluster $E_T^0 > 25$ GeV $\frac{E_{\rm Had}}{E_{\rm EM}} < 0.125$
Missing E_T	$\not\!\!E_T^0 > 15$ GeV $\Sigma E_T^0 > 1$ GeV		$\not\!\!E_T^0 > 25$ GeV
WNOTRACK NO L2			
EM cluster	≥ 1 Central EM cluster $E_T^0 > 8$ GeV $\frac{E_{\rm Had}}{E_{\rm EM}} < 0.125$		$\frac{E_{\rm Had}}{E_{\rm EM}} < 0.125$
Missing E_T	$\not\!\!E_T^0 > 15$ GeV		$\not\!\!E_T^0 > 25$ GeV
SUPERPHOTON70			
EM cluster	≥ 1 Central EM cluster $E_T^0 > 10$ GeV	$\lvert\eta\rvert < 1.1$ $E_T^0 > 70$ GeV $E_T^{\rm SeedTower} > 8$ GeV	≥ 1 EM cluster $E_T^0 > 70$ GeV $\frac{E_{\rm Had}}{E_{\rm EM}} < 0.2$
SUPERPHOTON70 L2			
EM cluster	≥ 1 Central EM cluster $E_T^0 > 20$ GeV $\frac{E_{\rm Had}}{E_{\rm EM}} < 0.125$	≥ 1 Central EM cluster $E_T^0 > 70$ GeV $0.0 \leq \lvert\eta\rvert \leq 3.6$ $\frac{E_{\rm Had}}{E_{\rm EM}} < 0.2$	
PHOTON25ISO			
EM cluster	≥ 1 Central EM cluster $E_T^0 > 8$ GeV $\frac{E_{\rm Had}}{E_{\rm EM}} < 0.125$	$\lvert\eta\rvert < 1.1$ $E_T > 21$ GeV $E_T^{\rm SeedTower} > 8$ GeV $E_T^{\rm ISO} < 3$ GeV $\frac{E_{\rm Had}}{E_{\rm EM}} < 0.125$	≥ 1 EM cluster $E_T^0 > 25$ GeV $\rm Iso^{Total} < 2.0$ $\chi^2 < 20$ $\frac{E_{\rm Had}}{E_{\rm EM}} < 0.055$
ELECTRON70			
EM cluster	≥ 1 Central EM Cluster $E_T^0 > 20$ GeV	≥ 1 Central EM Cluster $E_T^0 > 70$ GeV $0.0 \leq \lvert\eta\rvert \leq 3.6$	$\frac{E_{\rm Had}}{E_{\rm EM}} < 0.2$
ULTRAPHOTON50			
EM cluster	≥ 1 Central EM Cluster $E_T^0 > 12$ GeV $\frac{E_{\rm Had}}{E_{\rm EM}} < 0.125$	≥ 1 Central EM Cluster $E_T^0 > 50$ GeV $0.0 \leq \lvert\eta\rvert \leq 3.6$ $\frac{E_{\rm Had}}{E_{\rm EM}} < 0.125$	$\frac{E_{\rm Had}}{E_{\rm EM}} < 0.125$

Table 2.1: Online event selection for the W_NOTRACK triggers, as well as a list of additional triggers we allow using the logical *or* of all triggers.

Period	Run Range	SAM ID	Luminosity (pb^{-1})
1-4	190851-203799	bhelbh	460
5-10	203819-233111	bhelbi	1020
11-13	233133-246231	bhelbj	660
14-17	252836-261005	bhelbk	410
18-28	261119-289197	bhelbm	3030
29-30	289273-293800	bhelap	720
Totals	190851-293800		6300

Table 2.2: Summary of the datasets used in this analysis and their luminosities. In this analysis we use a good run list which requires that the Shower Max, Central Outer Tracker, Silicon, and Muon subsystems to be operational during data taking. Moreover, we apply a unique Good EMTiming Run List that disregards runs where the EMTiming system was not functioning properly (this accounts for < 0.1 fb^{-1} reduction in luminosity). We furthermore require that all the runs within the good run lists must have an integrated luminosity ≥ 100 nb^{-1} to ensure there are sufficient statistics to calibrate over that given run period (again resulting in only a < 0.1 fb^{-1} reduction in luminosity). After these various requirements the data analyzed corresponds to an integrated luminosity of (6.3 ± 0.4) fb^{-1}, using the standard CDF luminosity uncertainty [35].

high level objects necessary to define the exclusive $\gamma + \not\!\!E_T$ final state.

2.4.1 Jets

The most basic calorimeter object is a set of neighboring calorimeter towers, each with significant energy. When such a set of towers is identified by our algorithms, we refer to this as a "cluster" of energy in the calorimeter. Many particles can produce clusters in the calorimeter. The term "jet" is typically used to describe what the spray of particles resulting from the hadronization of a high energy quark or gluon looks like. Electrons, photons, and taus can also produce clusters of energy. Following the jargon of the CDF collaboration, we refer to all clusters of energy as a jet unless they are identified as being from an electron, photon, or tau.

The standard algorithm for identifying jets at CDF is a fixed cone iterative algorithm [32]. It begins by creating a list of all towers with $E_T > 1$ GeV sorted

in descending order known as "seed towers." Clusters are then built by taking all towers within a cone around each seed tower, where the cone radius is defined as $\Delta R = \sqrt{(\eta_{tower} - \eta_{jet})^2 + (\phi_{tower} - \phi_{jet})^2}$ where η_{jet} and ϕ_{jet} are the coordinates of the best guess energy centroid value. In this analysis, we use cones of size 0.4. For each cluster, the E_T is calculated as the sum each tower's E_T, and the jet η and ϕ are calculated as E_T weighted averages. After calculation, the center of the cone is moved to the centroid value, and the clusters are rebuild. This process continues iteratively until the set of towers in each cluster converges. If two jets overlap by more than 50% during this process, they are merged. If they overlap by less than 50%, the towers are assigned only to the closer of the two jets. We list the requirements to accept a jet for this analysis in Table 2.3.

Quantity	**Selection Cut**
E_T^0	> 15 GeV
ΔR cone	0.4

Table 2.3: Requirements to select jets for use in our jet veto. Uncorrected jets are utilized; there is no η cut made. The detector accepts events out to $|\eta| \approx 3.5$.

2.4.2 Tracks

As described in Section 2.2.1, the trajectory of charged particles through the tracking chambers is reconstructed by finding a collection of tracking hits which are consistent with the helical path of a charged particle in a magnetic field. Once the pattern matching algorithm has identified these collections of hits, a fitter reconstructs the track by fitting it to the helical path. From this fit, we can extract the particle's charge, P_T, η, ϕ_0, z_0, d_0, and t_0 where ϕ_0 is the azimuthal angle at the

beam line, z_0 is the position of origin along the beam line, d_0 is the distance of closest approach in the transverse plane, and t_0 is the time of origin.

We use tracks in three different ways in this analysis. First, tracks are the primary way we distinguish between electrons and photons since electrons are expected to have a high P_T track pointing directly to a cluster in the EM calorimeter, whereas photons veto on the presence of such a track.

Second, we can use two different clustering algorithms in a manner similar to the calorimeter clustering algorithm to cluster tracks to create vertices, which are points where a collision likely occurred. One algorithm, designed for high efficiency, clusters tracks just by z_0 [36] and is the standard vertex algorithm. The other, which clusters in z_0 and t_0, is known as space-time vertexing, and it is used to distinguish between nearby collisions and gives a high quality measurement of the time and position of the collision. The requirements for tracks to be used in space-time vertexing are listed in Table 2.4. This algorithm will be discussed in more detail in Section 2.4.5.

Finally, to select events with exclusive production, events with a high P_T track are rejected. This removes events which may contain an extra electron or muon which might indicate that the event under consideration is from a known background source rather than the signal type for which we are searching. The requirements for these tracks are listed in Table 2.5. These requirements are less stringent than those used vertexing since we are only looking for evidence that production was not exclusive, and that does not require high quality measurements of z_0 and t_0.

We quickly note that the variables COTStereoSeg(5) and COTAxialSeg(5) described in Tables 2.4 and 2.5 refer to the number of stereo or axial superlayers with at least five hits. Axial hits are necessary for a good P_T measurement while stereo hits are necessary for a good z_0 measurement. The variable $T_0\sigma$ refers to the fitted uncertainty in t_0 which indicates whether or not the t_0 measurement is believable.

Quantity	**Selection Cut**
P_T	> 0.3 GeV
$\lvert\eta_{\text{track}}\rvert$	≤ 1.4
COT StereoSeg(5)	≥ 2
COT AxialSeg(5)	≥ 2
$\lvert Z\rvert$	≤ 70 cm
$\lvert d_0\rvert$	≤ 1.0 cm
$T_0\sigma$	0.2 ns $\leq T_0\sigma \leq$ 0.8 ns
$\frac{\text{COT \# HitsTotal}}{\text{COT LastLayer + 1}}$	> 0.6

Table 2.4: The requirements used to select tracks with a good timing measurement in addition to a good position measurement. Here COT StereoSeg(5) refers to the number of COT stereo segments with 5 or more hits, COT AxialSeg(5) refers to the number of COT axial segments with 5 or more hits; d_0 refers to the corrected impact parameter; $T_0\sigma$ refers to the track time uncertainty; COT # HitsTotal is the sum of COT # HitsAxial (total count of axial hits) and COT # HitsStereo (total count of stereo hits); COT LastLayer is the last layer number that is expected to be hit (since they are numbered 0-95, a 1 is added to the number of layers).

Quantity	**Selection Cut**
P_T	≥ 10 GeV
COT AxialSeg(5)	≥ 2
$\frac{\text{COT \# HitsTotal}}{\text{COT LastLayer + 1}}$	> 0.6

Table 2.5: Requirements for our track veto. We reject events with a high P_T track that passes all the requirements in this table.

Finally, $\frac{nCOTHits}{LastLayerCOT+1}$ is the fraction of hits associated with the track compared to the maximum number of hits the track geometrically could have had.

2.4.3 Photons

The process of identifying photons in the calorimeter begins by considering all the EM clusters identified by the clustering algorithms to see if they are consistent with the expectations of being a photon. Reconstructed photons begin with calorimeter clusters of at most three towers in a single wedge. We select events that contain a photon candidate where the photon passes a set of selection requirements based on standard requirements with a long history at CDF [37]. The standard requirements are designed to reject other particles which could look like a photon. We reject clusters with a high-P_T track extrapolating to it since those are likely to be electrons. Since π^0 decay to a pair of photons, we reject clusters with a second significant cluster in the CES. To reduce backgrounds from jets mis-identified as photons, we require that the sum of the P_T of tracks within a cone of 0.4 and the energy in a cone of 0.4, but not in the cluster, be small.

While Table 2.6 lists the full set of photon identification requires we use, we note that we have made a few changes to the standard requirements for this analysis. We remove the standard χ^2 comparison of the shower shape in the CES to photon candidates from the beam line since that has been shown to problematic for photons with large incident angles [21]. We also require the PMT asymmetry to be small to reject instances where the energy in the calorimeter was due to a high voltage breakdown in one of the PMTs. Finally, we add minimum requires for energy in the CES and hadronic calorimeter to reject cosmic rays. These requirements will be described in more detail in Section 3.2.

Quantity	**Selection Cut**
EM cluster E_T^0	1 cluster with $E_T^0 > 30$ GeV
Fiducial	$\lvert X_{\rm CES}\rvert < 21$ cm and $9 < \lvert Z_{\rm CES}\rvert < 230$ cm
Hadronic fraction	$\frac{E_{\rm Had}}{E_{\rm EM}} < 0.125$ $E_{\rm Had} > -0.3 + 0.008 \cdot E_{\rm T}^0$*
Energy isolation	$E^{\rm iso}_{\rm cone\ 0.4} < 2.0 + 0.02 \cdot (E_T^0 - 20.0)$
1st CES cluster energy	CES $E > 10$ GeV* CES $E/E > 0.2$*
2nd CES cluster energy (if one exists)	CES $E^{\rm 2nd} < 2.4 + 0.01 \cdot E_T^0$
PMT spike rejection	$A_{\rm PMT} = \frac{\lvert E_{\rm PMT1} - E_{\rm PMT2}\rvert}{E_{\rm PMT1} + E_{\rm PMT2}} < 0.6$*
Track Multiplicity	Number of N3D tracks either 0 or 1
Track P_T	If $N3D = 1 \rightarrow P_T < 1.0 + 0.005 \cdot E_T^0$

Table 2.6: The photon identification criteria. Note that these are standard requirements for high E_T photons, with the following exceptions (marked with a * on the above table) described in [21]: the standard $\chi^2_{\rm CES}$ cut is removed, we add a PMT asymmetry cut to reject PMT spikes, and three new cuts on $E_{\rm Had}$, CES E and CES E/E, are added to reject cosmics. Note that many of these variables (E_T^0, energy isolation, 2nd CES energy and track P_T requirement) are calculated using the photon algorithm run with $z = 0$ rather than using z of the primary vertex as they will not be well defined or biased for events where the wrong vertex is selected.

2.4.4 Electrons

We identify electrons as essentially the same as photons except we require that a high-P_T track exists that extrapolates to close to the CES cluster as listed in Table 2.7. The requirements are based on the standard set of requirements which have a long history of use at CDF [38]. A number of the requirements for electrons that differ from those for photons are due to the presence of a track. The ratio of energy to momentum compares the calorimeter measurement to the tracking measurement. Since only charged particles leave tracks, a large E/P could indicate that this is a jet with a large neutral component. The L_{shr} variable is comparison of the measured lateral sharing of energy to what is predicted given the origin point of the high-P_T track.

Quantity	**Selection Cut**
EM cluster E_T^0	1 cluster with $E_T^0 > 45$ GeV
Fiducial	$\lvert X_{\rm CES}\rvert < 21$ cm and $9 < \lvert Z_{\rm CES}\rvert < 230$ cm
Hadronic fraction	$\frac{E_{\rm Had}}{E_{\rm EM}} < 0.055 + 0.00045 \cdot E_{\rm EM}$
Energy isolation	$E^{\rm iso}_{\rm cone\ 0.4} < 0.1 \cdot E_T^{\rm EM}$
$L_{\rm shr}$	< 0.2
Track P_T and E/P	Track $P_T > 50$ GeV, if $P_T < 50$ GeV, require $E/P < 2$

Table 2.7: The electron selection requirements. Note that these are standard electron requirements, with the exception of $\chi^2_{\rm CES}$ cut, which has been removed to make it consistent with the photon ID cuts, as well as the $|\Delta x|$ and $|\Delta z|$ requirements (which are between the CES cluster variables and the extrapolated track variables).

The fact that electrons are almost the same as photons with the exception of a track provides a way to test many of our analysis assumptions in data. As we show

in Section 4.2, we can treat electrons like photons by excluding the electron track from the track clustering algorithms for creating vertices. We can then explicitly separate our sample into right and wrong-vertex events by checking whether or not the electron track matches the chosen vertex.

2.4.5 Vertices

In order to calculate t_{corr} in Equation 1.2, it is necessary to know the time and location of the collision from which the photon was produced. We estimate the time and location of the collision by clustering tracks together into what we call a vertex. As previously mentioned, the standard CDF vertexing algorithm, ZVertex, only clusters tracks based on their z_0 [36]. In cases where we do not care about collision time or the combination of two collisions at the same Z but different times, as in Section 4.3.3, this algorithm is the correct choice as it allows us to use tracks without COT information (and hence without timing information). However, when we cluster only based on z_0, it is possible for collisions which are close in z but far in t to be merged together such that the reported time is the average of two unrelated collisions.

To solve this, we use the space-time vertexing algorithm [39]. Since this is a central part of the timing calculation, we now say more about how the clustering is done. This algorithm clusters tracks based on both z_0 and t_0 using the expectation maximization algorithm [40]. To begin, we generate a list of all the tracks satisfying the requirements in Table 2.4 and order them by P_T. For the expectation maximum formalism to work, we must have a starting hypothesis to iterate from. We do this by creating a list of seed vertices from the track list. We create the first seed vertex by merging the highest P_T track with any other track within a 1.0 cm radius in z and a 0.6 ns radius in t. We then create a second seed doing the same procedure on the

remaining tracks and continuing the process until there are no other seed vertices to be created.

Once we have a list of seed vertices, we can begin the expectation maximization. To do this, we calculate the mean z and t and the covariance matrix for each vertex. This defines a multivariate Gaussian probability distribution function (pdf) for each vertex. Then, we construct pdfs for each track from the fitted z_0 and t_0 and their uncertainties. The expectation maximization formalism uses these pdfs in a two step iterative process. In the first step, if we calculate the overlap between each track and each vertex which is the probability of that particular track belonging to that particular vertex. In the second step, we use those probabilities to adjust the means and covariance matrices. We continue this process until the means do not move by more than 1%. Finally, we check to see if any pair of vertices has significant overlap. If they do, we merge them and repeat the expectation maximization loop. Once the list of vertices is finalized, we select good vertices using the requirements in Table 2.8, and we use the one with the highest ΣP_T, which is the sum of all track P_T belonging to the vertex. This choice will be discussed in more detail in Section 4.1.

Quantity	**Selection Cut**
ΣP_T	≥ 5 GeV
N_{track}	≥ 3
$\lvert z \rvert$	≤ 60 cm

Table 2.8: Table of requirements used to identify good space-time vertices. Note that only tracks found in Table 2.4 are considered.

2.5 Corrected Time Measurement and Calibration

We now have all the parts necessary to calculate t_{corr} from Equation 1.2. We measure t_f from using the EMTiming system, $\vec{x}_f$ from the CES cluster, and t_i and $\vec{x}_i$ from the highest ΣP_T space-time vertex. If no space-time vertex is found, we can still construct a version of t_{corr} relative to the center of the detector (setting $t_i = 0$ and $\vec{x}_i = 0$ in Equation 1.2) known as t^0_{corr} defined as:

$$t^0_{corr} \equiv t_f - \frac{|\vec{x}_f|}{c} \tag{2.1}$$

We note that there is significant variation in the measurement of the detector response to tracks and photons, so a large amount of calibration must be done upstream. These calibrations are described in Appendix A and in more detail in Reference [41, 42]. After all calibrations, we find a timing resolution of ∼0.25 ns for vertices and ∼0.65 ns for calorimeter clusters. A validation of the calibrations shows that the timing variation is less than 100 ps as a function of track parameters, energy, tower number, and run number.

2.6 Monte Carlo Methods and Samples

Although we can use electron data to approximate the response of the detector to events with photons and $\not\!\!E_T$, there are some background processes which we can only model using Monte Carlo simulation techniques. CDF has standard tools which account for accelerator and detector conditions [43]. To generate Monte Carlo events, we first begin with an event generator such as PYTHIA [44] or BAUR [45]. These programs are capable of simulating the production of a selected process from $p\bar{p}$ collisions and the decay and hadronization of the resulting particles. Once this has been done, GEANT3 [46] is run to simulate the interaction of these particles with

the detector. This information is used to model the response of the detector and produce simulated raw data. From this point, the simulated data is reconstructed as if it were produced by the real detector.

Unfortunately, we cannot simply use these simulations to directly model the number of events in the signal region from SM background processes since we cannot be sure how accurate the Monte Carlo is. However, we do expect the Monte Carlo to reproduce major features of the real data, which we can validate using our $e + \not\!\!E_T$ sample, so we use it to explore possible previously unknown timing biases. The Monte Carlo samples of background processes used in this analysis are listed in Table 2.9.

Process	**MC Stntuple**	**MC Generator**	**Luminosity ($\mathbf{fb}^{-1}$)**
$W \to e\nu$	`we0she, we0sge, we0sie, we0seh, we0sej`	PYTHIA	~ 11
$\gamma +$ jets	`gx0s0j`	PYTHIA	~ 24
$W\gamma \to l\nu\gamma$	`re0s68` ($e\nu\gamma$) , `re0s69` ($\mu\nu\gamma$) , `re0s6a` ($\tau\nu\gamma$)	BAUR	~ 500
$W \to \mu\nu$	`we0s8m, we0s9m, we0sam, we0sbm, we0sgm`	PYTHIA	~ 7
$W \to \tau\nu$	`we0sat, we0sbt`	PYTHIA	~ 11
$Z\gamma \to \nu\nu\gamma$	`zx0s0n`	PYTHIA	$\sim 25,000$

Table 2.9: The six MC Stntuple files used in this analysis to make our Standard Model $\gamma + \not\!\!E_T$ control samples.

Because the EMTiming system was added to the CDF detector after Run II started, it was never added to the standard detector simulation. However, it is straightforward to approximate the detector response. Standard CDF Monte Carlo samples include detector simulation information including the generated energies of particles, the time they were produced, and locations where they interacted with the detector. We take this list of particles and remove any which do not deposit significant energy in the electromagnetic calorimeter. We then iterate through each particle's trajectory through the detector and find the last location where it inter-

acted with the detector before crossing the plane of the CES. At the point of the last interaction, the detector simulation records the time, location, and velocity of the particle. We extrapolate the trajectory of the particle across the plane of the CES and calculate the time at which it crossed. This is the absolute time of arrival. We then apply a Gaussian smearing of 0.59 ns to the time of arrival to account for the measured EMTiming intrinsic resolution. This technique has been shown to accurately model the EMTiming system [47], and we will show more on this in Chapter 4.

Having described the tools necessary to perform the search for new physics in the exclusive $\gamma + \not\!\!E_T$ final state, we now turn to describing non-collision backgrounds, how to reduce their rates, and how to estimate the amount remaining.

3. NON-COLLISION BACKGROUNDS

3.1 Overview

Non-collision backgrounds are sources of $\gamma + \not\!\!E_T$ events where the reconstructed photon is not produced through the collision of protons and anti-protons that reside in the primary bunches. The most important non-collision backgrounds for this analysis are cosmic rays, which are muons produced in the atmosphere out of interactions with charged particles from outer space. Other sources, such as collisions of satellite bunches, which are collisions between protons and anti-protons in the beam not in their intended locations, and beam halo, which are particles produced by the interaction of beam particles at large radius with accelerator material upstream of the detector. Both are found to be negligible after all the requirements but are discussed here to explain the requirements used as well as the methods used to confirm their rates after all requirements.

Because of the details of how these backgrounds are produced, each background has a distinctive timing distribution. In this chapter, we discuss the origin of each of the backgrounds, how that affects its timing distribution, and how the we can model its timing distribution. We will also discuss the requirements listed in Chapter 2 that were used to reject each background.

To study the backgrounds, their timing distributions, and show the efficacy of the rejection methods, we create a set of control samples using real data that are dominated by an individual non-collision background. We begin by creating a pre-sample mainly composed of non-collision events using the criteria listed in Table 3.1 and then add extra requirements for each separate background.

Requirement	**Selection Cut**
Trigger and good run	See Tables 2.1 and 2.2
Good isolated photon	See Table 2.6
E_T^0	> 30 GeV
$\not\!\!E_T^0$	> 30 GeV

Table 3.1: The set of requirements to create the various non-collision background samples.

3.2 Cosmic Rays

Cosmic rays are electrons, protons, and nuclei of astrophysical origin which strike the Earth's upper atmosphere [12]. Cosmic rays interact in the atmosphere and create secondary showers of particles. If they have enough energy, these secondary particles can reach the surface of the Earth. Of these secondary particles, only muons and neutrinos can penetrate the ground and reach the CDF detector. For our purposes, only the muons are of interest since only they interact with the detector in an observable way.

Normally, we do not consider muons to be a large source of mis-reconstructed photons for two reasons: muons are charged particles, so the tracking chamber usually records their path; and at the energies produced at the Tevatron, muons are minimum ionizing particles which typically do not initiate a shower in the CEM [12]. However, because the rate of cosmic rays passing through our detector is high, these muons occasionally deposit a significant amount of energy in the CEM. If the muon stops in the calorimeter, or the track is not reconstructed, the calorimeter deposit can be interpreted as a photon [48]. A second source of photon candidates from cosmic ray events is when the muon radiates a high energy photon as it traverses the detector, but does so in a way that does not go through the origin, so no track is reconstruccted. If an unrelated collision creates a vertex, the cosmic ray can enter the exclusive $\gamma + \not\!\!E_T$ final state as shown in Figure 3.1

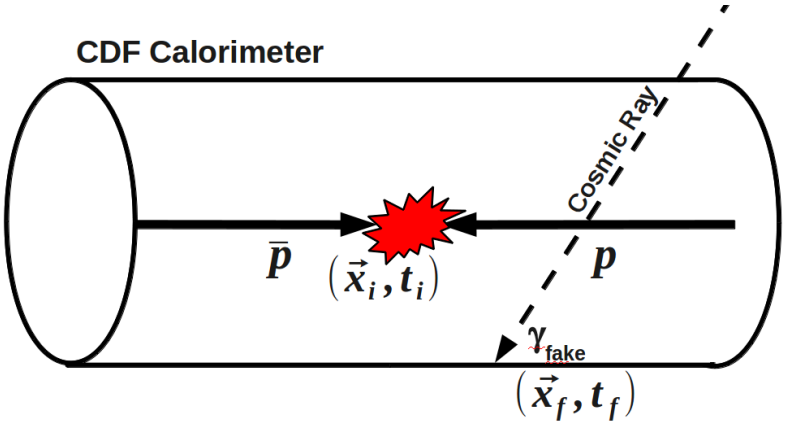

Figure 3.1: Cosmic rays enter the detector from outside and are totally uncorrelated with the beam structure. A cosmic ray can enter our sample if it interacts with the detector during the collision time window to produce a photon candidate and an unrelated collision occurs.

To study cosmic rays, we note that they arrive at our detector randomly in time, completely uncorrelated with the beam structure. Due to this, we expect to see a flat distribution of cosmic ray events in t_{corr} with the exception of turn-on and turn-off regions due to the opening and closing of the energy integration window of the calorimeter [7]. Therefore, we can create a nearly pure sample of cosmic ray induced photon events by selecting events with sufficiently large t_{corr} to avoid collision produced photons but not so large as to be in the turn-off region. Our cosmic ray control sample is defined by the requirements in Table 3.1 and the timing requirement 20 ns $< t_{corr} <$ 80 ns. Similarly, we create a collision control sample by using electron data to model photons using requirements listed in Table 3.2. Using these two samples, we can test cosmic ray rejection requirements.

Cosmic rays have been studied at CDF for many years, and there are many ways to reject them to reduce their rate and impact on our search. We use methods of photon identification as well as event topology requirements. The photon identification requirements were described in Chapter 2. Before the description of these

Requirement	**Selection Cut**
Trigger and good run	See Tables 2.1 and 2.2
Good electron requirements	See Table 2.7
E_T^0	> 30 GeV
$\not\!\!E_T^0$	> 30 GeV

Table 3.2: The set of requirements to create the $W \to e\nu \to e + \not\!\!E_T$ data control sample used to model photons from collisions. This allows us to study the difference between reconstructed photons from collision and reconstructed photons due to cosmic rays.

requirements, we note that our job is more difficult than in a typical analysis with cosmic ray backgrounds because delayed photons share some features in common with cosmic rays. Specifically, the energy deposited in the detector for photons from collisions and cosmic ray sources are different both in the main tower as well as the shower maximum detector. For this reason, many CDF searches with final state photons use the requirement that the energy distribution in the CES be consistent with the shower shape of a prompt photon (CES χ^2) which reduces the cosmic ray rate significantly. However, it has been found that this requirement is inefficient for photons with large incident angles as is possible with delayed photons [21]. Without this shape requirement, the cosmic ray rate is very large, so it is critical that we find requirements to replace it.

Before adding requirements to the photon identification, we first use event topology requirements to reduce the cosmic ray rate to $\gamma + \not\!\!E_T$ events. Previous analyses have used the fact that since cosmic rays are muons, there is often evidence for a muon passing through CDF's muon detectors (located outside the calorimetry system as shown in Figure 2.1) before or after having created a photon. Such requirements have been successfully used in several previous delayed photon analyses [21]. When a muon traverses the muon system, it leaves a series of hits known as a muon stub. We require that there be no muon stubs within 30° of the electromagnetic cluster

of the reconstructed photon. Using the cosmic ray control sample and the electron data control sample, we find that this requirement rejects ∼80% of cosmic ray events while retaining ∼95% of electrons.

After this requirement, we create two additional photon identification, requirements which take advantage of the difference between the way photons shower in the detector when then come from the center of the detector, and when photon candidates come from outside the detector in as with cosmic rays. The first requirement considers the distribution of energy in the EM and HAD calorimeters. Real photons produced in collisions initiate an electromagnetic shower which is largely contained in the EM calorimeter. However, most energetic photons do produce some energy leakage into the HAD calorimeter. Since cosmic rays often travel into the detector from outside the detector, there are a few options: if it initiates a shower in the HAD calorimeter, it will not be reconstructed as a photon, but if it initiates a shower in the EM calorimeter, it is less likely to leave a large amount of energy in the HAD calorimeter. Therefore, we require that a small amount of energy be deposited in the HAD calorimeter.

The requirement reflects the expectation that the amount of energy deposited in the hadronic calorimeter should scale with the energy of the electron or photon. We find that a cut of $E_{had} \geq -0.30 + 0.008 \cdot E_T^0$ gives us an efficiency of ∼95% for all photon energies while rejecting ∼66% of cosmic ray events as shown in Figure 3.2.

Although we cannot use the CES shower shape (CES χ^2) variable, described in Section 2.3, to reject cosmic rays, the magnitude of the energy of the deposit in the CES detector is expected to be good for all incident angles of photons from the beam line. While the energy reported in the CES is a coarse estimate of the total energy of the photon, it does track well with the total energy. Cosmic rays do not have a normally developing shower since they typically travel outside-in. If the shower is

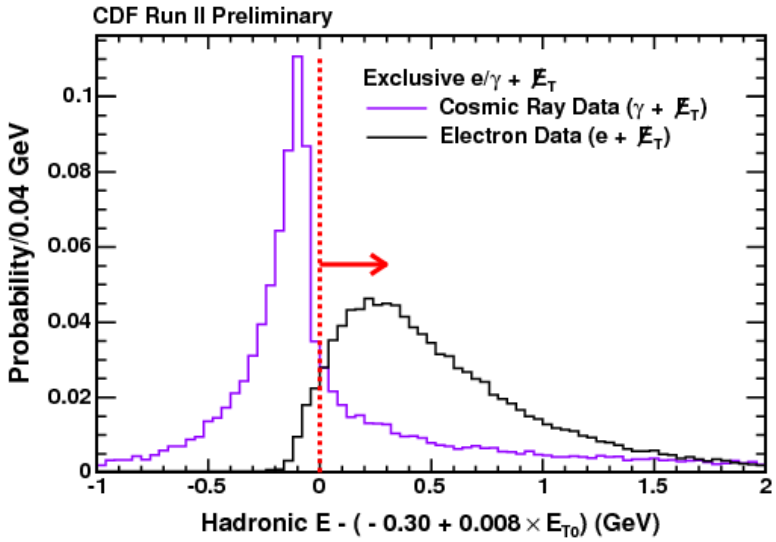

Figure 3.2: The probability of cosmic rays (purple) and electrons (black) passing the hadronic energy requirement after the application of the CES energy requirement.

initiated far from the CES, there will be little or no CES energy. To help separate cosmic rays from real photons, we require a significant amount of energy measured in the CES that scales with the measured photon energy.

We find that by requiring $E_{CES}/E_{tot} \geq 0.2$, we can reject ∼36% of cosmic ray events while retaining ∼97% of electron events as shown in Figure 3.3. The combined effect of these two new requirements allows us to reject ∼76% of cosmic ray events while retaining ∼92% of electron events. All three cosmic ray rejection requirements are summarized in Table 3.3 for completeness.

Now that we have reliable methods to reject cosmic ray events, we use these requirements to confirm our understanding of the cosmic ray timing distribution. We construct a cosmic ray enriched sample from our non-collision pre-sample by inverting the criteria in Table 3.3. In addition, we reject beam halo events using the requirements listed in Table 3.4 which will be described in Section 3.4. Figure 3.4 shows the t^0_{corr} distribution for the cosmic ray enriched sample. We confirm that the

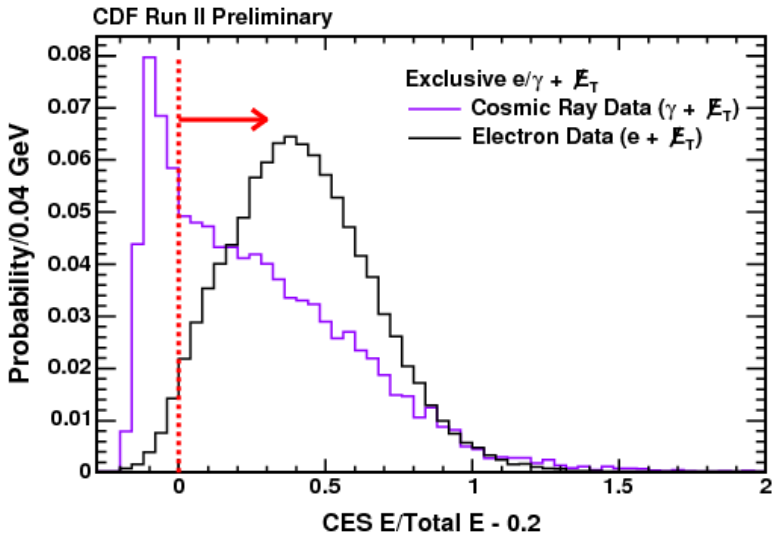

Figure 3.3: The probability of cosmic rays (purple) and electrons (black) passing the CES energy requirement after the application of the hadronic energy requirement.

Quantity	**Selection Cut**
Muon stub veto	$\Delta(\phi_{\text{stub}} - \phi_\gamma) < 30°$
Hadronic energy deposited (E_{Had})	$\geq -0.30 + 0.008 \cdot E_T^0$
Total energy in the CES	CES $E \geq 10$ GeV CES $E/E \geq 0.2$

Table 3.3: Summary of requirements used to veto photon candidates as originating from cosmic rays. Note, the hadronic energy cut and CES energy cuts are included in the photon ID variable listed in Table 2.6. We include them here in order to explain why these non-standard cuts are present in the photon ID used in this analysis. The muon stub veto is described in [21].

timing distribution is flat with the exception of the turn-on and turn-off regions discussed previously and can be reliably extrapolated into the signal region. Therefore, once we estimate the cosmic ray rate using the 20 ns $< t_{corr} <$ 80 ns region, we can estimate the cosmic ray content of any time interval by simply scaling the rate by the length of the intervals.

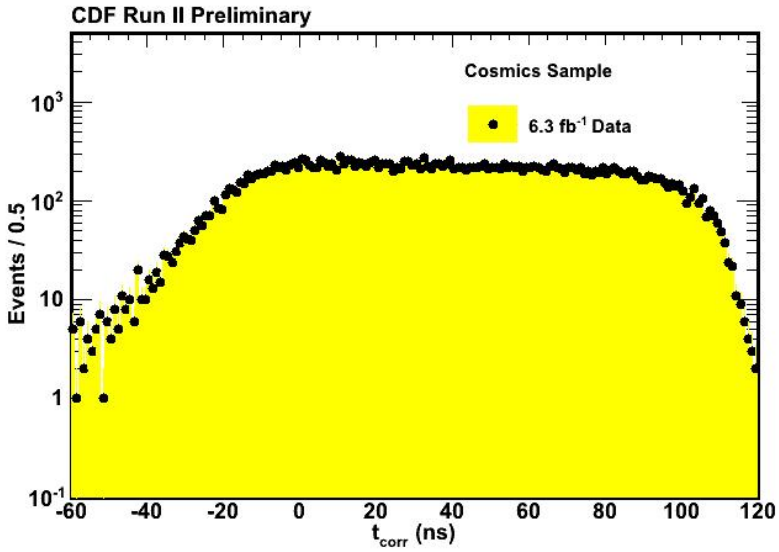

Figure 3.4: The rate of cosmic ray events is approximately flat away from the edges of the energy integration window.

3.3 Satellite Bunches

Satellite bunches are collections of protons or anti-protons which are not in their intended RF buckets, described in Section 2.1. In particular, main bunches are flanked by satellite bunches with a spacing of ∼18.8 ns. These bunches typically are ∼1% the intensity of the main bunch [29]. While these collisions can produce a fair

number of $\gamma + \not{E}_T$ events, after all requirements, they do not produce a significant number in our signal region, or in regions used to estimate background contributions in the signal region.

The expected distribution in position and time of collisions between collections of main and satellite bunches is shown in Figure 3.5 as determined by MC methods. We find that interactions between the satellite bunch and the main bunch tend to produce collision with times offset by half the radio frequency period but with very large $|Z|$. Interactions between two satellite bunches tend to produce collision with $|Z|$ near zero but with times offset by a full radio frequency period.

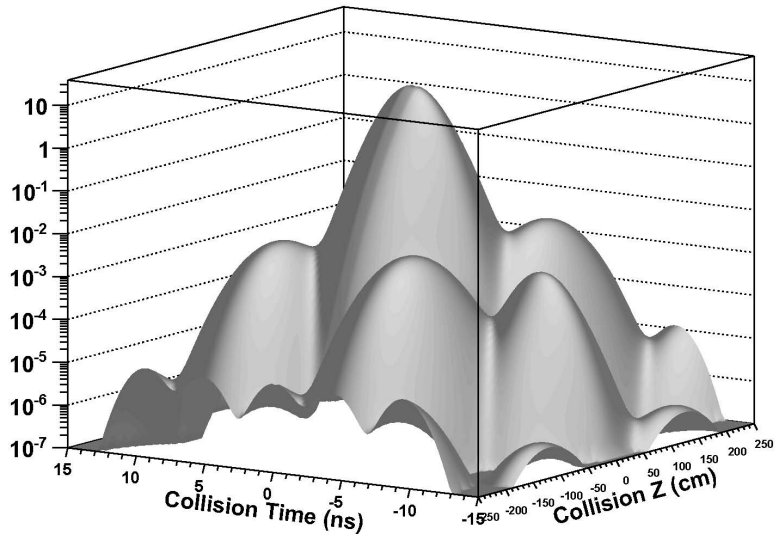

Figure 3.5: The distribution of position and times for satellite bunch collisions calculated using MC methods from the nominal shapes of bunches and the expected spacing between main and satellite bunches.

Using the same MC methods, we simulate the timing distribution of photons

produced by those collisions in the assumption that they hit the detector. The expected distribution of t^0_{corr} for photons originating in satellite bunch collision is shown in Figure 3.6. We see that satellite bunches cause peaks near ± 5 ns for main-satellite interactions and near ± 10 ns for satellite-satellite interactions.

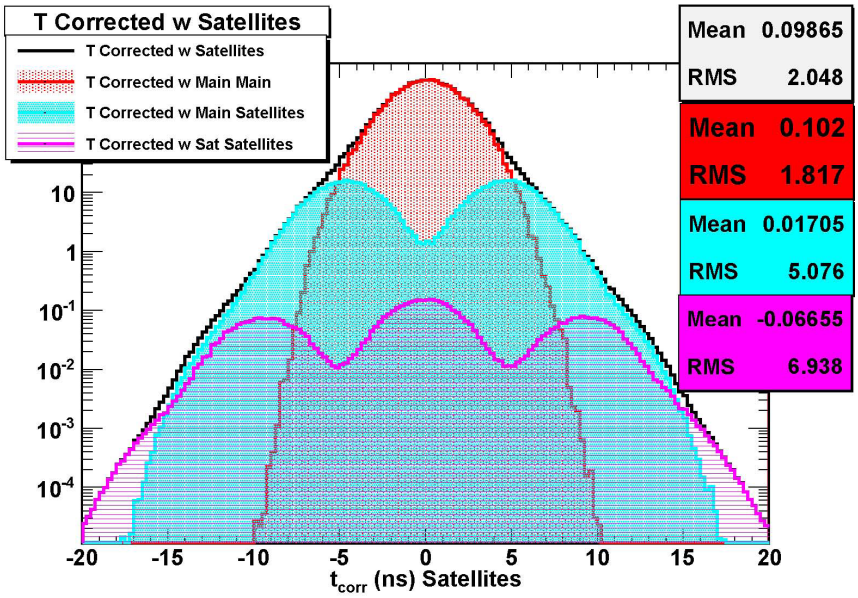

Figure 3.6: The expected t^0_{corr} distribution for satellite bunch collisions calculated using MC methods from the nominal shapes of bunches and the expected spacing between main and satellite bunches. We see that satellite bunches cause an enhancement near ± 10 ns and ± 5 ns.

With this expected timing distribution, we look for evidence of satellite bunches in the non-collision pre-sample with cosmic ray and beam halo events rejected using the criteria in Tables 3.3 and 3.4. Figure 3.7 shows the t^0_{corr} for these events after subtracting off the cosmic ray content estimated from the $20 < t^0_{corr} < 80$ ns region. The central peak is due to collision events where the vertex was not reconstructed.

From the excess at -5 ns and no matching peak at +5 ns, it is clear that satellite bunches must contribute less than 1% of collision background, especially considering contributions from beam halo are expected to contribute events to the negative side, but not the positive side, as is observed here. We do not attempt to further reduce satellite bunches, and we treat them as negligible in the final analysis.

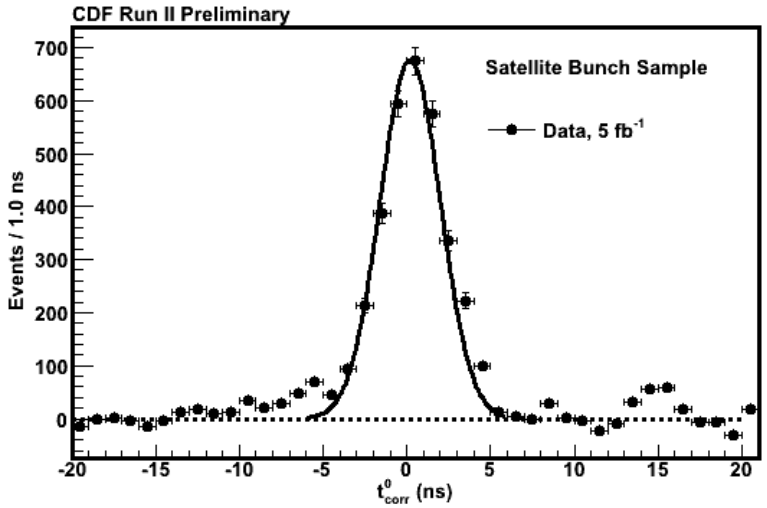

Figure 3.7: The t^0_{corr} time distribution for the non-collision pre-sample in the first 5 fb^{-1} of data with cosmic ray and beam halo events rejected. We subtract off the estimated cosmic ray content using the rate in the $20 < t^0_{corr} < 80$ ns region. Any contributions from satellite bunches are very small.

3.4 Beam Halo

Beam halo are muons produced by interactions between the beam and accelerator material upstream of the detector and which travel parallel with the beam. This has been studied in great detail and there are powerful rejection methods which are described in Reference [48]. As shown in Figure 3.8, as beam halo muons travel

parallel to the beam, and since they are at the radius of the calorimeter, they can deposit energy in the calorimeter that can be interpreted as a photon. However, they also tend to leave small amounts of energy in towers they pass through. The standard rejection methods calls for the rejection of events where towers in the same wedge as the reconstructed photon and the plug hadronic calorimeter contain energy consistent with a minimum ionizing particle. These criteria are listed in Table 3.4 and have been shown to be more than 98% efficient for real photons while rejecting nearly all beam halo events.

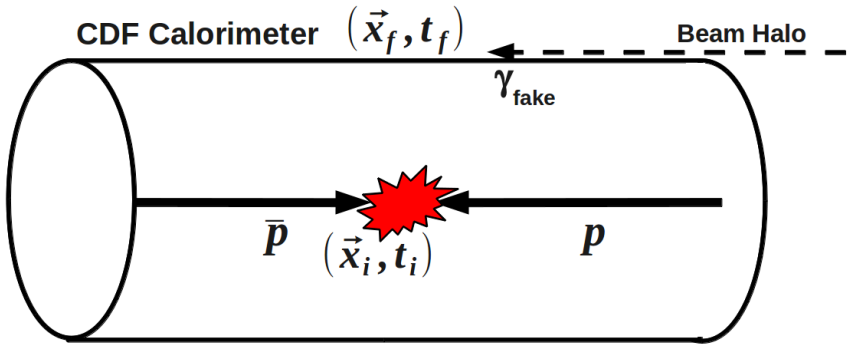

Figure 3.8: A diagram showing beam halo interactions producing events that mimic the $\gamma + \not\!\!E_T$ final state. Beam halo occurs when an interaction with accelerator material upstream of the detector creates a particle traveling in parallel is a proton or anti-proton bunch. This beam halo particle interacts directly with calorimeter.

To confirm these results and study the timing distribution of beam halo candidates, we construct a beam halo enriched sample by selecting events in the non-collision pre-sample and requiring that they pass the cosmic ray veto but fail the beam halo veto. Figure 3.9 shows the timing distribution for this beam halo en-

Quantity	Selection Cut
N towers with $E_T^0 > 0.1$ GeV in the wedge of the photon	> 8
N plug hadronic towers with $E_T^0 > 0.1$ GeV	≥ 2

Table 3.4: Summary of requirements used to veto photon candidates as originating from beam halo. These are the standard requirements as described in [21].

riched sample. Since beam halo muons travel parallel to the beam at the radius of the calorimeter, it typically arrives at the calorimeter early compared to a photon which traveled from the beam line. In fact, nearly half of all beam halo events occur in the region (-10,-5) ns. The secondary peak seen at ∼15 ns is due to beam halo caused by satellite bunches.

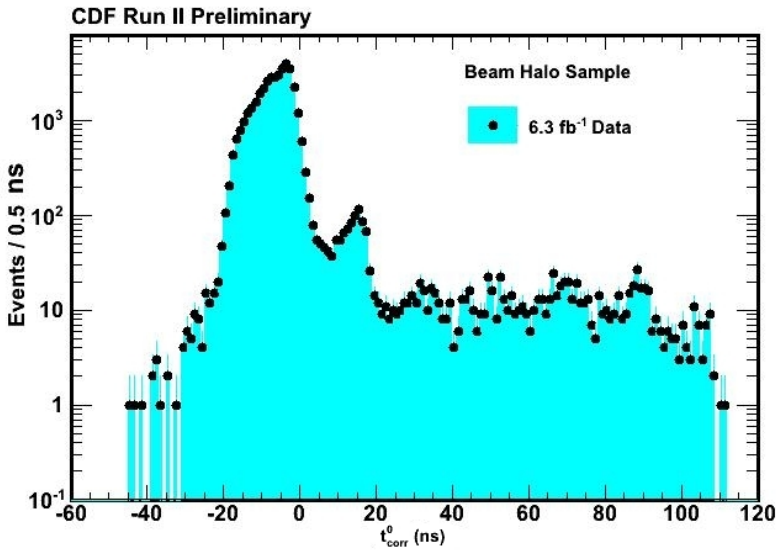

Figure 3.9: Because the beam halo particle travels with a proton or anti-proton bunch but at radius of the calorimeter, they tend to arrive earlier than a particle which had to travel from a collision.

We can use the fact that nearly half of all beam halo events occur in the region

(-10,-5) ns to estimate the beam halo content in Figure 3.7 as well as in the signal region and no-vertex data samples. Starting with the satellite sample, we see that there are ∼300 excess events in the region (-10,-5) ns, but not many events around 5 ns as would be consistent with beam halo. Assuming all these events are due to beam halo and using the distribution in Figure 3.9, we find that there should ∼100 events in the region (-3.5,3.5) ns which is ∼3% of the total events in that region. Similarly, beam halo should only contribute ∼1 event to the region (2,7) ns.

Since we estimate the mean of the wrong-vertex distribution from the mean of the no-vertex distribution, as described in Chapter 5, it is reasonable to worry about the beam halo contribution to the no-vertex sample in the region (-3.5,3.5) ns. We overestimate the contamination by estimating the no-vertex collision distribution as a Gaussian with a mean of zero and an RMS of 1.6 ns, and using the predicted beam halo distribution to determine how large of a deviation beam halo could cause in the no-vertex mean. We find that beam halo should not shift the predicted mean by more than 40 ps. Therefore, we treat beam halo as negligible in the final analysis for the no-vertex sample.

4. STANDARD MODEL BACKGROUNDS AND TIMING BIASES IN THE EXCLUSIVE $\gamma + \not\!\!E_T$ FINAL STATE

Having described non-collision background sources, in this chapter we now turn to Standard Model collision background sources. We list the Standard Model processes which can produce a reconstructed photon and nothing else in Table 4.1. We note that only $Z\gamma \to \nu\nu\gamma$ produces exactly one real photon and nothing else. In $W \to e\nu$ and $W \to \tau\nu$ production, there is no real photon, and the reconstructed photon is due to mis-reconstructing a lepton. In $W\gamma$ and $\gamma + jet$ production, the photon is real, but there are extra objects. In these cases, either a lepton or a jet must fail to be reconstructed, and in the $\gamma + jet$ case, the non-reconstruction of the jet means that the $\not\!\!E_T$ is mis-measured. We will study these backgrounds using simulated data described in Section 2.6.

We have a number of goals when looking at these events. One is the justification of the event selection requirements in Chapter 2 to remove the most pathological timing events, as well as to reduce the bias of the samples. Another is to show that after all requirements, the data are well described by the double Gaussian description. This will be crucial because the rate estimates for the number of events passing all requirements are not reliable enough to estimate each background individually. Thus, we estimate all collisions as a whole and estimate their rate using data-driven methods as discussed in Chapter 5.

4.1 Overview of the Double Gaussian Model of Collision Backgrounds

As described in Section 1.2, the characteristic timing distribution for all collision backgrounds can be modeled as the sum of the right-vertex distribution and the wrong-vertex distribution. Both distributions are Gaussian with different means and

Standard Model Collision Sources
$W \to e\nu \to \gamma_{\text{fake}} + \not\!\!E_T$
$\gamma + \text{jet} \to \gamma + \text{jet}_{\text{lost}} \to \gamma + \not\!\!E_{T\,\text{fake}}$
$W\gamma \to l\nu\gamma \to \gamma + l_{\text{lost}} + \not\!\!E_T$
$W \to \tau\nu \to \gamma_{\text{fake}} + \not\!\!E_T$
$Z\gamma \to \nu\nu\gamma \to \gamma + \not\!\!E_T$

Table 4.1: Standard Model collision backgrounds relevant in the exclusive $\gamma + \not\!\!E_T$ final state. Details of how each background is simulated can be found in Table 2.9.

widths. To understand the origin of the double Gaussian model, we must consider how the t_{corr} variable is constructed.

We see from Equation 1.2 that the t_{corr} variable takes the time of arrival from the EMTiming system and corrects it by subtracting off the presumed time-of-flight from the initial collision to the calorimeter deposit and the collision time. The location and time of the initial collision is taken from the highest ΣP_T vertex produced by the space-time vertexing algorithm.

It is worth commenting on this choice before continuing. Most reasonable models of new physics, like what we are considering here, are due to a large momentum transfer between the incoming proton and anti-proton; therefore, the most interesting collisions have high ΣP_T. In most analyses of collider data, the tracks from the leptons or jets in the events both contribute to the ΣP_T of the collision as well as allow for the unique identification of the collision that produced the final state objects. However, photons do not have tracks, so without a high P_T reconstructed track to point back to the correct vertex, while the highest ΣP_T vertex is most likely to be correct, it is still an assumption that is sometimes correct and sometimes incorrect.

While the selection of the highest ΣP_T vertex is not perfect, it is a uniquely defined selection that has the advantage that all collision events are describable as

being drawn from either the right or wrong-vertex distribution - both of which are well defined and can be cleanly modeled. Alternative suggestions, such as looping over all reconstructed vertices and choosing the lowest t_{corr}, will bias the t_{corr} distribution in a way that depends on the number of collisions in the event. In particular, the more collisions there are, the more biased the t_{corr} distribution becomes towards zero, even for signal events. Furthermore, it also makes a timing distribution for the events in our sample dependent on the number of vertices in the event, and thus very hard to model, especially for backgrounds. Our method is easy to model, well understood, and excellent for retaining signal.

If the reconstructed photon corresponds to a real, prompt photon, and the highest ΣP_T vertex corresponds to the collision which produced the photon, we call this a right-vertex event. In this case, t_f, the time recorded by the EMTiming system, is equal to the time-of-flight from the vertex plus the time the collision occurred. In a perfect detector, the t_{corr} of a photon from a right-vertex event would be identically zero. In the real EMTiming detector, the resolution has been found to be 0.6 ns [26]. This, in combination with the uncertainty in the vertex timing measurement, smears our t_{corr} to be a Gaussian centered at zero with a width of $\sim$0.65 ns.

Unfortunately, as shown in Figure 1.4a, many events contain multiple vertices, and the right vertex is not always reconstructed or selected. Therefore, we often pick the wrong vertex. When we select the wrong vertex, we subtract off a time-of-flight and collision time that have nothing to do with the collision that produced the photon. Unlike right-vertex events whose shape was dominated by EMTiming resolution effects, the wrong-vertex t_{corr} distribution is directly related to the beam profile which determines the distribution of minimum bias collisions, but is well described by a Gaussian with an RMS of 2.0 ns for reasons which will be described in more detail in Section 4.3.

4.2 Presamples and Control Samples for the Exclusive $\gamma + \not\!\!E_T$ Final State

To further study collision backgrounds, we now define the exclusive $\gamma + \not\!\!E_T$ presample. This presample is defined in Table 4.2 using the a subset of the requirements which will be used in the final analysis. We can use this set of requirements to also create control samples by selecting events from MC datasets. We will use these control samples to look for previously unknown biases and develop methods to reduce them. The requirements we develop using these control samples will be added to the presample to create the final analysis sample.

Requirement	**Selection Cut**
Trigger and good run	See Tables 2.1 and 2.2
Good isolated photon	See Table 2.6
E_T^0	> 45 GeV
$\not\!\!E_T^0$	> 45 GeV
Beam halo veto	See Table 3.4
Cosmic ray veto	See Table 3.3
High P_T track veto	See Table 2.5
Jet veto	See Table 2.3

Table 4.2: The set of requirements to create exclusive $\gamma + \not\!\!E_T$ pre-sample. Note that the trigger, beam halo, and cosmics requirements are only used for data.

While we can use the exclusive $\gamma + \not\!\!E_T$ presample requirements to select control samples in MC, there are no comparable photon control samples in real collision data which do not include our signal region. To get around this, we exploit the fact that electrons look very similar to photons in our detector with the exception that charged electrons produce a high P_T track. We create electron data control samples where we select $e + \not\!\!E_T$ events in real data passing all the high quality electron requirements

in Table 4.3, but we exclude the electron track from the vertexing algorithm to effectively simulate $\gamma + \not\!\!E_T$ events in data.

Requirement	**Selection Cut**
Trigger and good run	See Tables 2.1 and 2.2
Good electron requirements	See Table 2.7
E_T^0	> 45 (30) GeV
$\not\!\!E_T^0$	> 45 (30) GeV
Beam halo veto	See Table 3.4
Cosmic ray veto	See Table 3.3
Track veto	See Table 2.5
Jet veto	See Table 2.3
Space-time vertex	See Table 2.8

Table 4.3: The set of requirements to create the various $e + \not\!\!E_T$ control samples. Note, we use two versions of these selection requirements: one with E_T^0 and $\not\!\!E_T^0$ at 30 GeV and another with E_T^0 and $\not\!\!E_T^0$ at 45 GeV.

We can test the double Gaussian model by using the $e + \not\!\!E_T$ data control sample requiring an electron with $E_T^0 > 30$ GeV and $\not\!\!E_T^0 > 30$ GeV. Although we ignore the electron track in the vertexing algorithm, we are still able to use the electron track to determine whether the highest ΣP_T vertex we selected is right or wrong. In Figure 4.1, we show the t_{corr} distribution where the $e + \not\!\!E_T$ data is subdivided into events where the highest ΣP_T vertex is well-matched to the electron in z_0 and t_0, and those where it is not. We see that the right and wrong-vertex distributions are Gaussian out to many sigma. For the case where we always pick the highest ΣP_T vertex (without matching) is indeed well described by a double Gaussian fit. However, we note that the mean of the wrong-vertex distribution is generally not zero for reasons we discuss next. We will show comparisons between data and MC

showing that the detector simulation well describes the data in the next section, after we have described the sources of bias in wrong-vertex events.

4.3 Sources of Bias in Wrong-Vertex Events and How to Minimize Them

Previously, we mentioned that the mean t_{corr} for wrong-vertex events, $\langle t_{corr}^{WV} \rangle$, is not generally zero. We can understand this by examining the equation for the wrong-vertex time. We rewrite Eqn. 1.2 as:

$$t_{corr} = (t_f - t_i) - TOF^{meas} \tag{4.1}$$

where TOF is defined as $\frac{|\vec{x}_f - \vec{x}_i|}{c}$ which can be rewritten:

$$TOF \equiv \frac{\sqrt{R_{CES}^2 + (Z_{vtx} - Z_{CES})^2}}{c} \tag{4.2}$$

Using this, the wrong-vertex time can be written:

$$t_{corr}^{WV} = (t_f - t_i^{WV}) - TOF^{WV} \tag{4.3}$$

However, we know that the true t_f is given by $t_f = t_i^{RV} + TOF^{RV}$. Substituting in and rewriting, we find:

$$t_{corr}^{WV} = (t_i^{RV} - t_i^{WV}) + (TOF^{RV} - TOF^{WV}) \tag{4.4}$$

This version as well as the following version will be useful for our discussions about biases. We rewrite again as:

$$t_{corr}^{WV} = (t_i^{RV} - t_i^{WV}) + (TOF^0 - TOF^{WV}) + (TOF^{RV} - TOF^0) \tag{4.5}$$

where TOF^0 is the time-of-flight measured from the center of the detector (taking

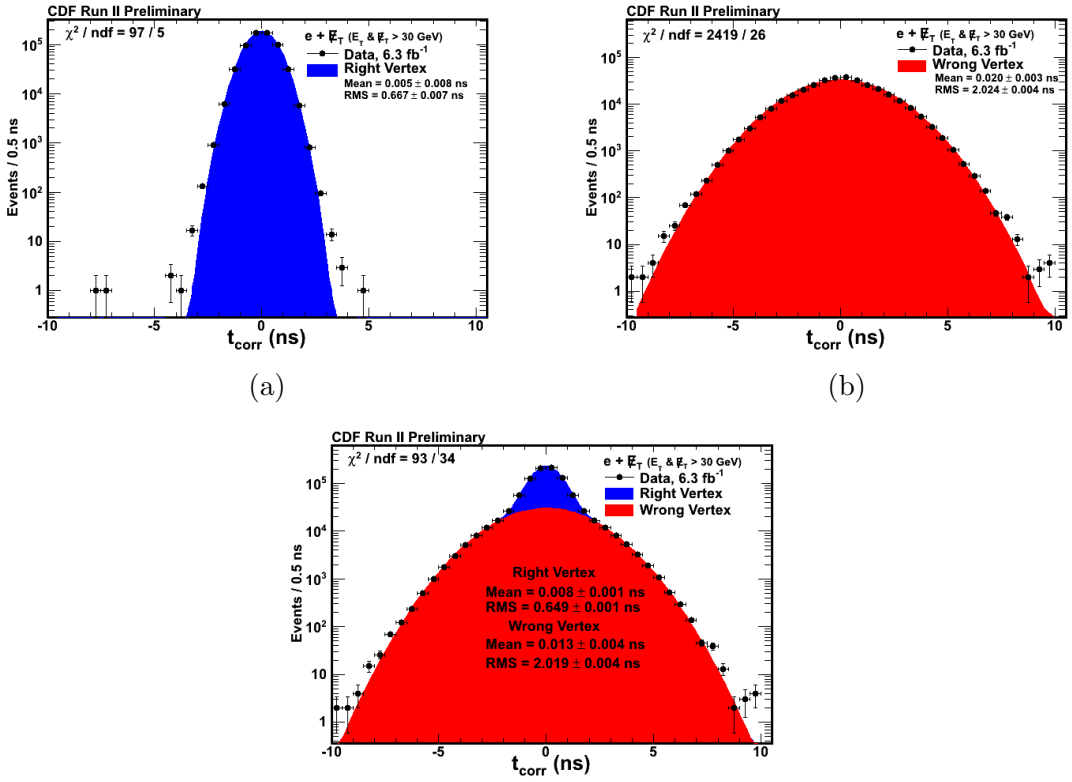

Figure 4.1: The $e + \not\!\!E_T$ data control sample, where we ignore the electron track in the vertexing, and the highest ΣP_T vertex is always selected, with $E_T > 30$ GeV. (a) The t_{corr} distribution where the electron track well matches the vertex. (b) The t_{corr} distribution where the electron track does not match the vertex. Both (a) and (b) are Gaussian to many sigma, and in (b) we observe a non-zero mean. (c) The t_{corr} distribution where the highest ΣP_T vertex is chosen regardless of the track information fitted allowing the wrong-vertex mean to float. We find that a double Gaussian fit for the right and wrong-vertex components well describes the data.

$z_{vtx} = 0$ in Equation 4.3) for reasons that will be described later. The first term is entirely dependent on the beam structure ($\langle t_i \rangle = 0$ ns and RMS$\langle t_i \rangle = 1.28$ ns) and has a mean of zero and an RMS of $1.28 \oplus 1.28$ ns [48]. The second term in Equation 4.5 is a mostly beam dependent geometric term that it is very small on average and will be discussed in more detail in Section 5.1.2. The last term is a physics dependent geometric term and can have an average value of a nanosecond or more. We refer to this term as the bias of the sample because it is the source of a possible non-zero mean wrong-vertex t_{corr}, and it is equivalent on average to $TOF^{RV} - TOF^{WV}$ up to smearing. An important point to note about this last term (and/or the second term in Equation 4.4) is that while the mean can be large, the RMS of this term is small compared to the RMS of the first term, especially when the resolution of the EMTiming system is taken into account. Thus, both Equations 4.4 and 4.5 can be well described as having a mean that is determined by the last term alone, but with an RMS that is dominated by the first term.

As the production of events with large values of t_{corr}^{WV} are the dominant source of collision background in our signal region, we describe biases which can both shift the $\langle t_{corr}^{WV} \rangle$ as well as make the wrong-vertex distribution non-Gaussian from three separate effects:

- Mis-measuring photon E_T due to selecting a wrong vertex
- Electrons being mis-identified as photons
- Events produced at large values of $|Z|$

All of these effects only lead to biased times when we select a wrong vertex (since the time is always "correct" when we select the right vertex). The large fraction of events in our data which are wrong vertex in the exclusive $\gamma + \not\!\!E_T$ final state means

that these biases are capable of strongly enhancing the background rate in the signal region. For each of these effects, we construct new requirements that either remove the most biased events, decrease their bias, or reduce their overall rate. We consider them one at a time although the underlying geometric reasons for the bias are always the same.

4.3.1 E_T Threshold Effect

The first effect that causes wrong-vertex events to be biased to large times is what we refer to as the E_T threshold effect. It is subtle so we begin with a description of the way we measure E_T in our sample as it is different than in most analyses. In most analyses there is a reliable way to determine where the collision occurred, and in those cases, E_T is a well defined quantity for any particle that hits the detector. When the wrong vertex is selected in this scenario, the E_T is always mis-measured. This occurs because of the way we measure E_T which is $E\sin\theta$ where θ is measured from the vertex position. If we get the vertex position wrong (always true for wrong-vertex events), we get $\sin\theta$, and thus, E_T wrong.

The E_T threshold effect is a bias due to wrong-vertex events with mis-measured E_T crossing the threshold to enter or exit our sample. For photons $\sin\theta$ is measured using the path length between the CES cluster associated with the calorimeter deposit and the presumed vertex position. In terms of the positions of the CES cluster and the presumed vertex position, we can write $\sin\theta^{meas}$ as

$$\sin\theta^{meas} = \frac{R_{CES}}{\sqrt{R_{CES}^2 + (Z_{vtx} - Z_{CES})^2}} \tag{4.6}$$

where R_{CES}, the radius of the CES detector, is 184.15 cm. Therefore, using Eqn. 4.2, we see

$$\sin\theta^{meas} = \frac{R_{CES}}{c \cdot TOF^{meas}} \tag{4.7}$$

which makes it clear that the time-of-flight correction and the measured $\sin\theta$, $\sin\theta^{meas}$, are inversely proportional to each other. Therefore, the measured E_T, E_T^{meas} is also inversely proportional to the time-of-flight correction. The effects of this are clear in Figure 4.2a. That is,

- If $E_T^{meas} > E_T^{true}$, $TOF^{RV} - TOF^{WV} > 0$
- If $E_T^{meas} < E_T^{true}$, $TOF^{RV} - TOF^{WV} < 0$

One might assume that the positive and negative biases in t_{corr} ought to cancel each other out; however, in the presence of a minimum E_T threshold, they add. Figure 4.2b shows exclusive $\gamma + \not\!\!E_T$ events from $W \to e\nu$ Monte Carlo that pass the requirements of Table 4.6 (note that the x-axis is the E_T^{true} of the photon). The white histogram shows events with an E_T^{meas} threshold of 25 GeV and the green histogram shows events with an E_T^{meas} threshold of 45 GeV. The events in the green histogram to the left of the line at 45 GeV are events which promoted over the threshold into the sample, specifically events which $E_T^{meas} > 45$ GeV when $E_T^{true} < 45$ GeV. These events are biased to positive times which increases the positive bias of the sample. The events to the right of the line at 45 GeV which are in the 25 GeV sample but not the 25 GeV sample are events which demoted below the threshold out of the sample. These events are biased to negative times. Since these events leave the sample, they decrease the negative bias of the sample. Rather than cancel each other out, both effects conspire to enhance the positive bias of the sample.

The E_T threshold effect is particularly strong in $W \to e\nu$ events due to the kinematic peak being 10 GeV below the 45 GeV threshold. Specifically, a large number of

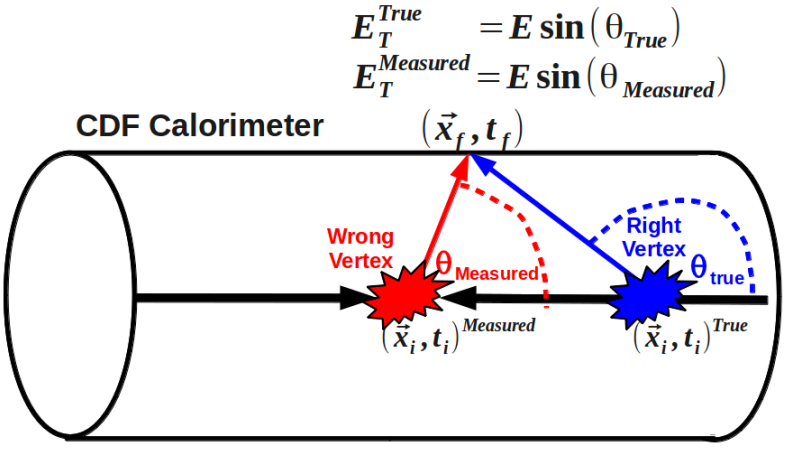

(a)

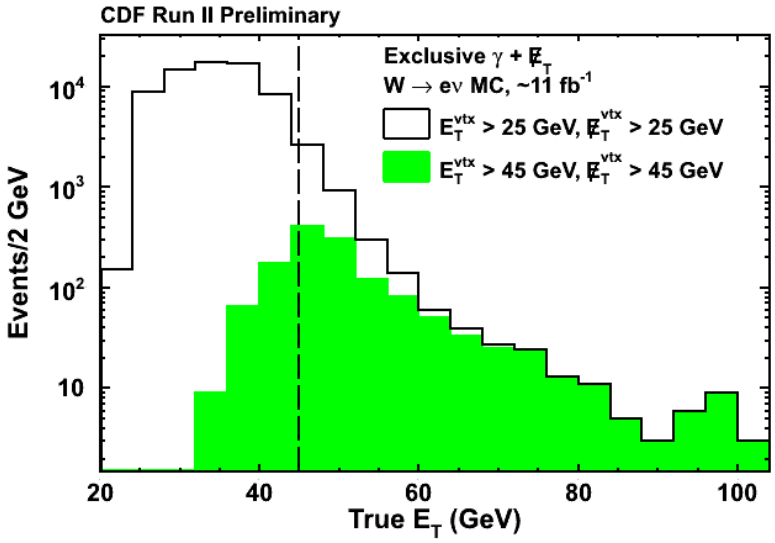

(b)

Figure 4.2: (a) Both the E_T and t_{corr} are mis-measured in a correlated way by choosing a wrong vertex. If picking a wrong vertex causes the TOF^{WV} to increase, t_{corr} and E_T^{meas} both decrease. If picking a wrong vertex causes the TOF^{WV} to decrease, t_{corr} and E_T^{meas} both increase. (b) This shows the E_T^{true} distribution for $W \to e\nu$ Monte Carlo in the exclusive $\gamma + \not\!\!E_T$ final state with E_T^{meas} greater than 25 GeV (white) and E_T^{meas} greater than 45 GeV (green). The events to the left of the line at 45 GeV are those promoting over threshold. The difference between the white and the green above 45 GeV are those demoting below threshold. Both effects conspire to cause a net positive shift in the $\langle t_{corr}^{WV} \rangle$.

events are within range of promoting or demoting over the threshold. To determine how much the E_T threshold effect can bias the wrong-vertex timing distribution, we look at $W \to e\nu$ events in the $e + \not\!\!E_T$ final state in both data and Monte Carlo (electrons that fake photons have additional biases; we focus on electrons here to separate out the threshold effect) selected using the requirements in Table 4.3, but choosing $E_T^{vtx} > 45$ GeV and $\not\!\!E_T^{vtx} > 45$ GeV to denote that they are calculated from the highest ΣP_T vertex. Figure 4.3 shows the $e + \not\!\!E_T$ final state in both data and $W \to e\nu$ Monte Carlo, and both show an almost 0.5 ns shift of the wrong-vertex timing distribution. This gives us confidence both that the MC well models the data, as well as that we understand this source of large values of $\langle t_{corr}^{WV} \rangle$.

To minimize the E_T threshold effect, we look for ways to decrease the correlation between the measured E_T and t_{corr}. Our solution is to calculate E_T relative to $Z = 0$ cm. While this has other advantages we will see later, measuring the E_T from the approximate center of the vertex distribution minimizes the average mismeasurement.

Figure 4.4 shows the t_{corr} distributions for the set of events passing the same requirements as in Figure 4.3 but with the E_T and $\not\!\!E_T$ calculated around $Z = 0$ (referred to as E_T^0 and $\not\!\!E_T^0$). Changing to E_T^0 reduces the wrong-vertex mean from $\sim$0.5 ns to $\sim$0.3 ns. Again we see excellent agreement between data and Monte Carlo. It is important to note that most events are still right vertex, and therefore, not part of the background in the signal region. We choose to continue calculating t_{corr} around the highest ΣP_T vertex because the no-vertex corrected timing distribution, t_{corr}^0, is broader than the right-vertex distribution, and the wrong-vertex event rate is low enough that using it instead would reduce the overall sensitivity to new physics by both making the right-vertex distribution have a larger RMS as well as smearing out the timing for signal events.

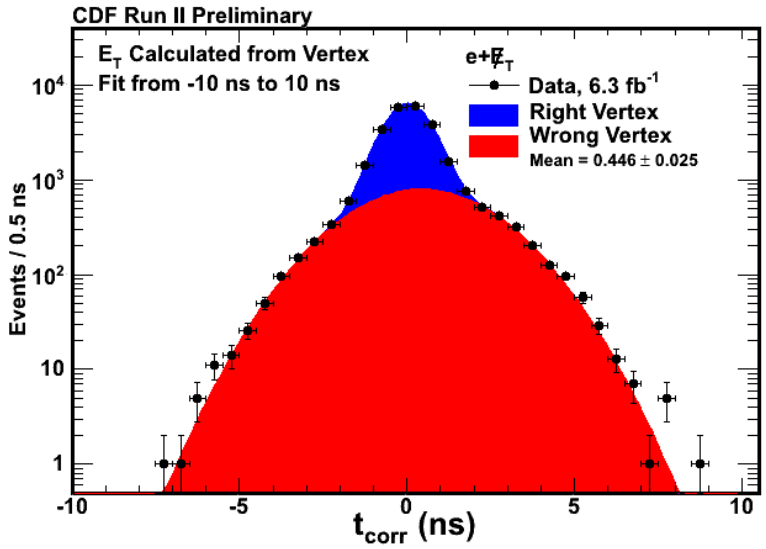

(a)

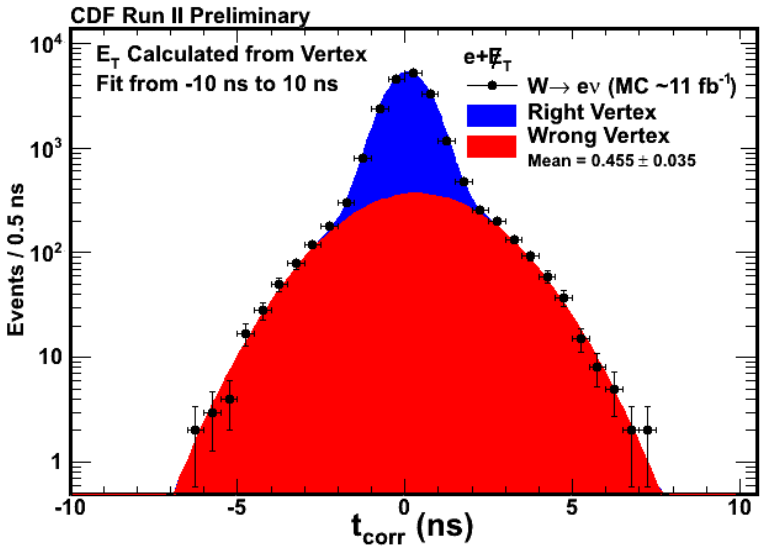

(b)

Figure 4.3: (a) The t_{corr} distribution for the sample of $e + \not\!\!E_T$ data selected with $E_T^{meas} > 45$ GeV. We observe that right-vertex events are centered at zero (as expected), but wrong-vertex events have $\langle t_{corr}^{WV} \rangle > 0$ ns. (b) The same selection in $e + \not\!\!E_T$ events from $W \to e\nu$ Monte Carlo yields results consistent with data.

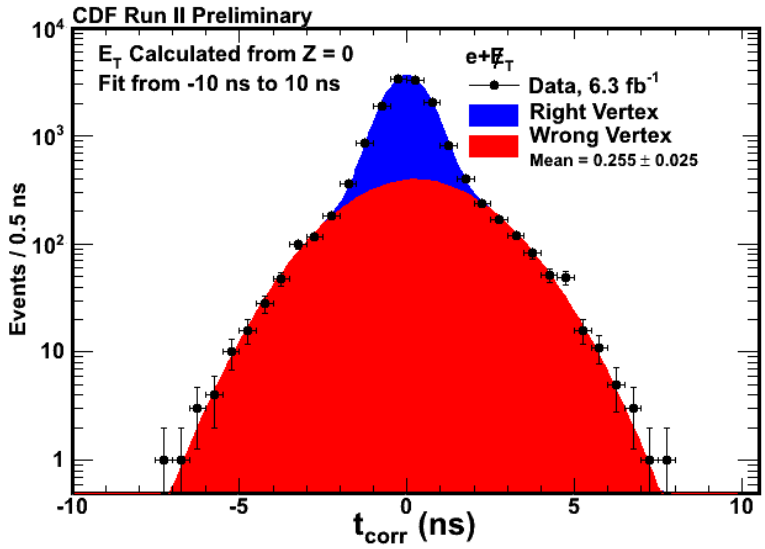

(a)

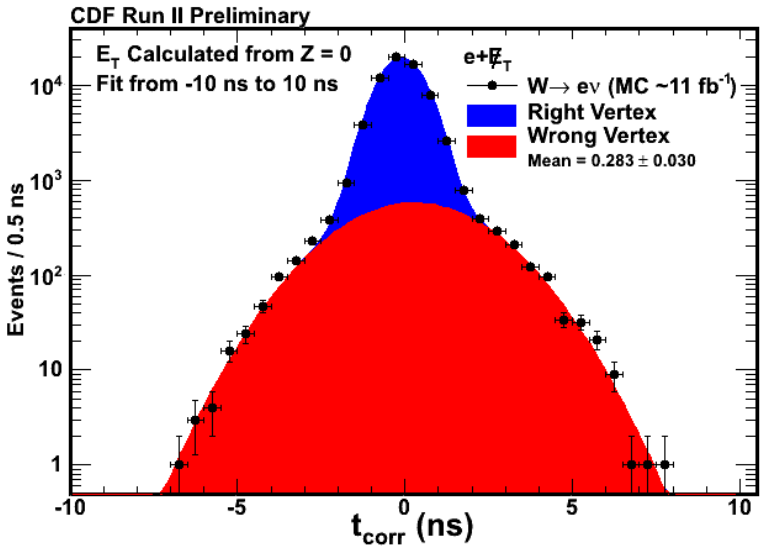

(b)

Figure 4.4: To decorrelate E_T^0 and t_{corr}, we calculate E_T around $Z_{vtx} = 0$ instead of the selected vertex. (a): This shows that in exclusive $e + \not\!\!E_T$ data, using E_T^0 reduces the mean shift. (b): This shows that in $W \to e\nu \to$ exclusive $e + \not\!\!E_T$ Monte Carlo, using E_T^0 reduces the mean shift consistent with what was seen in data.

4.3.2 Fake Photon Effect

Although the $e + \not\!\!E_T$ sample allows us to approximate the behavior of the $\gamma + \not\!\!E_T$ final state if we discard the electron track, it does not perfectly model it. There are differences between good identified electrons and electrons which were mis-identified as photons (fakes), which we will label as $e \to \gamma_{\text{fake}}$. For instance, electrons that start from large $|Z|$ positions and/or have higher η, have a lower track reconstruction efficiency, which raises the $e \to \gamma_{\text{fake}}$ rate. We can see some of these differences by using a MC sample of $W \to e\nu$ events and comparing events that are reconstructed as $\gamma + \not\!\!E_T$ (which are mostly fakes) and $e + \not\!\!E_T$ events. In particular, we compare the time of flight distributions for each. As shown in Figure 4.5a, candidates from $e \to \gamma_{\text{fake}}$ typically have longer path lengths than electrons identified as electrons. Since path length is proportional to time-of-flight, longer true path lengths imply more positively biased wrong-vertex times. Said differently, $TOF^{RV} > TOF^{WV}$ in many of the cases. We can see that this is true by comparing the bias term in Figure 4.5b which uses TOF^0 in favor of the event dependent TOF^{WV}.

To understand and mitigate this bias, we need a better understanding of what causes $e \to \gamma_{\text{fake}}$ candidates. The primary difference between a reconstructed electron and a reconstructed photon is the presence of a high P_T track pointing to the calorimeter cluster. Therefore, an electron which is mis-identified as a photon means that the track has been lost. Simulations show that there are two primary ways to lose a track: the pattern matching algorithm fails to recognize the pattern of hits in the tracking chamber as a track (tracking failure), or the electron suffered a hard bremsstrahlung interaction in the detector material. This second case is illustrated in Figure 4.6. In it, we see that the radiated photon carries away most of the electron's energy and continues moving along the direction of the parent electron. The now

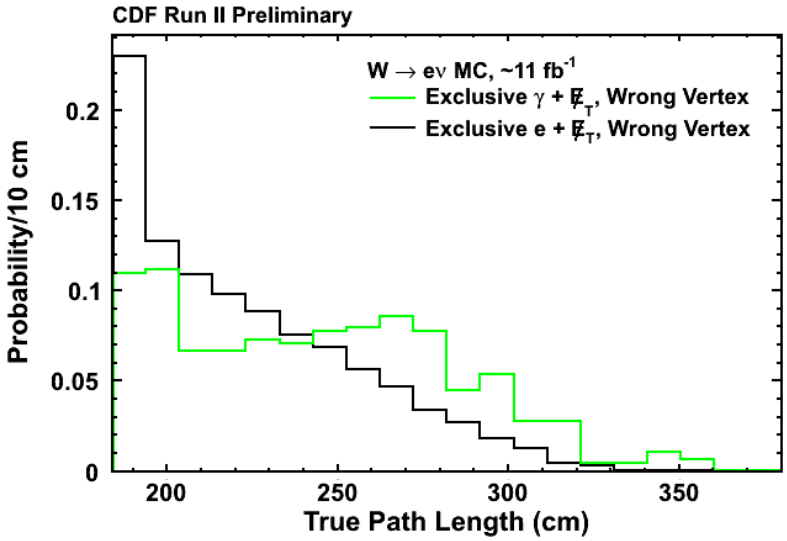

(a)

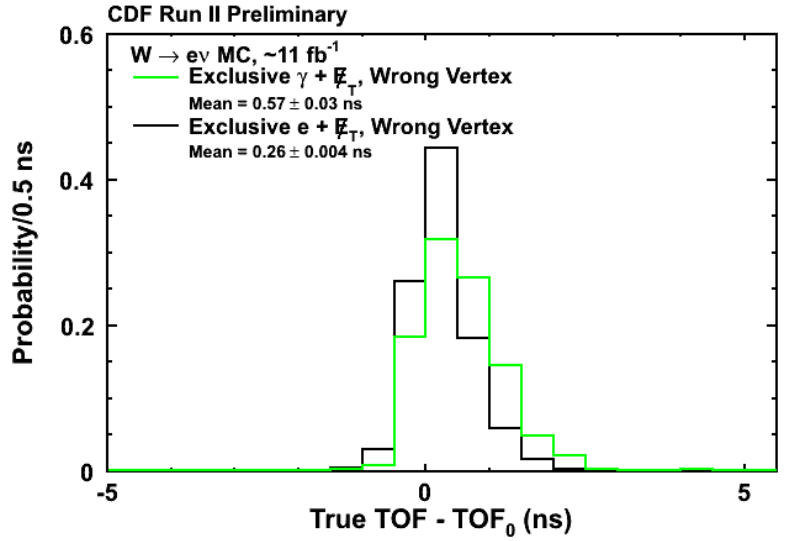

(b)

Figure 4.5: (a) Electrons mis-identified as photons tend to have longer path lengths than electrons identified as electrons. (b) The tendency of electrons mis-identified as photons to have longer path lengths causes the $TOF^{RV} - TOF^{0}$ to have a larger positive bias than correctly identified electrons.

low-energy electron spirals away due to the magnetic field and the resulting track (if identified) fails to match the calorimeter cluster.

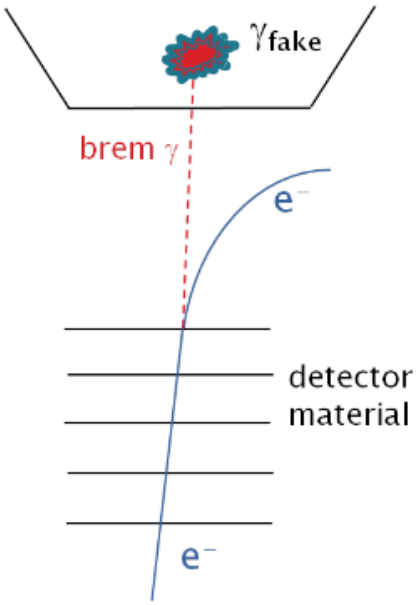

Figure 4.6: A cartoon showing the typical way an electron is mis-identified as a photon that passes all the standard photon identification requirements because of a hard interactions with the detector. The deposit in the calorimeter comes from the radiated photon, and no track is reconstructed that extrapolates toward the deposit in the calorimeter.

We can study this by using the $\gamma + \not\!\!E_T$ presample of $W \to e\nu$ MC events. Since $W \to e\nu$ MC contains both events where the electron faked a photon and those where a photon was produced in association with the W, we further restrict the sample to only those events where the reconstructed photon matches the generated electron well both geometrically and in energy. We then trace the path of the generated electron and find the locations in space of all associated radiation events, if any. Figure 4.7a

shows the radial distance from the beam line (R) and the distance along the beam line (Z) of any radiation event where a generated electron lost at least 50% of its starting energy. We find that radiation events are overwhelmingly associated with passing through SVXII detector and its associated support structures. Figure 4.7b shows the fraction of electrons having lost at least 50% of their starting energy as a function of the radial distance from the beam line. We can clearly see that the largest number of radiation events occur near 14 cm, corresponding with the location of the SVXII read out structures called port cards. In addition, we can see that the vast majority of fake photons are associated with a hard bremsstrahlung interaction. In fact, only 7% electrons associated with fake photons do not undergo a single, hard interaction. We take that as an upper limit on the fraction of fakes that are due to tracking failures.

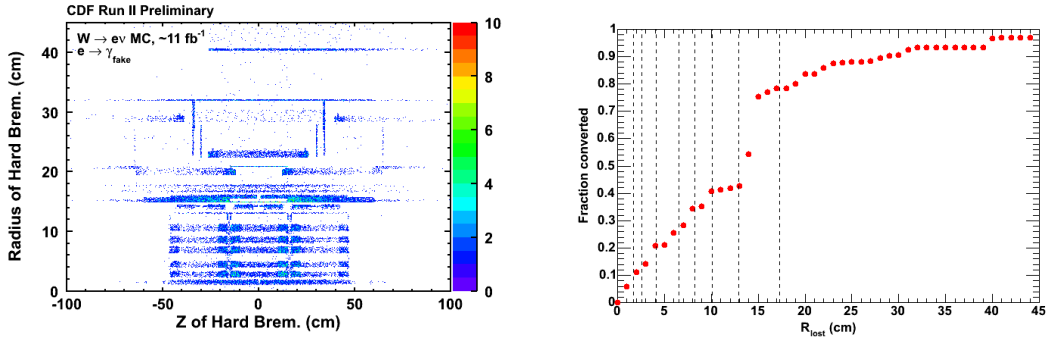

(a) (b)

Figure 4.7: Using the exclusive $\gamma + \not\!\!E_T$ presample constructed from $W \to e\nu$ MC, we isolate events where the reconstructed photon matches well geometrically and in energy to the generated electron. (a) The radial distance and the distance along the beam line where generated electrons radiated a photon with at least 50% of the electrons starting energy. (b) The fraction of electrons having undergone a hard radiation event as a function of radial distance. In both cases, we see that the hard radiation events are strongly associated with passing through the material of the SVXII detector and its support structures.

Since electrons that fake photons tend to be more biased to positive times than real photons, finding ways to identify fakes and removing them is crucial. We begin by noting two key facts: before the interaction with the detector the initial electron pointed towards the calorimeter, and it generally passes through several layers of the SVXII before the hard interaction. Based on that information, we would expect deposits in the tracking chamber to look like the straight line of the high P_T initial electron joined with the helix of the low P_T electron after the hard radiation event. The reconstructed track based on those deposits in the tracking chamber may be of low quality, but the ϕ_0 and η should be approximately that of the initial electron.

As an initial estimate of closeness, we consider the variable $\Delta R = \sqrt{(\Delta\phi)^2 + (\Delta\eta)^2}$ where $\Delta\phi = \phi_0^{trk} - \phi^{pho}$ and $\Delta\eta = \eta^{trk} - \eta^{pho}$ with η^{trk} and ϕ_0^{trk} taken from the track parameters, and η^{pho} and ϕ^{pho} calculated from the CES cluster associated with the photon. Figure 4.8 shows the $\Delta\phi$ and $\Delta\eta$ of the closest track in ΔR for events in the $\gamma + \not\!\!E_T$ presample of $W \to e\nu$ MC where the generator electron matches well with the reconstructed photon both geometrically and in energy for tracks passing the minimal requirements of COTAxialSeg(5) ≥ 2, COTStereoSeg(5) ≥ 2, and $|z_0| \leq 150$ cm. The elliptical distribution indicates that $\Delta\phi$ and $\Delta\eta$ do not have the same resolution.

We account for the different resolutions of $\Delta\phi$ and $\Delta\eta$ by creating a new measure of closeness between the calorimeter deposit and tracks defined as $\Delta R_{\text{pull}} = \sqrt{(\frac{\Delta\phi}{\sigma_\phi})^2 + (\frac{\Delta\eta}{\sigma_\eta})^2}$ where σ_ϕ and σ_η are the widths of the one dimensional $\Delta\phi$ and $\Delta\eta$ distributions and are measured to be 8.1×10^{-2} an 6.3×10^{-3} respectively. Figure 4.9a shows the ΔR_{pull} distribution for the $\gamma_{\text{fake}} + \not\!\!E_T$ presample for $W \to e\nu$ and $Z\gamma \to \nu\nu\gamma$ MC since the former is selected as a fairly pure sample of fake photons, and the later is a fairly pure sample of real, promptly-produced photons; all tracks that would make the photon fail the requirements are essentially uncorrelated in nature and thus the inefficiency is a measure of the number of tracks in the event

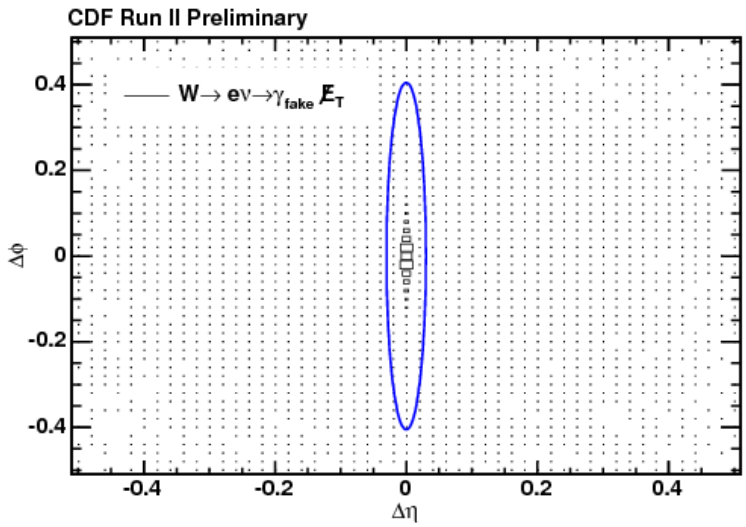

Figure 4.8: The $\Delta\phi$ vs. $\Delta\eta$ between an electron reconstructed in the events as a photon and the geometrically closest track using $W \to e\nu$ Monte Carlo in the exclusive $\gamma + \not\!\!E_T$ final state. The elliptical distribution indicates that $\Delta\phi$ and $\Delta\eta$ do not have the same resolution.

(which is expected to be small for our final state event topology). It is clear that mis-identified electrons tend to have a very small $\Delta R_{\rm pull}$ compared to real photons, where only a random track is selected. Figure 4.9b shows the fraction of fake photons rejected from the $W \to e\nu$ sample vs. the fraction of correctly identified photons retained from the $Z\gamma \to \nu\nu\gamma$ sample for a collection of $\Delta R_{\rm pull}$ requirements. For this analysis, an event is rejected if there is a track passing the requirements listed in Table 4.4 closer than $\Delta R_{\rm pull} = 5$ to the reconstructed photon. This rejects $\sim$73% of mis-identified electrons while retaining $\sim$90% of promptly produced photons.

The timing distribution of the $\gamma + \not\!\!E_T$ presample from $W \to e\nu$ MC are shown in Figure 4.10. We see that the $\Delta R_{\rm pull}$ requirement does not particularly change the $\langle t^{WV}_{corr} \rangle$ of the $W \to e\nu$ Monte Carlo sample in the $\gamma + \not\!\!E_T$ final state, but it does significantly reduce the event rate.

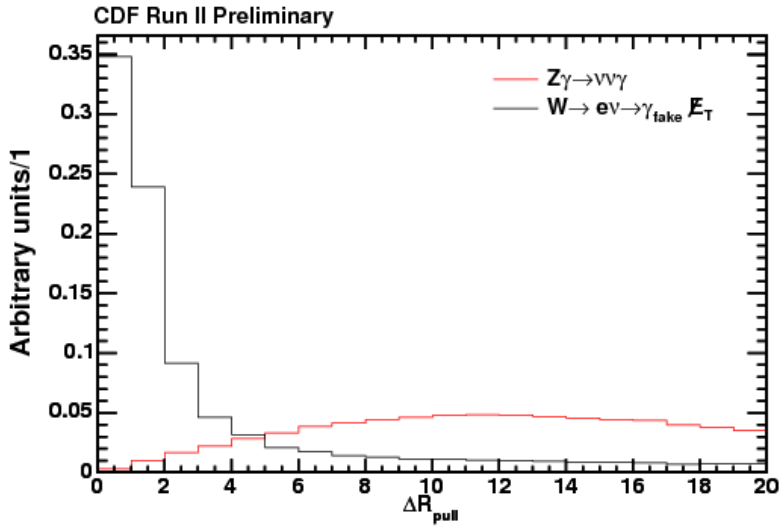

(a)

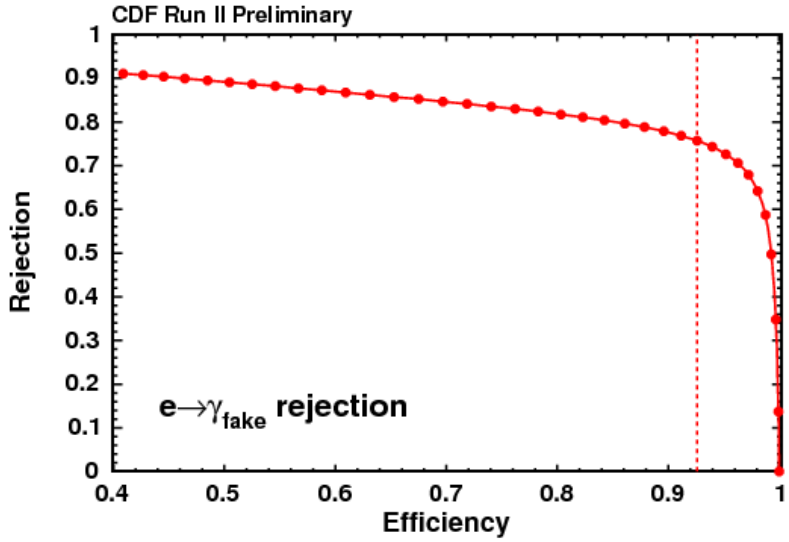

(b)

Figure 4.9: (a) The ΔR_{pull} distribution for $W \to e\nu \to \gamma_{\text{fake}} + \not\!\!E_T$ Monte Carlo (black) and $Z\gamma \to \nu\nu\gamma$ Monte Carlo (red). Mis-identified electrons from $W \to e\nu$ Monte Carlo tend to have a much smaller ΔR_{pull} than $Z\gamma \to \nu\nu\gamma$ which indicates that ΔR_{pull} has strong separation power between the poorly reconstructed track of an electron which underwent a hard interaction and random tracks near a real photon. (b) The rejection rate of mis-identified electrons from $W \to e\nu$ Monte Carlo vs. the efficiency for real photons in $Z\gamma \to \nu\nu\gamma$ Monte Carlo for varying ΔR_{pull} requirements. Requiring $\Delta R_{\text{pull}} > 5$ yields a $\sim$73% rejection rate with a $\sim$90% efficiency.

Quantity	Selection Cut
COT AxialSeg(5)	≥ 2
COT StereoSeg(5)	≥ 2
$\lvert z \rvert$	≤ 150 cm
ΔR_{Pull}	< 5.0

Table 4.4: Requirements for our $e \to \gamma_{\text{fake}}$ veto. We reject the event if there is a track that passes all the requirements in this table. We define $\Delta R_{\text{Pull}} = \sqrt{\Delta\phi^2_{\text{Pull}} + \Delta\eta^2_{\text{Pull}}}$, where $\Delta\phi_{\text{Pull}}$ and $\Delta\eta_{\text{Pull}}$ are defined as the difference between the detector location of the photon candidate and the beamline direction of the track, but divided by the resolutions of 8.1×10^{-2} and 6.3×10^{-3} in ϕ and η respectively, in order to account for detector response.

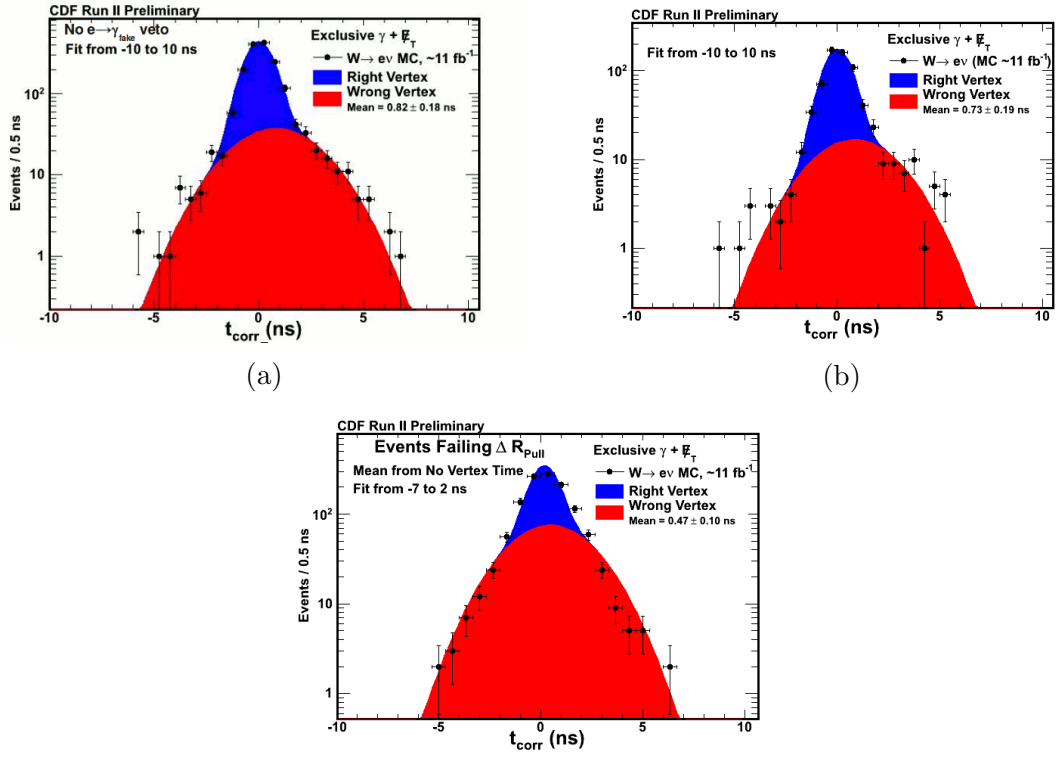

Figure 4.10: (a) The timing distribution for $W \to e\nu$ Monte Carlo events in the exclusive $\gamma + \not\!\!E_T$ final state before the ΔR_{pull} cut. Even after changing the definition of E_T, the wrong-vertex mean shift is very large. (b) The timing distribution for $W \to e\nu$ Monte Carlo events in the exclusive $\gamma + \not\!\!E_T$ final state that pass the ΔR_{pull} cut. Although this does not change the wrong-vertex mean shift much, it significantly reduces the $e \to \gamma_{\text{fake}}$ rate. (c) The $W \to e\nu$ Monte Carlo events in the exclusive $\gamma + \not\!\!E_T$ final state failing the ΔR_{pull} cut.

4.3.3 Large $|Z|$ Effect

If an event is occurs with $|Z| > 60$ cm, we will never pick the right vertex since the highest ΣP_T vertex selected is always required to have $|Z| < 60$ cm. These large $|Z|$ events typically have $TOF^{RV} > TOF^{WV}$ which means that t_{corr} can have a very large bias. This can happen for several reasons. As mentioned previously, electrons fake photons more often at large values of $|Z|$, partially due to a decreased tracking efficiency away from the center of the detector. Perhaps more importantly, for a $\gamma + jet$ event to enter into the exclusive $\gamma + \not\!\!E_T$ final state, the jet must not be reconstructed. For the jet to not be reconstructed, it must either be below threshold or fail to enter an instrumented portion of the calorimeter. The larger the $|Z|$ at which a $\gamma + jet$ event is produced, the better chance the associated jet is oriented out of the detector. This creates an enhancement at large $|Z|$ shown in Figure 4.11a, which shows the true Z position of $\gamma + jet$ MC events that pass all the $\gamma + \not\!\!E_T$ requirements. The timing distribution for these events is also biased towards large values of $\langle t^{WV}_{corr} \rangle$ as seen in Figure 4.11b.

To minimize this effect, we reject any events with evidence of having been produced at a large value of $|Z|$. Specifically, we reject any event that has a standard ZVertex [36] with $|Z| > 60$ cm which contain at least three tracks as listed in Table 4.5. We use standard vertices because we are using them purely for rejection, not to measure timing. The standard vertexing algorithm is designed to be as efficient as possible for as large a $|Z|$ as possible whereas the space-time algorithm [39] is designed to report on vertices with a well-measured time as well as separate out cases where two collisions occur in the same event close in Z but with different times which would cause a problem measuring t_i in Equation 1.2. The t_{corr} distribution for the $\gamma + \not\!\!E_T$ presample from $\gamma + jet$ MC after these requirements is shown in Fig-

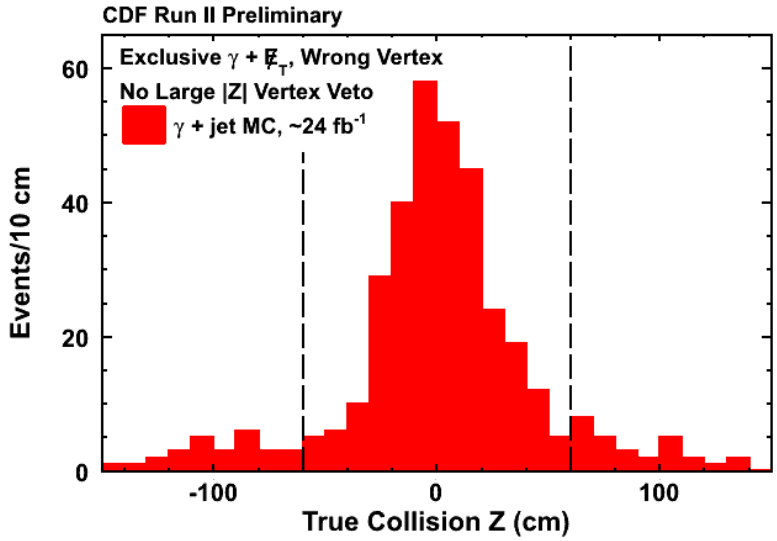

(a)

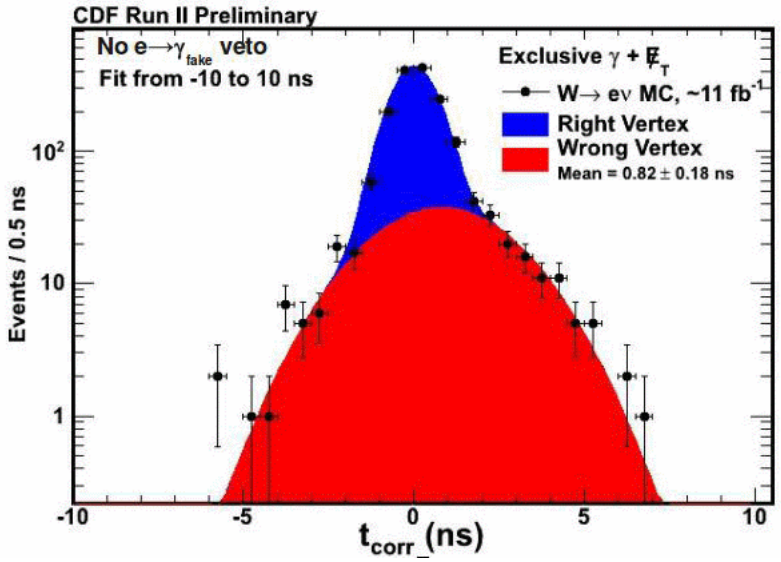

(b)

Figure 4.11: (a) The Z position of the collision as measured in a sample of $\gamma + jet$ Monte Carlo events passing all exclusive $\gamma + \not\!\!E_T$ final state requirements, including the E_T^0 and $\Delta R_{\rm pull}$ cuts. Note that many events occur at large $|Z|$. (b) The timing distribution for these events. Note the significant shift in the wrong-vertex mean.

ure 4.12. As expected, the large $|Z|$ veto rejects events with very large times, and the remaining wrong-vertex mean is decreased.

Quantity	**Selection Cut**
N_{track}	≥ 3
$\lvert z\rvert$	> 60cm

Table 4.5: Requirements for our large standard vertex $|z|$ veto. We reject events with a standard vertex that passes all the requirements in this table.

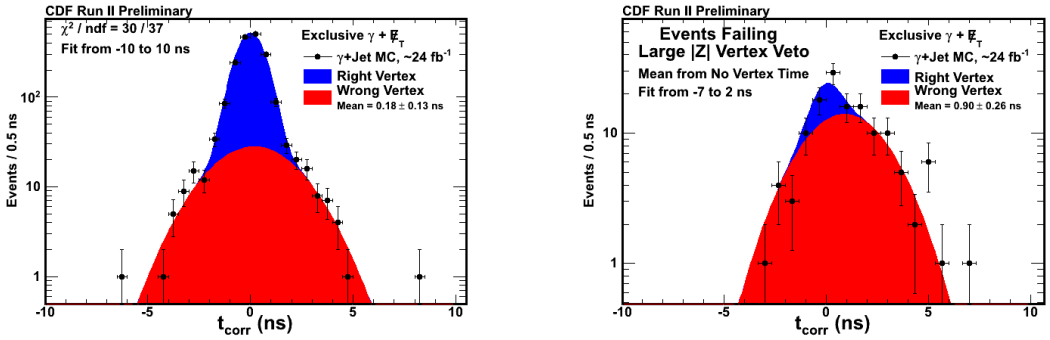

(a) (b)

Figure 4.12: (a) The t_{corr} distribution for $\gamma + jet$ Monte Carlo events in the exclusive $\gamma + \not\!\!E_T$ final state passing the large $|Z|$ veto (no standard vertex with at least 3 tracks having $|Z|$ greater than 60 cm). (b) The timing distribution for those events failing the large $|Z|$ veto. The wrong-vertex mean is very positive.

4.4 Timing Distributions for Standard Model Backgrounds

Having finished our study of the biases present in Standard Model collision backgrounds and added three important requirements to reduce them, we can now fully define the event selection requirements for the exclusive $\gamma + \not\!\!E_T$ final state. The full set of requirements are listed in Table 4.6.

Requirement	**Selection Cut**
Trigger and good run (applied to data only)	See Tables 2.1 and 2.2
Good isolated photon	See Table 2.6
E_T^0	> 45 GeV
$\not\!\!E_T^0$	> 45 GeV
Beam halo veto	See Table 3.4
Cosmic ray veto	See Table 3.3
High P_T track veto	See Table 2.5
Jet veto	See Table 2.3
Large standard vertex $\|z\|$ veto	See Table 4.5
Electron rejection veto	See Table 4.4
Vertex selection	See Table 2.8

Table 4.6: The set of requirements to create the various exclusive $\gamma + \not\!\!E_T$ datasets. Note that the "no vertex" samples are created using the same requirements, but requiring that there be no good space-time vertex in the event.

Using these requirements, we construct control samples from all of our background Monte Carlo samples described in Table 2.9. Figure 4.13 shows the t_{corr} distribution for all six MC samples as well as the two exclusive $e + \not\!\!E_T$ data control samples where the electron track is removed from the vertexing. To demonstrate that all samples are well described by the double Gaussian model, we fit each timing distribution to the sum of two Gaussians over the range (-10,10) ns. We fix the right-vertex

mean to zero, the right-vertex RMS to 0.65 ns, and the wrong-vertex RMS to 2.0 ns. However, we allow the wrong-vertex mean and the normalization of each Gaussian to float. In each case, the double Gaussian model well describes the data.

We can further test the double Gaussian model by relaxing the requirement that the wrong-vertex RMS = 2.0 ns. Figure 4.14 shows fitted wrong-vertex RMS for each sample as a function of the fitted wrong-vertex mean. We see that wrong-vertex RMS is consistent with our assumption of 2.0 ± 0.1 ns for all samples, and there is no dependence of the wrong-vertex RMS on the wrong-vertex mean. The detailed fit results are listed in Table 4.7. Now that we have confidence in the double Gaussian model, we now look for methods to estimate the background contribution in the signal region.

Sample	$\langle t_{corr}^{WV} \rangle$ **(ns)**	$RMS\langle t_{corr}^{WV} \rangle$ **(ns)**
W→ eν	0.69 ± 0.22	2.18 ± 0.17
γ+Jet	0.18 ± 0.13	2.04 ± 0.16
Zγ	0.08 ± 0.05	1.97 ± 0.05
W→ $\mu\nu$	0.30 ± 0.23	2.06 ± 0.18
W→ $\tau\nu$	0.48 ± 0.22	1.97 ± 0.22
Wγ	0.14 ± 0.09	2.14 ± 0.08
$e + \not\!\!E_T$ data	0.16 ± 0.07	2.05 ± 0.07
$e + \not\!\!E_T$ data (E_T^0,$\not\!\!E_T^0 > 30$ GeV)	0.04 ± 0.05	1.98 ± 0.05

Table 4.7: Summary of the measured $\langle t_{corr}^{WV} \rangle$ and $RMS\langle t_{corr}^{WV} \rangle$ for our SM MC and $e + \not\!\!E_T$ data control samples selected using the cuts in Tables 4.6 and 4.3. In these results we have allowed the mean and RMS of the WV Gaussian to float in the fit.

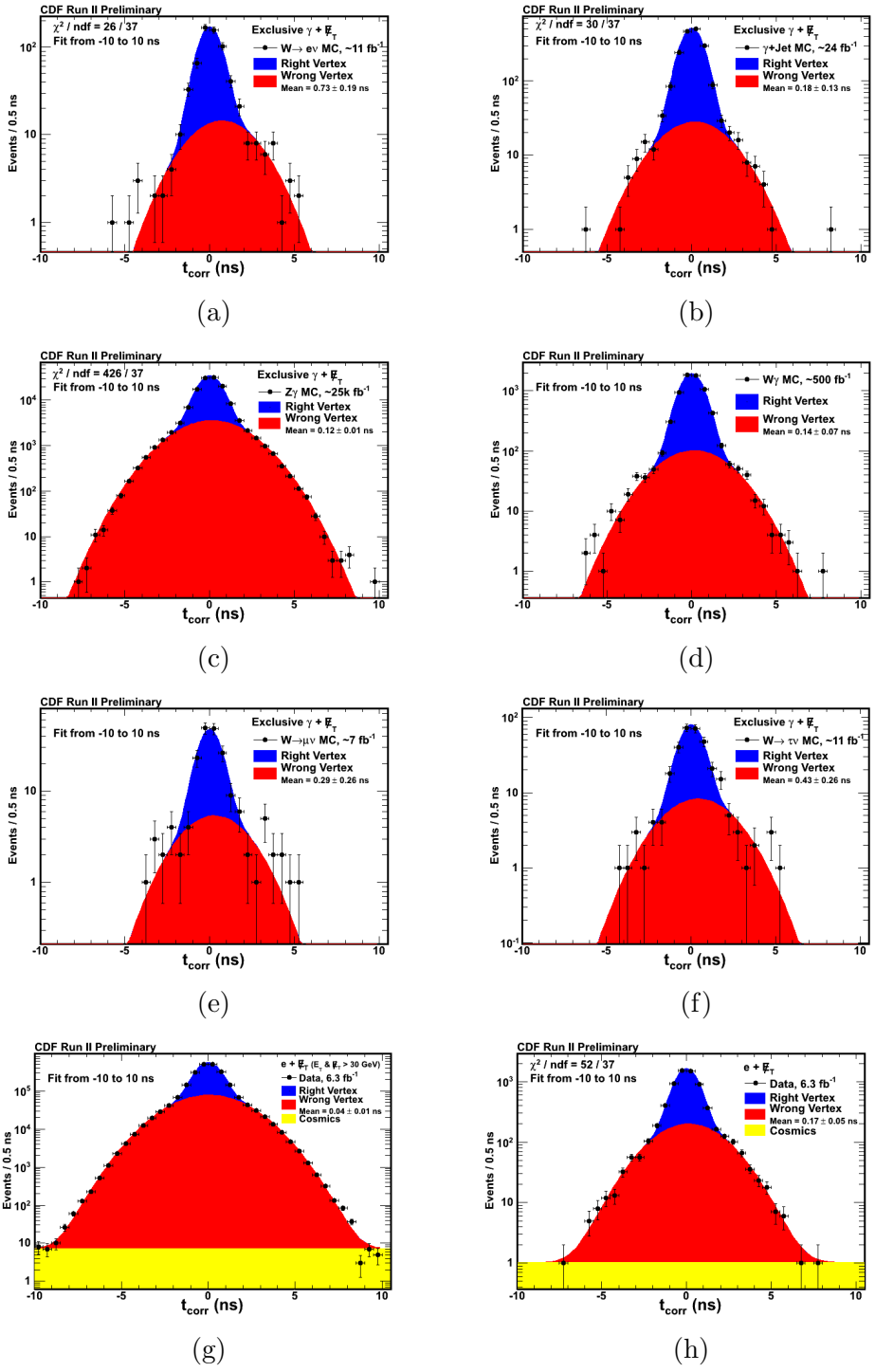

Figure 4.13: The results of a double Gaussian fit for a number of Monte Carlo datasets as well as two electron datasets from data using the full selection requirements: (a) $W \to e\nu$, (b) γ + jet, (c) $Z\gamma$, (d) $W\gamma$, (e) $W \to \mu\nu$, (f) $W \to \tau\nu$, (g) $e + \not\!\!E_T$ (30 GeV), (h) $e + \not\!\!E_T$ (45 GeV)

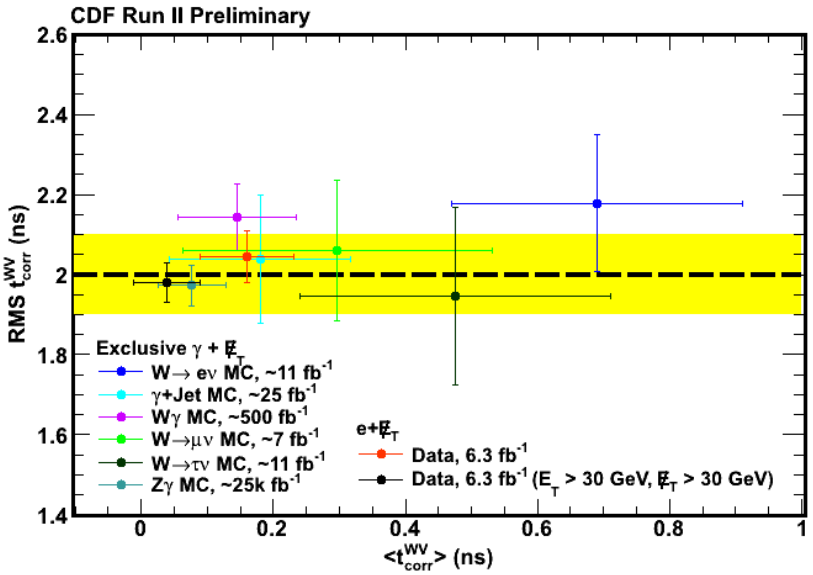

Figure 4.14: The fitted $RMS\langle t_{corr}^{WV}\rangle$ vs. the fitted $\langle t_{corr}^{WV}\rangle$. We find that the $RMS\langle t_{corr}^{WV}\rangle$ is consistent with the assumption of 2.0 ns for all samples, regardless of the fitted $\langle t_{corr}^{WV}\rangle$.

5. BACKGROUND ESTIMATION

In the previous chapters we studied the various classes of backgrounds to the exclusive $\gamma + \not\!\!E_T$ final state. We have seen that beam halo and satellite bunch events can be effectively neglected, but that cosmic ray events can, which will be the dominant background in the signal region, be described by a flat distribution in time. We have seen that after implementing new rejection techniques, all collision background sources can be described by a double Gaussian with only the normalizations and the wrong-vertex mean completely unknown. We now seek to use this knowledge to develop techniques for estimating the background contributions to the signal region.

We note that while we have used Standard Model Monte Carlo samples to study collision backgrounds, we cannot be confident enough in their predictions of the overall rates to use them for estimation purposes. For instance, we cannot be sure that the rate of selecting the wrong vertex is properly modeled. Because of this, we will use data-driven methods. In Section 5.1 we will describe how the double Gaussian model can be used to predict the number of events in the signal region. We first show how to do this if there were only one collision background source, then we show how to generalize the method to the case of multiple background sources. Finally, in Section 5.2 we show how to implement these techniques using a combined likelihood function.

5.1 Data-Driven Background Estimation for Collision Sources

5.1.1 Single Collision Source of Wrong-Vertex Events

We begin by considering a single collision wrong-vertex background source with no cosmic ray contamination. Since our goal is to estimate the background contribution in the signal region, we begin by defining the wrong-vertex sideband region as shown

in Figure 5.1a. Since the right-vertex distribution is narrow, right-vertex events are negligible in both the wrong-vertex sideband and the signal region; therefore, both regions can be described by the same wrong-vertex Gaussian t_{corr} distribution. The wrong-vertex distribution is characterized by three parameters: the number of wrong-vertex events (N_{WV}), the wrong-vertex mean ($\langle t_{corr}^{WV} \rangle$), and the wrong-vertex RMS ($RMS\langle t_{corr}^{WV} \rangle$). Since $RMS\langle t_{corr}^{WV} \rangle$ is known to be 2.0 $\pm$ 0.1 ns, the ratio of the number of events in the signal region ($N_{(2,7)}$) to the number of events in the wrong-vertex sideband ($N_{(-7,-2)}$) only depends on the wrong-vertex mean. The integral of a Gaussian can be described in terms of the error function defined as:

$$Erf(x) = \frac{2}{\pi} \int_0^x e^{-t^2} dt \tag{5.1}$$

allowing us to write $N_{(2,7)}$ and $N_{(-7,-2)}$ as:

$$N_{(2,7)} = N_{WV} \cdot \epsilon(\langle t_{corr}^{WV} \rangle, 2, 7) \tag{5.2}$$

$$N_{(-7,-2)} = N_{WV} \cdot \epsilon(\langle t_{corr}^{WV} \rangle, -7, -2) \tag{5.3}$$

where $\epsilon(\langle t_{corr}^{WV} \rangle, a, b)$ is the integral of a Gaussian normalized to unit area over the interval (a,b), defined as:

$$\epsilon(\langle t_{corr}^{WV} \rangle, a, b) = \left(Erf(\frac{b - \langle t_{corr}^{WV} \rangle}{RMS\langle t_{corr}^{WV} \rangle \sqrt{2}}) - Erf(\frac{a - \langle t_{corr}^{WV} \rangle}{RMS\langle t_{corr}^{WV} \rangle \sqrt{2}}) \right) \tag{5.4}$$

Using these, we define the ratio:

$$R(\langle t_{corr}^{WV} \rangle) = \frac{N_{(2,7)}}{N_{(-7,-2)}} = \frac{\epsilon(\langle t_{corr}^{WV} \rangle, 2, 7)}{\epsilon(\langle t_{corr}^{WV} \rangle, -7, -2)} \tag{5.5}$$

where N_{WV} cancels out. The value of $R(\langle t_{corr}^{WV} \rangle)$ is shown in Figure 5.1b as a function of $\langle t_{corr}^{WV} \rangle$. The yellow band represents the variation due to the uncertainty on $RMS\langle t_{corr}^{WV} \rangle$. As long as Standard Model collision backgrounds are consistent with the double Gaussian model (as shown in the previous chapter), we expect ths relationship to hold.

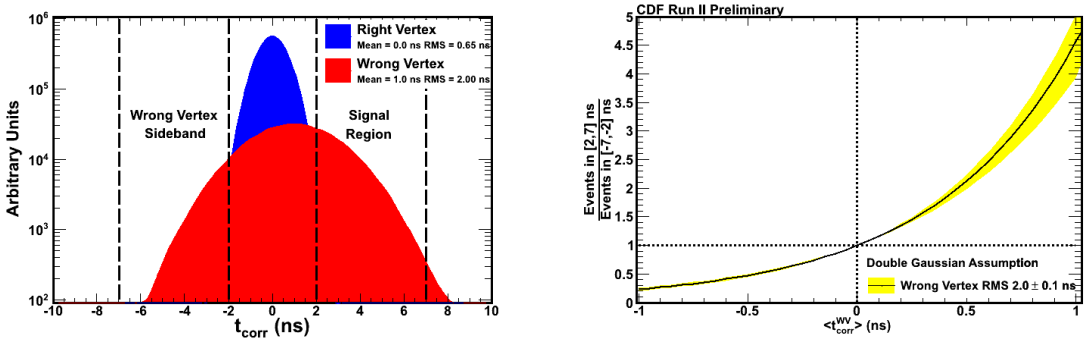

(a) (b)

Figure 5.1: (a) The Wrong-vertex sideband (-7,-2) ns and signal region (2,7) ns. (b) The ratio of $N_{(2,7)}$ to $N_{(-7,-2)}$ vs. the assumed wrong-vertex mean.

We test this expectation using all the Monte Carlo $\gamma + \not\!\!E_T$ control samples and the $e + \not\!\!E_T$ data control samples using two different E_T^0 and $\not\!\!E_T^0$ thresholds, 30 GeV and 45 GeV. For each control sample, we count the observed number of events in the signal region and the wrong-vertex sideband to calculate the ratio. We plot this against $\langle t_{corr}^{WV} \rangle$ derived from a double Gaussian fit in the region (-10,10) ns with $\langle t_{corr}^{RV} \rangle$, $RMS\langle t_{corr}^{RV} \rangle$, and $RMS\langle t_{corr}^{WV} \rangle$ fixed at their nominal value. The results are shown Figure 5.2 over the prediction curve. More detailed results are listed in Table 5.1. We see that all samples agree with the prediction derived from the double Gaussian model. This suggests that if we were able to develop an independent estimate of

$\langle t_{corr}^{WV} \rangle$, estimating $N_{(2,7)}$ from $N_{(-7,-2)}$ would be straight-forward by using:

$$N_{(2,7)}^{Exp} = N_{(-7,-2)}^{Obs} * R(\langle t_{corr}^{WV} \rangle) \tag{5.6}$$

where we note that if $\langle t_{corr}^{WV} \rangle = 0$, this reduces to the original assumption that $N_{(2,7)} = N_{(-7,-2)}$ as used in the original delayed photon analysis and the preliminary result from 2008 [21].

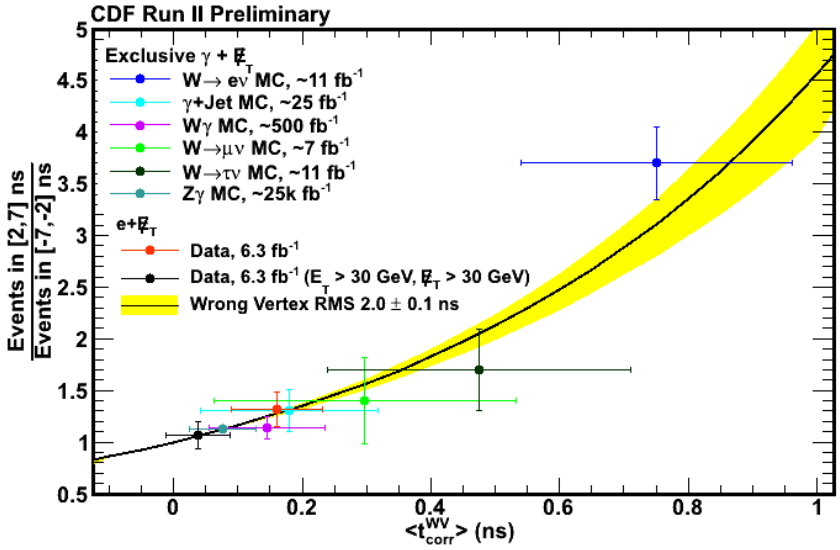

Figure 5.2: We find that all samples agree well with the prediction from the Double Gaussian approximation for a wide range of $\langle t_{corr}^{WV} \rangle$.

5.1.2 Estimating the Wrong-Vertex Mean

We now turn to the crux of this analysis, the task of estimating $\langle t_{corr}^{WV} \rangle$ for our sample. In Figure 5.2 we were able estimate $\langle t_{corr}^{WV} \rangle$ from a simple fit over the range (-10,10) ns, so a naive suggestion would be simply to fit over the range (-7,2) ns

Sample	$\langle t_{corr}^{WV} \rangle$ **(ns)**	**Predicted Ratio**	**Observed Ratio**
$W \to e\nu$ MC	0.73 ± 0.19	2.92 ± 1.01	3.70 ± 0.36
γ+Jet MC	0.18 ± 0.13	1.30 ± 0.26	1.30 ± 0.20
$W\gamma$ MC	0.14 ± 0.07	1.22 ± 0.14	1.14 ± 0.11
$Z\gamma$ MC	0.12 ± 0.01	1.20 ± 0.01	1.12 ± 0.02
$W \to \mu\nu$ MC	0.29 ± 0.26	1.50 ± 0.70	1.40 ± 0.41
$W \to \tau\nu$ MC	0.43 ± 0.26	1.26 ± 0.16	1.70 ± 0.40
$e + \not\!\!E_T$ Data	0.16 ± 0.05	1.26 ± 0.16	1.32 ± 0.17
$e + \not\!\!E_T$ Data (E_T^0,$\not\!\!E_T^0 > 30$ GeV)	0.04 ± 0.05	1.03 ± 0.07	1.06 ± 0.13

Table 5.1: Summary of the measured $\langle t_{corr}^{WV} \rangle$, as well as the predicted and observed ratio of the number of events in the signal region (2 ns $< t_{corr} <$ 7 ns) to the number of events in the control region (-7 ns $< t_{corr} <$ -2 ns), for the SM MC and two $e + \not\!\!E_T$ data control samples selected using the cuts in Tables 4.6 and 4.3.

to avoid including the signal region. Unfortunately, this does not work for several reasons. The region (-7,-2) ns only contains the tail of the wrong-vertex distribution. Because of that, a fit would not be able to distinguish between a large $\langle t_{corr}^{WV} \rangle$ and a decreased N_{WV} introducing an unacceptable level of correlation. Extending the fit further to include the (-2,2) ns region does not help since the right-vertex distribution dominates in this region and obscures the turn over of the wrong-vertex distribution. The addition of cosmic ray events further complicates the matter by adding additional uncertainty. Therefore, the only reliable option is to seek an independent experimental handle.

Because we changed our definition of E_T to be calculated around zero, it is possible to define the no-vertex sample, a sample of $\gamma + \not\!\!E_T$ events that is orthogonal to the exclusive $\gamma + \not\!\!E_T$ sample and consists of all events passing all requirements for the exclusive $\gamma + \not\!\!E_T$ final state except that they have no reconstructed space-time vertex. We expect this sample to be topologically similar to our sample of events with a good vertex, especially since we know that many of our good-vertex events

do not select the right vertex because the right vertex is not actually reconstructed. Since there is no reconstructed vertex, we consider the timing variable t^0_{corr} as defined in Equation 2.1.

Using the same arguments as before, we note that t^0_{corr} is Gaussian distributed like the wrong-vertex distribution, but due to one less factor of vertex timing variation, its RMS is 1.28 $\oplus$ 0.6 ns where the 1.28 ns comes from beam parameters and the 0.6 ns comes from the EMTiming resolution. Overall, this produces an RMS of $\sim$1.6 ns. Figure 5.3 shows the no-vertex distribution for all the MC $\gamma + \not\!\!E_T$ control samples and the $e + \not\!\!E_T$ data control samples. Each sample is fit from (-5,3) ns with an RMS fixed to 1.6 ns. The $e + \not\!\!E_T$ data control samples also include a cosmic ray component estimated from the region (20,80) ns.

We further test the no-vertex distribution by refitting each sample to a Gaussian while allowing both the mean and RMS to float. We see in Figure 5.4 that all samples have a fitted RMS consistent with 1.6 ns up to a systematic uncertainty of 5%. In addition, although the fitted mean varies for all sample, the RMS is constant. More detailed results are listed in Table 5.2.

Now that we understand the shape of the no-vertex distribution, we note the important relationship between t^{WV}_{corr} and t^0_{corr}. Using the true time of arrival from $t_f = t_i^{RV} + TOF^{RV}$, we can rewrite Equation 2.1 as:

$$t^0_{corr} = t_i^{RV} + TOF^{RV} - TOF^0 \tag{5.7}$$

Substituting this into Equation 4.5, we find:

$$t^{WV}_{corr} = t^0_{corr} - t_i^{WV} + (TOF^0 - TOF^{WV}) \tag{5.8}$$

Wrong vertices are produced independent of the physics of the right vertex, so

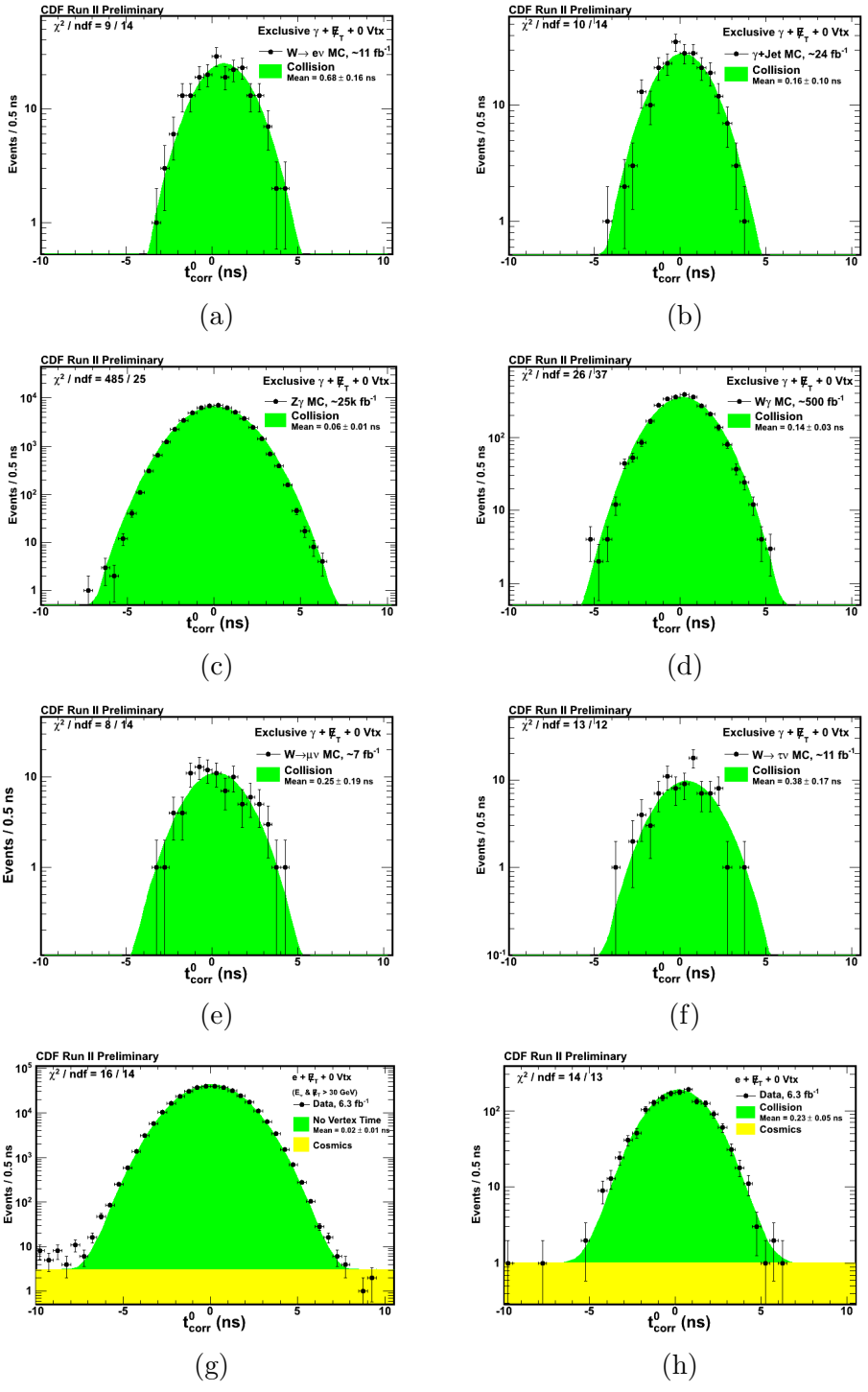

Figure 5.3: The t^0_{corr} distribution for events with no reconstructed vertex: (a) $W \to e\nu$, (b) $\gamma + jet$, (c) $Z\gamma \to \nu\nu\gamma$, (d) $W\gamma$, (e) $W \to \mu\nu$, (f) $W \to \tau\nu$, (g) $e + \not\!\!E_T$ data (30 GeV), (h) $e + \not\!\!E_T$ data (45 GeV)

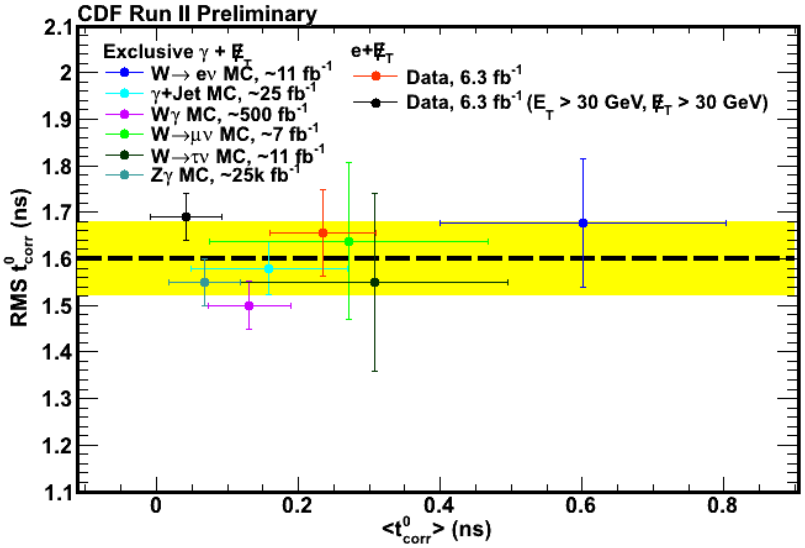

Figure 5.4: The fitted RMS vs. the fitted mean for the six background Monte Carlo samples and two data control samples. We find that the RMS is consistent with the assumption of 1.6 ± 0.08 ns for all samples, regardless of the fitted no-vertex mean.

Sample	$\langle t^0_{corr} \rangle$ **(ns)**	$RMS\langle t^0_{corr} \rangle$ **(ns)**
W→ eν MC	0.61 ± 0.20	1.68 ± 0.14
γ+Jet MC	0.16 ± 0.11	1.58 ± 0.06
Zγ MC	0.07 ± 0.05	1.55 ± 0.05
W→ $\mu\nu$ MC	0.27 ± 0.20	1.64 ± 0.17
W→ $\tau\nu$ MC	0.31 ± 0.19	1.56 ± 0.19
Wγ MC	0.13 ± 0.06	1.50 ± 0.05
$e + \not\!\!E_T$ data	0.23 ± 0.08	1.66 ± 0.09
$e + \not\!\!E_T$ data (E^0_T,$\not\!\!E^0_T$ > 30 GeV)	0.04 ± 0.05	1.69 ± 0.05

Table 5.2: Summary of the measured $\langle t^0_{corr} \rangle$ and $RMS\langle t^0_{corr} \rangle$ for our SM MC and $e + \not\!\!E_T$ data control samples selected using the cuts in Tables 4.6 and 4.3. In these results we have allowed the mean and RMS of the Gaussians to float in the fit.

$\langle t_i^{WV} \rangle = 0$ ns and simply adds a Gaussian smearing of 1.28 ns as previously mentioned.

An important term in Equation 5.8 is $TOF^0 - TOF^{WV}$. This term is largely physics independent, and as shown in Figure 5.5a, it is very small on average since distance from the beam line to the calorimeter (184.15 cm) is very large compared to the scale of deviations from the center of the detector for wrong vertices ($\langle Z_{WV} \rangle = 0$ cm and RMS$\langle Z_{WV} \rangle = 28$ cm). We test this using a toy Monte Carlo drawing vertices from the beam profile and assuming a uniform η distribution. The resulting $TOF^0 - TOF^{WV}$ distribution is shown in Figure 5.5b. The average difference is $\sim$40 ps and the RMS is less than 50 ps.

Therefore, to a good degree of approximation, we expect $\langle t_{corr}^{WV} \rangle \approx \langle t_{corr}^{0} \rangle$ if we had a sample of wrong-vertex events and calculated both t_{corr}^{WV} and t_{corr}^{0} from them. Because the no-vertex sample is selected in an identical away to the wrong-vertex sample, and in both cases, the right-vertex was not selected, we expect the relation to still hold.

We check this by comparing the means from Figure 4.14 and Figure 5.4. As shown in Figure 5.6a $\langle t_{corr}^{WV} \rangle \approx \langle t_{corr}^{0} \rangle$ for each sample. Note that the term $\langle t_{corr}^{WV} \rangle$ can only be directly measured in MC or the $e + \not\!\!E_T$ control samples, but $\langle t_{corr}^{0} \rangle$ from the no-vertex sample can be measured in data since it is an orthogonal dataset. More details are shows in Table 5.3. Although the match is quite good, based on simulations of the mean of $TOF^0 - TOF^{WV}$ and the limits of our calibrations, we take $\langle t_{corr}^{WV} \rangle = \langle t_{corr}^{0} \rangle \pm 80$ ps to conservatively overestimate the systematic uncertainties.

Perhaps the ultimate test is to compare the observed ratio for good-vertex events with the measured $\langle t_{corr}^{0} \rangle$ from the no-vertex sample for all eight control samples. We see in Figure 5.6b that $\langle t_{corr}^{0} \rangle$ is as predictive of the ratio of $N_{(2,7)}$ to $N_{(-7,-2)}$ as $\langle t_{corr}^{WV} \rangle$. A detailed comparison of observed and expected ratios using $\langle t_{corr}^{0} \rangle$ is shown

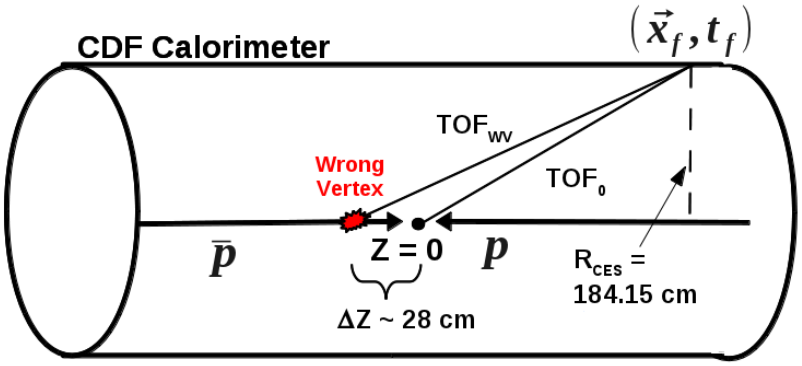

(a)

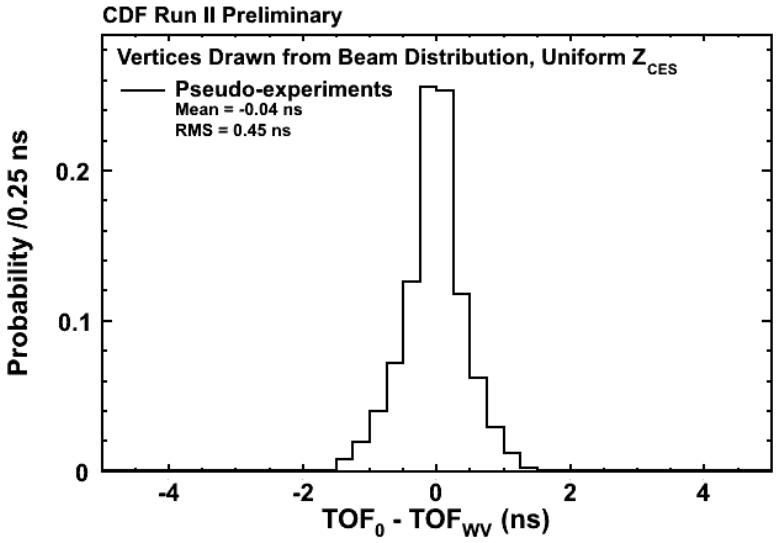

(b)

Figure 5.5: An illustration of why $\langle t^{WV}_{corr} \rangle \approx \langle t^{0}_{corr} \rangle$. (a) The large distance between the beam line and the calorimeter and the small variation in wrong-vertex Z positions means that measuring t_{corr} from zero is often a good approximation for t_{corr} from a wrong-vertex. (b) The distribution of $TOF^0 - TOF^{WV}$ from a toy Monte Carlo events where we draw vertices from the beam profile, and we assume a uniform η distribution. On average, they are very close together (around 40 ps).

in Table 5.1. Again, we note that on the figure, the black line is not a fit, but is rather the prediction for the double Gaussian assumption.

Sample	$\langle t^{WV}_{corr} \rangle$ **(ns)**	$\langle t^{0}_{corr} \rangle$ **(ns)**
$W \to e\nu$ MC	0.73 ± 0.19	0.68 ± 0.16
γ+Jet MC	0.18 ± 0.13	0.16 ± 0.10
$W\gamma$ MC	0.14 ± 0.07	0.14 ± 0.03
$Z\gamma$ MC	0.12 ± 0.01	0.06 ± 0.01
$W \to \mu\nu$ MC	0.29 ± 0.26	0.25 ± 0.19
$W \to \tau\nu$ MC	0.43 ± 0.26	0.38 ± 0.17
$e + \not\!\!E_T$ Data	0.16 ± 0.05	0.23 ± 0.05
$e + \not\!\!E_T$ data (E^0_T,$\not\!\!E^0_T > 30$ GeV)	0.04 ± 0.05	0.02 ± 0.01

Table 5.3: Summary of the measured means, $\langle t^{WV}_{corr} \rangle$ and $\langle t^{0}_{corr} \rangle$, of the wrong vertex and no vertex timing distributions for our SM MC and $e + \not\!\!E_T$ data control samples selected using the cuts in Tables 4.6 and 4.3. In these results we have allowed the mean and RMS of the Gaussians to float in the fit.

5.1.3 Multiple Collision Sources of Wrong-Vertex Events

So far in this section, we have only considered the predictions from single Standard Model collision backgrounds; however, we know that there are multiple Standard Model collision backgrounds which span a range of characteristic wrong-vertex means. For a data-driven approach to work, it must be possible to treat the sum of Standard Model sources as a single background. We expect this to work because the RMS of the wrong-vertex distribution is large compared to the value of $\langle t^{WV}_{corr} \rangle$ for most backgrounds. To show that this works, we use several methods.

We begin by showing the results of a toy Monte Carlo which combines two wrong-vertex distributions which have characteristic means similar to our most biased and

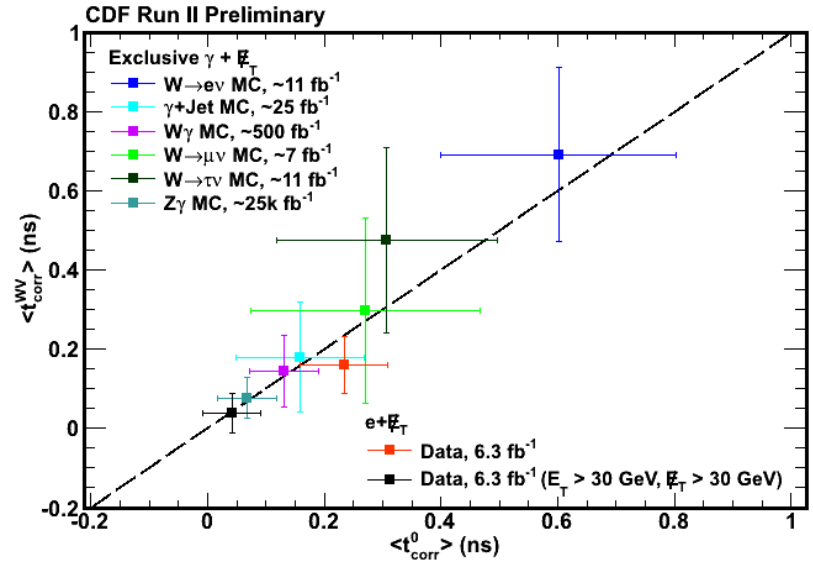

(a)

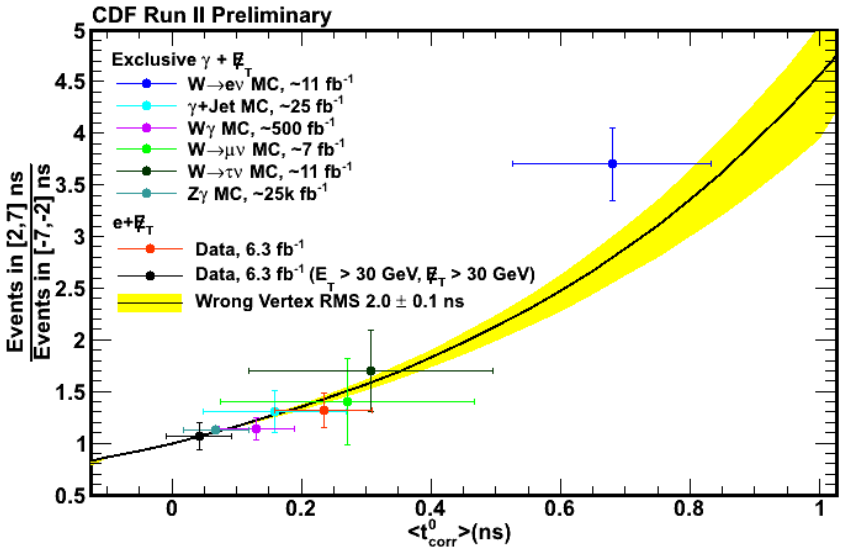

(b)

Figure 5.6: Two plots which show that we can use the no-vertex sample to estimate the mean of the wrong-vertex distribution in data. (a) For our set of Monte Carlo control samples as well as two $e + \not\!\!E_T$ control samples from data, we isolate wrong-vertex (using generator quantities or the electron track) and no-vertex events, and we plot the fitted wrong-vertex mean vs. the fitted no-vertex mean. We find that the wrong-vertex and no-vertex means agree for all samples within a small systematic uncertainty which we take to be 80 ps. (b) The no-vertex mean is as predictive of the ratio of events in the signal region to the number of events in the wrong-vertex sideband region as the wrong-vertex mean.

Sample	$\langle t^0_{corr} \rangle$ **ns**	**Predicted Ratio**	**Observed Ratio**
$W \to e\nu$ MC	0.68 ± 0.16	2.74 ± 0.76	3.70 ± 0.36
γ+Jet MC	0.16 ± 0.10	1.27 ± 0.20	1.30 ± 0.20
$W\gamma$ MC	0.14 ± 0.03	1.23 ± 0.05	1.14 ± 0.11
$Z\gamma$ MC	0.06 ± 0.01	1.09 ± 0.02	1.12 ± 0.02
$W \to \mu\nu$ MC	0.25 ± 0.19	1.46 ± 0.48	1.40 ± 0.41
$W \to \tau\nu$ MC	0.38 ± 0.17	1.77 ± 0.51	1.70 ± 0.40
$e + \not\!\!E_T$ Data	0.23 ± 0.05	1.39 ± 0.31	1.32 ± 0.17
$e + \not\!\!E_T$ Data (E^0_T,$\not\!\!E^0_T$ > 30 GeV)	0.02 ± 0.01	1.03 ± 0.07	1.06 ± 0.13

Table 5.4: Summary of the measured $\langle t^0_{\rm corr} \rangle$, as well as the predicted and observed ratio of the number of events in the signal region (2 ns < $t_{\rm corr}$ < 7 ns) to the number of events in the control region (-7 ns < $t_{\rm corr}$ < -2 ns), for the SM MC and two $e + \not\!\!E_T$ data control samples selected using the cuts in Tables 4.6 and 4.3.

least biased backgrounds. That is, $W \to e\nu$, which has characteristic wrong-vertex mean near 0.8 ns, and $Z\gamma \to \nu\nu\gamma$, which has a characteristic wrong-vertex mean near 0.1 ns. We combine these Gaussians, each with an RMS of 2.0 ns, in varying fractions from 0% $Z\gamma \to \nu\nu\gamma$ to 100% $Z\gamma \to \nu\nu\gamma$. We fit the resulting distribution to a Gaussian in the region (-7,2) ns. We do a similar combination for no-vertex-like Gaussians with an RMS of 1.6 ns, which we fit to a Gaussian in the region (-3.5,3.5) ns. The results in Figure 5.7 shows that the fitted mean is well described by the weighted mean of the two sub-components. As expected, the fitted RMS increases as we approach a 50% combination; however, it is covered by the 5% systematic uncertainty we took from Figure 5.2. Thus, no special consideration is required in the treatment of the no vertex and wrong-vertex means. We further validate this approach in Chapter 6.

5.2 The Combined Likelihood Method

To summarize, we now understand that the backgrounds can be well described as the sum of three components with different shapes. Right-vertex events are due to

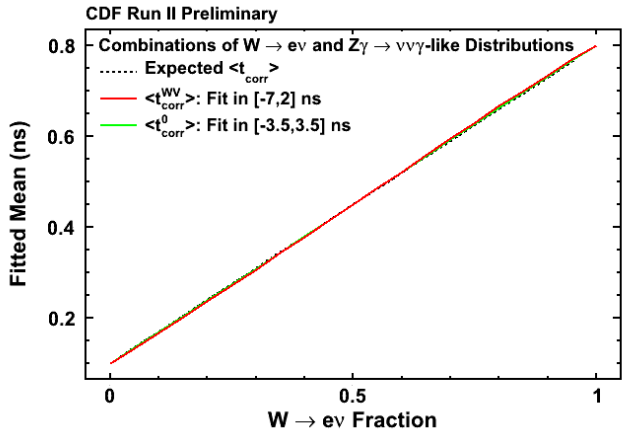

(a)

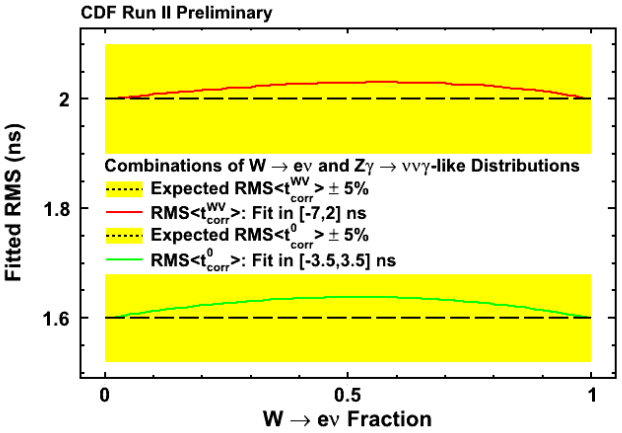

(b)

Figure 5.7: We examine the amount the wrong-vertex shape changes due to combinations of multiple collision sources by generating pseudo-experiments combining Gaussians with means 0.1 ns and 0.8 ns in varying fractions (similar to $Z\gamma \to \nu\nu\gamma$ and $W \to e\nu$ backgrounds). (a) This shows the fitted mean for combinations mimicking no-vertex or wrong-vertex distributions. In either case, the fitted mean is the weighted average of the means of the two distributions being combined with no deviation from expectations. (b) This shows the fitted RMS for combinations mimicking no-vertex or wrong-vertex distributions. In both cases, the fitted RMS tends to increase as we move towards a 50% mixture. This increase is small and well covered by the expected 5% systematic uncertainty on the RMS. With this systematic uncertainty, we can treat combined standard Model backgrounds using the double Gaussian approximation.

collisions for which the correct vertex was chosen. The shape of such events is known to be Gaussian with a mean of 0.0 ± 0.05 ns and an RMS of 0.65 ± 0.05 ns. Wrong-vertex events are due to collisions for which the incorrect vertex was chosen since the correct vertex was not the highest ΣP_T vertex. These events are also Gaussian distributed with a mean that can be significantly greater than zero; however, the RMS remains consistent with 2.0 ± 0.1 ns after all selection requirements. Cosmic ray events are flat in time since the are completely uncorrelated with the timing of the beam collisions. Therefore, the background expectation for the exclusive $\gamma + \not\!\!E_T$ signal region is described by the sum of two Gaussians and a uniform distribution, fully specified by seven parameters. These parameters can be determined in a data-driven manner.

We now discuss the fit we use to incorporate all the relationships we have described. To do this, we use the maximum likelihood method with a binned, extended likelihood function [49] and consider data from both the good-vertex and no-vertex samples. In practical terms, we minimize the negative log-likelihood defined as

$$-\ln \mathcal{L} \equiv \sum_i -n_i \ln \nu_i + \nu_i \tag{5.9}$$

where n_i is the observed number of events in a bin and ν_i is the expected number of events in a bin. We define a negative log-likelihood for the good-vertex sample and no-vertex sample separately. In the good-vertex sample, the expected number of events in a bin according to the double Gaussian model with cosmic ray events is

$$\nu_i^{GV} = \int_{t_i}^{t_{i+1}} \Big(N_{RV} * \mathcal{G}\left(t, \langle t_{corr}^{RV} \rangle, RMS\langle t_{corr}^{RV} \rangle\right) + N_{WV} * \mathcal{G}\left(t, \langle t_{corr}^{WV} \rangle, RMS\langle t_{corr}^{WV} \rangle\right) + n_{cosm}^{GV} \Big) dt \tag{5.10}$$

where $\mathcal{G}$ is the Gaussian function, N_{RV} is the number of right-vertex events, $\langle t^{RV}_{corr}\rangle$ is the right-vertex mean, $RMS\langle t^{RV}_{corr}\rangle$ is the right-vertex RMS, N_{WV} is the number of wrong-vertex events, $\langle t^{WV}_{corr}\rangle$ is the wrong-vertex mean, $RMS\langle t^{WV}_{corr}\rangle$ is the wrong-vertex RMS, and n^{GV}_{cosm} is the number of cosmic ray events per nanosecond in the good-vertex sample. Similarly, in the no-vertex sample, the expected number of events in a bin is

$$\nu_j^{NV} = \int_{t_j}^{t_{j+1}} \Big(N_{NV} * \mathcal{G}\left(t, \langle t^0_{corr}\rangle, RMS\langle t^0_{corr}\rangle\right) + n^{NV}_{cosm} \Big) dt \tag{5.11}$$

where N_{NV} is the number of no-vertex events, $\langle t^0_{corr}\rangle$ is the no-vertex mean, $RMS\langle t^0_{corr}\rangle$ is the no-vertex RMS, and n^{NV}_{cosm} is the number of cosmic ray events per nanosecond in the no-vertex sample.

We use information from the no-vertex sample to help estimate the wrong-vertex mean by creating a combining the likelihoods for the good-vertex sample and the no-vertex sample and adding a Gaussian constraint requiring that the wrong-vertex mean equal the no-vertex mean up to a 0.08 ns uncertainty. We also incorporate systematic uncertainties on the right-vertex mean, right-vertex RMS, and wrong-vertex RMS as Gaussian constraint terms [50]. The resulting combined likelihood can be written

$$-\ln\mathcal{L} \equiv -\ln\mathcal{L}_{GV} - \ln\mathcal{L}_{NV} - \sum_{constraints} \frac{(\alpha_k - \hat{\alpha_k})^2}{2\sigma_k^2} \tag{5.12}$$

We evaluate $-\ln\mathcal{L}_{GV}$ over all bins in the region $t_{corr} \in (-7, 2) \cup (20, 80)$ ns. The region (20,80) ns is necessary to properly estimate the cosmic ray rate. We evaluate $-\ln\mathcal{L}_{NV}$ over all bins in the region $t^0_{corr} \in (-3.5, 3.5) \cup (20, 80)$ ns. We choose the region (-3.5,3.5) ns to estimate the collision background portion of the

no-vertex sample because beam halo is more of a potential concern in the no-vertex sample than the good-vertex sample. We also note that the cosmic ray rate must be estimated independently for both samples.

The constrained parameters, α_k, the nominal values of the parameters, $\hat{\alpha}_k$, and the systematic uncertainties on those parameters, σ_k are shown in Table 5.5. The uncertainty on $\langle t^{RV}_{corr} \rangle$ and $RMS\langle t^{RV}_{corr} \rangle$ are due to the tolerance of our calibrations methods. The uncertainty on $RMS\langle t^{WV}_{corr} \rangle$ is derived from the variations due to combining wrong-vertex distributions with very different means as described previously. We tune the uncertainty for measuring $\langle t^{WV}_{corr} \rangle$ from $\langle t^{0}_{corr} \rangle$ using pseudo-experiments drawn from full Monte Carlo described in Section 6.2.2.

Parameter	**Nominal Value**	**Systematic Uncertainty**
$\langle t^{\mathrm{RV}}_{\mathrm{corr}} \rangle$	0 ns	0.05 ns
$\mathrm{RMS}\langle t^{\mathrm{RV}}_{\mathrm{corr}} \rangle$	0.65 ns	0.05 ns
$\langle t^{\mathrm{WV}}_{\mathrm{corr}} \rangle$	$\langle t^{0}_{\mathrm{corr}} \rangle$	0.08 ns
$\mathrm{RMS}\langle t^{\mathrm{WV}}_{\mathrm{corr}} \rangle$	2.0 ns	0.1 ns

Table 5.5: Systematic uncertainty constraint terms for the likelihood fit.

Now that our background estimation procedure is fully defined, we can now apply it to our final dataset. In the next chapter, we will perform our fit in the sideband regions, but before we compare to the results in the signal region, we will first use the fit result to construct validations of our method.

6. SEARCHING FOR NEW PHYSICS IN THE EXCLUSIVE $\gamma + \not\!\!E_T$ FINAL STATE

Having described our background estimation method, in this chapter we are ready to perform the search for new physics in the exclusive $\gamma + \not\!\!E_T$ final state. In Section 6.1 we show the fit to the sideband regions in our final dataset representing 6.3 fb^{-1} of integrated luminosity. In Section 6.2 we then use the sideband fit results to validate the background estimation method and make predictions about our final uncertainties for the backgrounds in the signal region. We validate the results using two methods: pseudo-experiments drawn from idealized distributions and pseudo-experiments derived from our Monte Carlo control samples. Having validated the fit method, in Section 6.3 we compare the background prediction in the signal region to the data observed in the signal region. Finally, in Section 6.4 we compare the new result to the previous 2008 result.

6.1 Event Selection and Background Predictions

Using the requirments listed in Table 4.6, we select the events of the final exclusive $\gamma + \not\!\!E_T$ dataset from CDF data corresponding to an integrated luminosity of 6.3 fb^{-1}. Table 6.1 shows the number of events surviving each subsequent requirement we apply. We find that 5,421 events pass all requirements necessary to be part of the good-vertex sample while 4,942 events pass the requirements to be part of the no-vertex sample.

As described in the previous chapter, we construct a likelihood function which allows us to perform a simultaneous fit to both the good and no-vertex samples. This uses information from the no-vertex sample to assist in determining $\langle t^{WV}_{corr} \rangle$. Figure 6.1a shows the result of the fit for the no-vertex sample while Figure 6.1b

Requirement	**Number of Events**
Central photon with $E_T^0 > 45$ GeV, $\not\!\!E_T^0 > 45$ GeV and passing trigger requirements	38,291
Beam halo veto	36,764
Cosmics veto	24,462
Track veto	16,831
Jet veto	12,708
Large $\|Z\|$ vertex veto	11,702
$e \to \gamma_{\text{Fake}}$ veto	10,363
Good vertex events/no vertex events	5,421/4,942

Table 6.1: Event reduction table for the exclusive $\gamma + \not\!\!E_T$ search. The last selection requirement breaks the events into two samples: 1) Events that do have a reconstructed vertex and 2) events that do not have a good space-time vertex ("no vertex sample"). The sample of events that do have a reconstructed vertex are the events on which we perform our search for $\gamma_{\text{delayed}} + \not\!\!E_T$ while the "no vertex sample" is used to estimate $\langle t^0_{\text{corr}} \rangle$.

shows the result of the fit to the sideband regions for the good-vertex sample. We use the measured values of N_{RV}, N_{WV}, N_{NV}, n^{GV}_{cosm}, n^{NV}_{cosm}, and $\langle t^{WV}_{corr} \rangle$ shown in Table 6.2 to create pseudo-experiments validating the method.

Parameter	**Value**
N_{RV}	875 ± 66
N_{WV}	676 ± 84
N_{NV}	257 ± 27
$N^{\text{GV}}_{\text{cosm}}$	31.9 ± 0.7 events/ns
$N^{\text{NV}}_{\text{cosm}}$	38.1 ± 0.8 events/ns
$\langle t^{\text{WV}}_{\text{corr}} \rangle$	0.23 ns $\pm$ 0.1 ns

Table 6.2: Parameter values determined from the sideband regions in the $\gamma + \not\!\!E_T$ data and used as inputs to the pseudo-experiments to determine the search sensitivty.

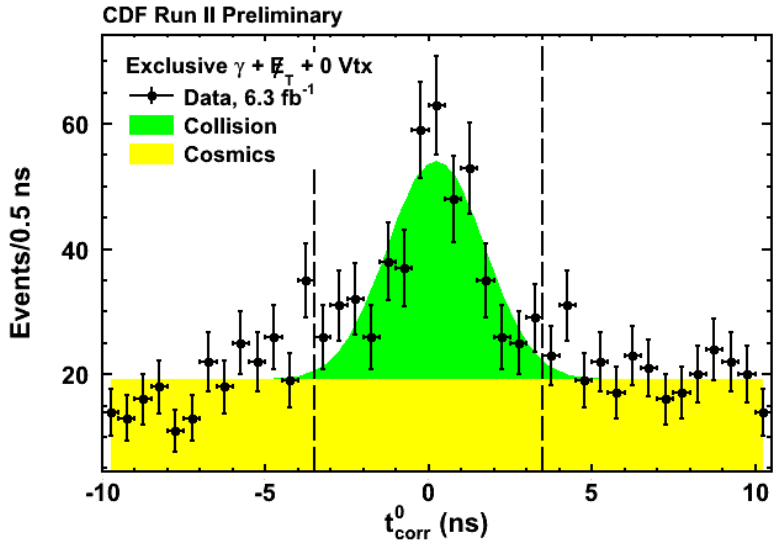

(a)

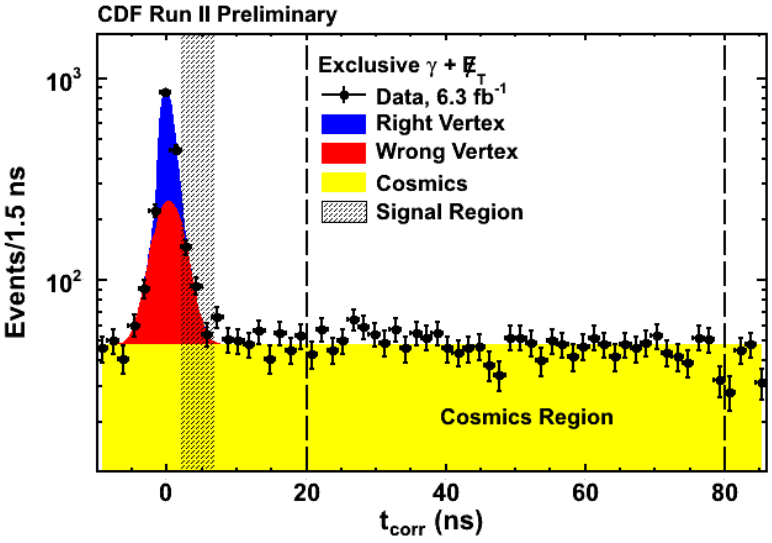

(b)

Figure 6.1: (a) The no-vertex distribution is fit in (-3.5,3.5) ns and (20,80) ns. This assists the estimation of the wrong-vertex mean. (b) The good vertex data with the signal region blinded. In addition to the collision sideband region, we fit in (20,80) ns to estimate the cosmic ray rate.

6.2 Fit Validation

Before we compare the number of events observed in the signal region to the number predicted, we must first validate the fit procedure. In general terms, we would like to know that for an ensemble of pseudo-experiments with qualities similar to data the background estimation method predicts the correct number of events, on average. That is, if calculate $N^{Obs}_{(2,7)} - N^{Exp}_{(2,7)}$ for each pseudo-experiment, the average of the entire ensemble should be close to zero. If this is true, the fit can be called unbiased. We also want to know how it responds for a variety of wrong-vertex means, from 0 ns to 1 ns, even though our sideband estimate indicates a mean of 0.23 ns.

In addition to checking for bias, the fit validation must also check to see if the error estimate assigned to the predicted number of events is correct. To determine this, as well as whether the fit is biased, we use a value called pull defined as:

$$Pull = \frac{N^{Obs}_{(2,7)} - N^{Exp}_{(2,7)}}{\sqrt{\sigma^2_{Exp} + \sigma^2_{Obs}}} \tag{6.1}$$

where σ_{Exp} is the uncertainty on $N^{Exp}_{(2,7)}$ as estimated by the fit, and σ_{Obs} is the statistical uncertainty on $N^{Obs}_{(2,7)}$. The errors in quadrature represent the total uncertainty. Since $N^{Obs}_{(2,7)}$ is a Poisson varying quantity, we use the Gaussian approximation of the uncertainty, $\sqrt{N}$. For an unbiased fit with well estimated uncertainties, the distribution of pulls over an ensemble of pseudo-experiments should be Gaussian with a mean of zero and an RMS of one.

We now measure the pull for two different validations. The first method uses ideal distributions (perfect Gaussians and uniform distributions) varied according to the presumed systematic uncertainties. This method is essentially a sanity check to be sure that if the fitter is supplied with exactly what it expects, it responds

properly. The second method uses the MC exclusive $\gamma + \not\!\!E_T$ control samples as the source distributions for generating pseudo-experiments. This method does not inject additional systematic variation but does allow for all the variations that occur in MC. Instead, it uses random proportions of $W \to e\nu$, $\gamma + jet$, and $Z\gamma \to \nu\nu\gamma$ MC to check how the fitter responds when supplied with distributions which deviate from expectations over a variety of input values of $\langle t^{WV}_{corr} \rangle$.

6.2.1 Ideal Distributions

Our first validation method uses ideal distributions with systematic uncertainties created according to the parameters found by the sideband fit in Table 6.2 in the first step and the statistical variation in the second step. First, $\langle t^{WV}_{corr} \rangle$ is set to the fit value of 0.23 ns and $RMS\langle t^{0}_{corr} \rangle$ is set to the nominal value of 1.6 ns. Next we draw values for $\langle t^{RV}_{corr} \rangle$, $RMS\langle t^{RV}_{corr} \rangle$, $RMS\langle t^{WV}_{corr} \rangle$, and $\langle t^{0}_{corr} \rangle$ according to the nominal values and the systematic uncertainties listed in Table 5.5. We then create Gaussian distributions for t^{RV}_{corr}, t^{WV}_{corr}, and t^{0}_{corr} and uniform distributions for both good-vertex and no-vertex cosmic ray events. Each of these distributions is normalized to the appropriate multiplicity found by the sideband fit.

Next, we integrate each distribution into bins to create histograms and Poisson vary each bin to take into account statistical variations. Finally, the good-vertex cosmic ray, t^{RV}_{corr}, and t^{WV}_{corr} histograms are added together to create the good-vertex distribution. Similarly, the no-vertex cosmic ray and t^{0}_{corr} histograms are added together to create the no-vertex distribution. These pairs together constitute a single pseudo-experiment. They are then input into the fitter which determines values for $N^{Exp}_{(2,7)}$, σ_{Exp}, and $N^{Obs}_{(2,7)}$. From these, the pull is calculated. We see in Figure 6.2 that the mean of the pull distribution is close to zero, which indicates that the method has low bias. The RMS of the pull distribution is close to one, which indicates that

the fit uncertainty on the number of signal region events expected is well estimated.

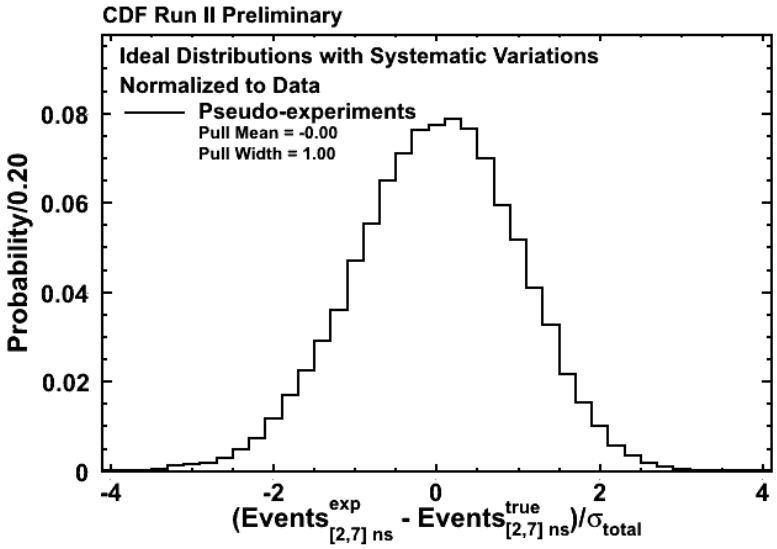

Figure 6.2: This figure shows the $N_{(2,7)}$ pull distribution for pseudo-experiments generated using Gaussian distributions for collision components and uniform distributions for cosmic ray components. We use the results of the fit in the sideband regions as the parameters of the generated distributions, and we vary all parameters with systematic uncertainties by those uncertainties. The pull distribution has a mean very close to zero, which indicates a lack of bias. It has an RMS very close to 1, which indicates that the fit uncertainty is well estimated.

Even though the results of the fit appear well behaved in bulk, we investigate how it behaves for certain ranges of input parameters. In particular, we would like to know if the fit remains well behaved as a function of the parameters within their systematic uncertainties, $\langle t^{RV}_{corr} \rangle$, $RMS\langle t^{RV}_{corr} \rangle$, $RMS\langle t^{WV}_{corr} \rangle$, and $\langle t^{0}_{corr} \rangle - \langle t^{WV}_{corr} \rangle$. We show the mean and width of the pull distribution as a function of each of the parameters in Figure 6.3. We find that the pull width is approximately one across a full sigma variation of each of these parameters, indicating that the fit uncertainty is well

estimated even for fairly large deviations from the parameters' nominal values. The pull mean is not constant as a function of the systematically constrained parameters; however, the bias increases by less than half a sigma after a full sigma variation for any of the parameters.

We can further investigate the robustness of this method by looking at a range of possible values for the parameters which we allow to float: $\langle t^{WV}_{corr} \rangle$ and $RMS\langle t^{0}_{corr} \rangle$. We run more ideal distribution pseudo-experiments where we still vary the systematically constrained parameters according to their systematic uncertainties, but this time we vary $\langle t^{WV}_{corr} \rangle$ and $RMS\langle t^{0}_{corr} \rangle$ across their full ranges seen in MC. We run once with $RMS\langle t^{0}_{corr} \rangle$ fixed at 1.6 ns and $\langle t^{WV}_{corr} \rangle$ varying from 0.0 ns to 0.8 ns. Then we run with $\langle t^{WV}_{corr} \rangle$ fixed at 0.23 ns and $RMS\langle t^{0}_{corr} \rangle$ varying from 1.4 ns to 1.8 ns. As shown in Figure 6.4, the fit remains unbiased and the uncertainties remain well estimated over the whole range. Therefore, the fit is robust for any reasonable variation in these parameters.

6.2.2 Full Monte Carlo

While we have determined that the combined likelihood fit method is unbiased, has well estimated uncertainties, and is robust using ideal distributions, we know that there is a limit to how well ideal distributions model real data. For instance, we know that the right, wrong, and no-vertex collision distributions are Gaussian to many sigma, but the combination of distributions from different collision sources are not. We have addressed this in Section 5.1.3, but it is important to verify that the systematic uncertainties we assigned cover the variation when using our full fitter.

To test the robustness of the full fitter with more realistic data, we construct pseudo-experiments using MC exclusive $\gamma + \not\!\!E_T$ control samples. We consider the three Standard Model backgrounds which span the range of possible wrong-vertex

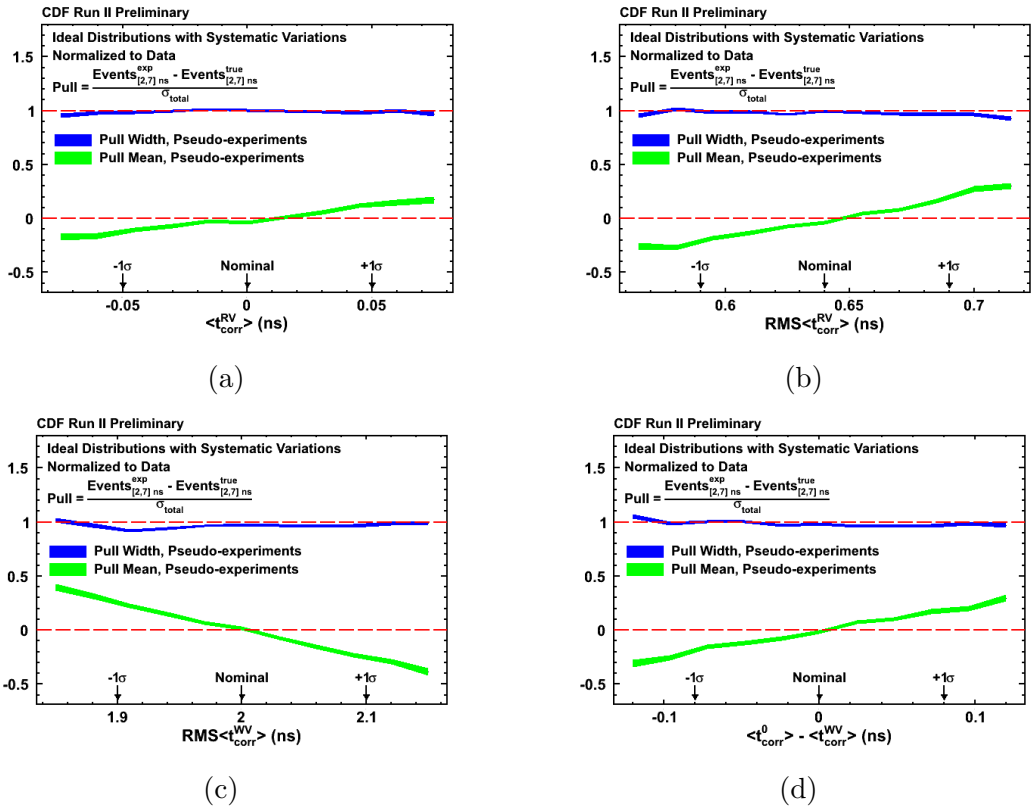

Figure 6.3: These figures show the $N_{(2,7)}$ pull mean and width as a function of variations in parameters with systematic uncertainties for pseudo-experiments generated using Gaussian distributions for collision components and uniform distributions for cosmic ray components. We use the results of the fit in the sideband regions as the parameters of the generated distributions, and we vary all parameters with systematic uncertainties by those uncertainties. In all cases, the bias in the $N_{(2,7)}$ pull distribution increases less than 1σ as the deviation from the nominal value increases by more than 1σ. (a) Right-vertex mean, (b) Right-vertex RMS, (c) Wrong-vertex RMS, (d) No-vertex mean - wrong-vertex mean

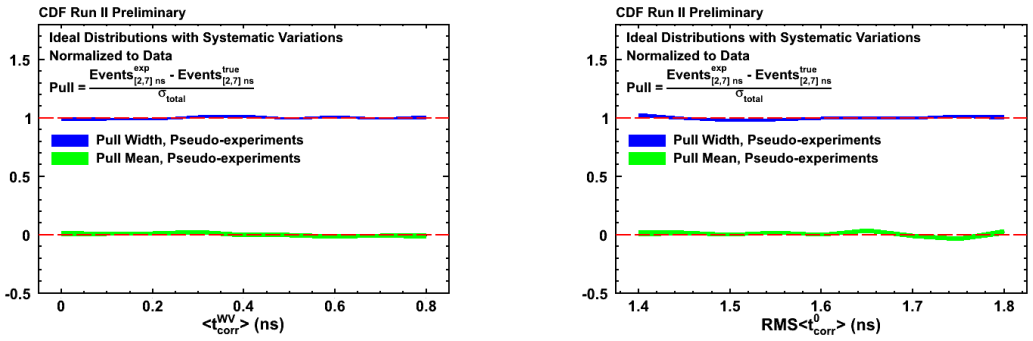

(a) (b)

Figure 6.4: These plots show that when the wrong-vertex mean and the no-vertex RMS vary a great deal, our estimation methods still work very well. We vary each separately and construct pseudo-experiments generated using Gaussian distributions for collision components and uniform distributions for cosmic ray components. We use the results of the fit in the sideband regions as the parameters of the generated distributions, and we vary all parameters with systematic uncertainties by those uncertainties. (a) For generated wrong-vertex means from 0.0 ns to 0.8 ns, the fit remains unbiased and the uncertainties remain well estimated. (b) For generated no-vertex RMSs from 1.4 ns to 1.8 ns, the fit remains unbiased and the uncertainties remain well estimated.

means, $W \to e\nu$ ($\langle t^{WV}_{corr} \rangle = 0.7$ ns), $\gamma + jet$ ($\langle t^{WV}_{corr} \rangle = 0.2$ ns), and $Z\gamma \to \nu\nu\gamma$ ($\langle t^{WV}_{corr} \rangle = 0.1$ ns). We construct right, wrong, and no-vertex samples from the full Monte Carlo samples where the right and wrong-vertex components are determined by selecting events if the highest ΣP_T vertex is well matched to the generated position of the collision. We scale the number of selected events from collision and cosmic ray components to match expectations from the sideband fit to data. We then generate an individual pseudo-experiment by Poisson varying the bins of the properly scaled components. We construct pseudo-experiments for each control sample individual, but we also create a combination pseudo-experiment by combining the drawn distributions from the three Standard Model backgrounds in random fractions.

Figure 6.5 shows fit results for $\langle t^{WV}_{corr} \rangle$ for all the three backgrounds individual as well as their combinations. Figure 6.6 shows fit results for $\langle t^{0}_{corr} \rangle - \langle t^{WV}_{corr} \rangle$, and we see that they agree within uncertainties as expected, always much less than the 80 ps systematic uncertainty taken. Figure 6.7 shows the fit uncertainty, and Figure 6.8 shows the pull distribution. The pull mean is ≤ 0.1 in all cases, even for random combinations, showing that the method is unbiased. The pull width is less than one showing that the fit uncertainties are, if anything, mildly over-estimated.

6.3 Results

Now that we have validated our background estimation techique, we discuss the results of the fit to the final exclusive $\gamma + \not\!\!E_T$ sample. Figure 6.9a shows the good-vertex t_{corr} distribution for the final sample zoomed in on the region (-10,10) ns on top of the predictions from the fit. To give a better sense of the agreement between data and prediction, Figure 6.9b shows the prediction with the fit uncertainty drawn as a yellow band around a solid black line. Similarly, Figure 6.10 shows observed data with the background prediction subtracted off on top of yellow and green bands

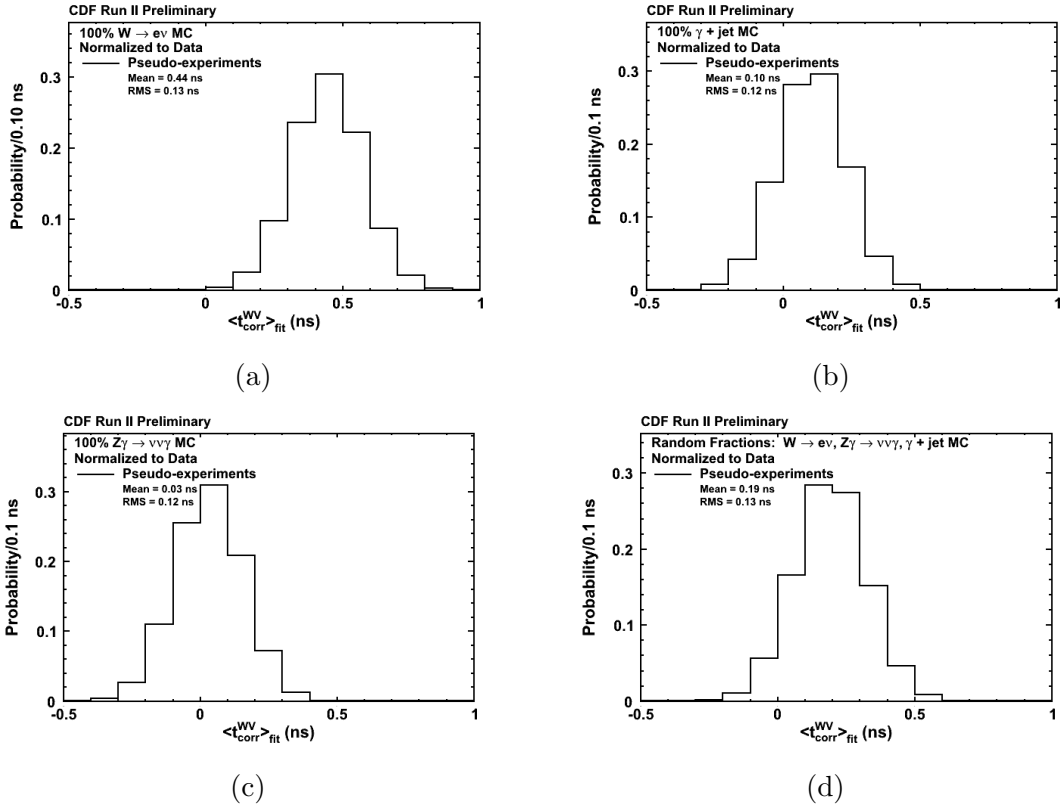

Figure 6.5: These figures show the fitted $\langle t^{WV}_{corr} \rangle$ distribution for pseudo-experiments derived from various full Monte Carlo samples. The number of right-vertex, wrong-vertex, no-vertex, and cosmic ray events are Poisson distributed around expectations from the sideband fit: (a) $W \to e\nu$, (b) γ + jet, (c) $Z\gamma \to \nu\nu\gamma$, (d) $W \to e\nu$, γ + jet, and $Z\gamma \to \nu\nu\gamma$ in random fractions. Note that the means are quite different for each sample, which shows that they span the space of $\langle t^{WV}_{corr} \rangle$ in our analysis.

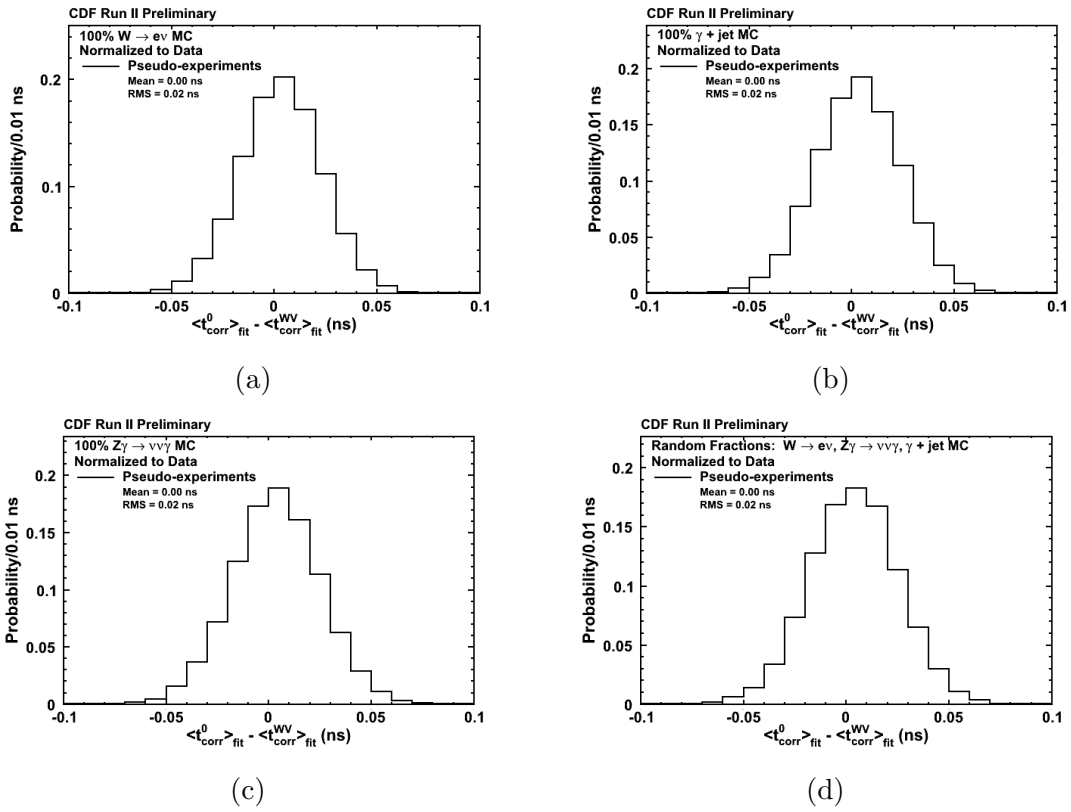

Figure 6.6: These figures show the fitted $\langle t^0_{corr} \rangle - \langle t^{WV}_{corr} \rangle$ distribution for pseudo-experiments derived from various full Monte Carlo samples. The number of right-vertex, wrong-vertex, no-vertex, and cosmic ray events are Poisson distributed around expectations from the sideband fit: (a) $W \to e\nu$, (b) γ + jet, (c) $Z\gamma \to \nu\nu\gamma$, (d) $W \to e\nu$, γ + jet, and $Z\gamma \to \nu\nu\gamma$ in random fractions. These are all centered at zero with an RMS of $\sim$0.02 ns which is small compared to the assumed 80 ps systematic uncertainty.

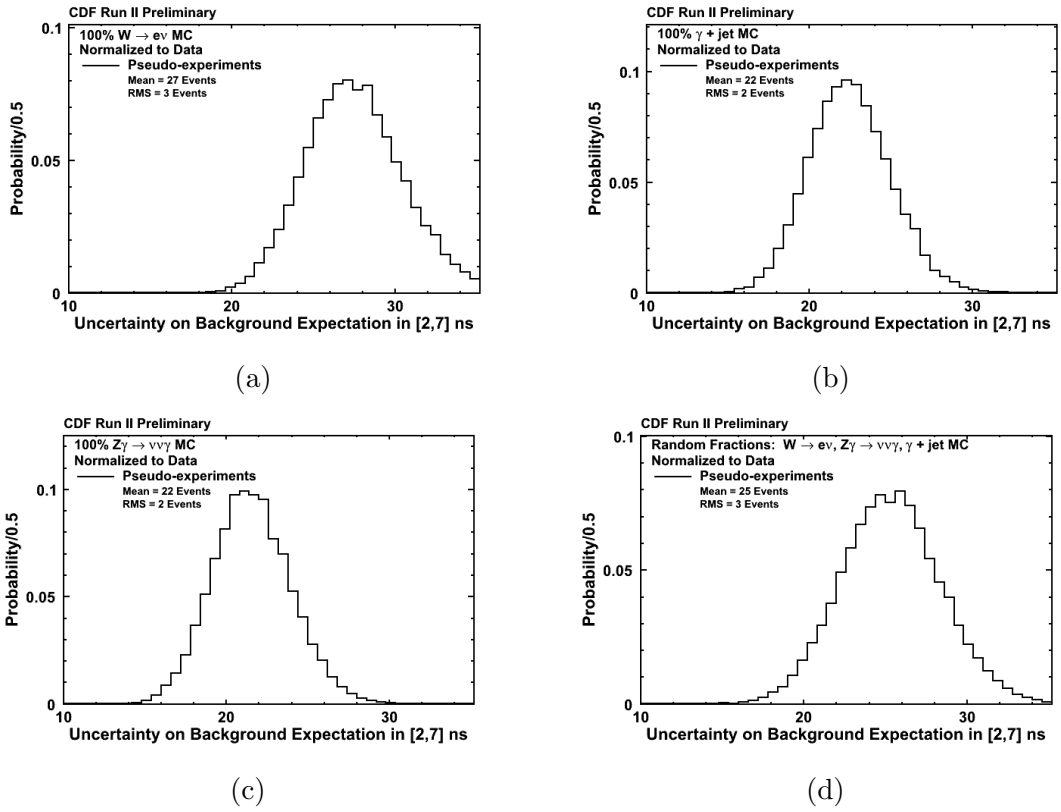

Figure 6.7: These figures show fit uncertainty on the $N_{(2,7)}$ prediction for pseudo-experiments derived from various full Monte carlo samples. The number of right-vertex, wrong-vertex, no-vertex, and cosmic ray events are Poisson distributed around expectations from the simple method. In all cases, the mean uncertainty is considerably smaller than the uncertainty seen in the simple method: (a) $W \to e\nu$, (b) γ + jet, (c) $Z\gamma \to \nu\nu\gamma$, (d) $W \to e\nu$, γ + jet, and $Z\gamma \to \nu\nu\gamma$ in random fractions. Note that the uncertainties are slightly larger when $\langle t_{corr}^{WV} \rangle$ is larger, but the values are typically in the 25 event range.

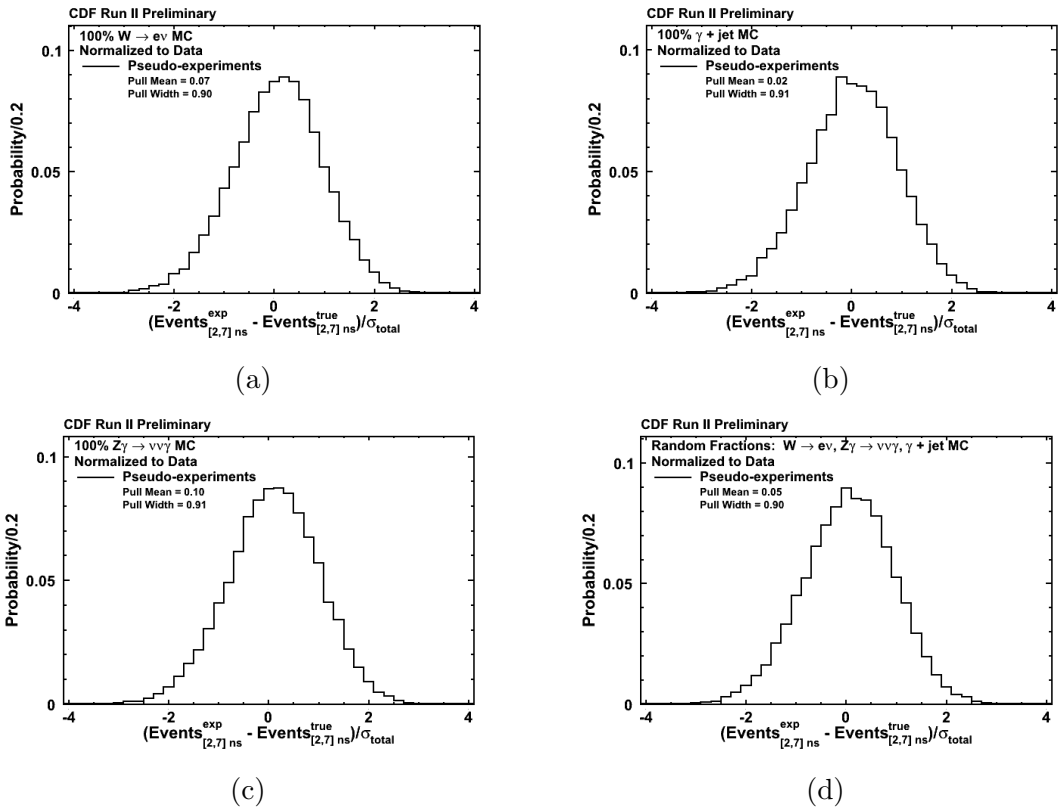

Figure 6.8: These figures show the $N_{(2,7)}$ pull distribution for pseudo-experiments derived from various full Monte carlo samples. The number of right-vertex, wrong-vertex, no-vertex, and cosmic ray events are Poisson distributed around expectations from the sideband fit. In all cases, the mean of the pull distribution is close to zero, which indicates a lack of bias. The RMS of the pull distribution is less than one, which indicates that the fit uncertainty is slightly over-estimated: (a) $W \to e\nu$, (b) γ + jet, (c) $Z\gamma \to \nu\nu\gamma$, (d) $W \to e\nu$, γ + jet, and $Z\gamma \to \nu\nu\gamma$ in random fractions.

representing the 1σ and 2σ uncertainties on the background prediction.

We see in Figure 6.9a that in the signal region, most bins are above expectations as would be expected of a signal from new physics. We observe 322 events in the signal region, and the fit predicts 287 $\pm$24 events. The full results are summarized in Table 6.2. As shown in Table 6.3, we find that the estimated background contributions in the signal region are 159 ± 4 cosmic ray events, 126 ± 24 wrong-vertex events, and 1.0 ± 0.6 right-vertex events. To be conservative, we estimate the significance of the excess using a simple counting experiment over the entire signal region. To do this, we determine the probability that the prediction could fluctuate to give a result at least as large as the observation using Monte Carlo methods. We draw each trial from a Gaussian distribution with a mean of the expected number of events in the signal region and an RMS of the fit uncertainty. We then Poisson vary that drawn number. The trial is marked as a success if the Poisson varied number is greater than or equal to the observed number of events in the signal region. The fraction of successes is the one sided p-value which can be straightforwardly converted into a significance. We find that the excess has a significance of 1.2σ, which is too small to justify a rejection of the null hypothesis.

6.4 Comparison to the Preliminary 2008 Results

This dissertation initially set out to answer the question of whether or not the excess seen in the 2008 preliminary result was real. After a thorough investigation, we have found that not only was the assumption that $\langle t^{WV}_{corr} \rangle = 0$ ns used in that analysis not valid, but there are a number of biases causing collision backgrounds to have large values of $\langle t^{WV}_{corr} \rangle$ as well as non-Gaussian tails. After developing new requirements to reduce the non-Gaussian tails in the t^{WV}_{corr} distribution, correctly taking in to account that $\langle t^{WV}_{corr} \rangle$ is greater than zero, and finding new methods for

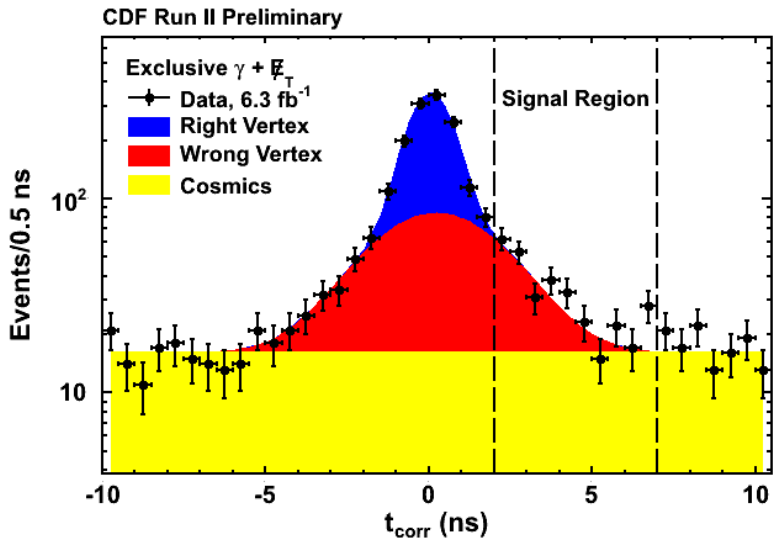

(a)

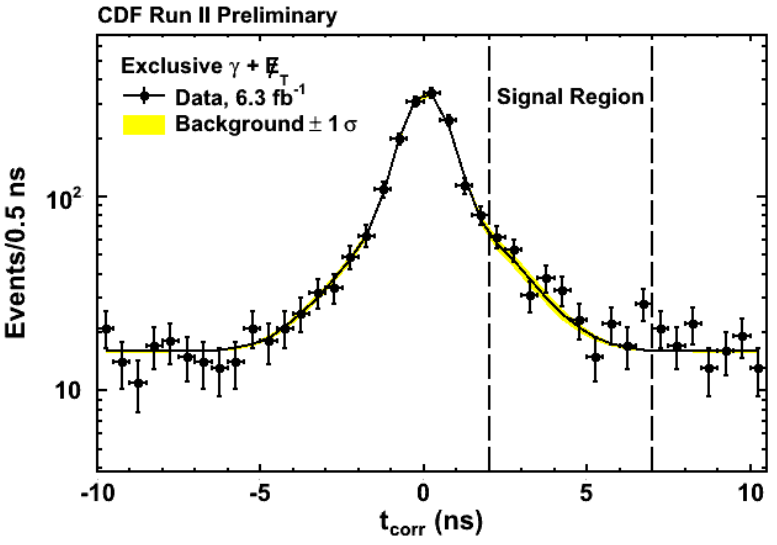

(b)

Figure 6.9: (a) The sideband fit results on the good-vertex data zoomed in to see the signal region. (b) The sideband fit results with a yellow band showing the combined statistical and systematic fit uncertainty.

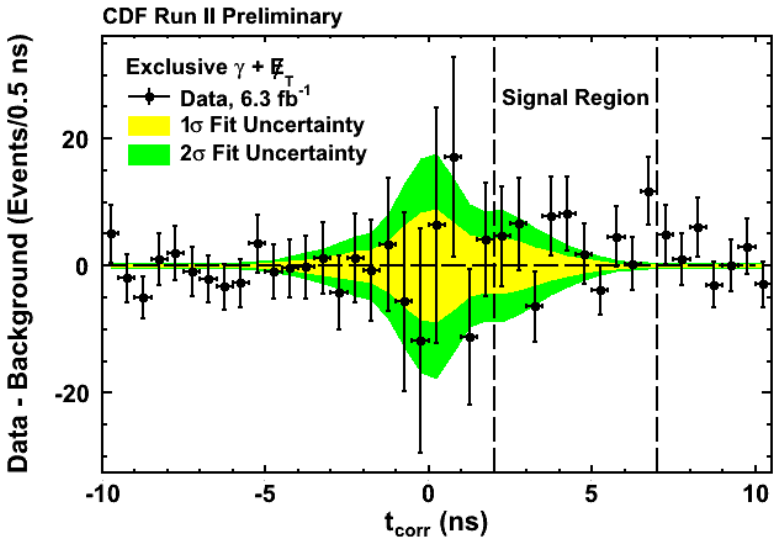

Figure 6.10: This shows the good vertex data with the background estimated with the sideband fit subtracted out. The yellow (green) band shows the 1σ (2σ) combined statistical and systematic fit uncertainty.

CDF Run II Preliminary $\int \mathcal{L} = 6.3\ \text{fb}^{-1}$

	Signal $2 < t_{\text{corr}} < 7$ **ns**	**RV Sideband** $-2 < t_{\text{corr}} < 2$ **ns**	**WV Sideband** $-7 < t_{\text{corr}} < -2$ **ns**
Right Vertex	1.0 ± 0.6	873 ± 65	0.6 ± 0.4
Wrong Vertex	126 ± 24	460 ± 60	89 ± 11
Cosmics	159 ± 4	128 ± 3	159 ± 4
Total Estimation	286 ± 24	1461 ± 38	249 ± 11
Data	322	1463	241

Table 6.3: The number of events predicted and observed in our three regions of interest. The total event expectations in the signal region is 286 ± 24; we observe 322 events in the data. This gives a modest 1.2σ excess. Note that the two sideband regions are determined using the fit, but are included here for completeness.

estimating its value in our data sample, we find that while an excess remains, it is no longer statistically significant, as demonstrated in the counting experiment.

To understand what happened to the previous excess, we consider the impact of some of the new requirements we added. First, the $\Delta R_{\rm pull}$ requirement was designed to reject fake photons primarily coming from $W \to e\nu$ where a hard interaction caused the electron track to be lost. Monte Carlo studies suggested that $W \to e\nu \to \gamma_{fake} + \not\!\!E_T$ was both the largest and the most highly biased background. Figure 6.11a shows the t_{corr} distribution of events which were rejected from our final data sample due to failing the $\Delta R_{\rm pull}$ requirement. We can see that these events have a very large $\langle t_{corr}^{WV} \rangle$ of $\sim$0.5 ns. Similarly, the large $|Z|$ veto was designed to reject events where the photon was produced outside the luminous region of the beam because these events typically have very large times. Figure 6.11b shows the t_{corr} distribution for events which were rejected from our final data sample due to failing the large $|Z|$ veto. While there are not many of these events, the distribution is even more heavily biased with a $\langle t_{corr}^{WV} \rangle$ of 1.4 ns.

Although we significantly reduced the bias of the final sample, some bias still remained. Therefore, perhaps the most important change was moving to a new background estimation method which takes into consideration that $\langle t_{corr}^{WV} \rangle$ is greater than zero. To determine how important this change was, we modify our estimation method to use only the good-vertex data sideband regions and hold $\langle t_{corr}^{WV} \rangle$ fixed to zero, with zero uncertainty. The results of this fit are shown in Figure 6.12. If we had performed the background estimation this way, we would have estimated the background contribution to the signal region to be 256 ± 14 events which corresponds to an excess with a significance of 3.0σ.

Next, we will conclude this dissertation with a discussion of the results and possible future improvements to the analysis.

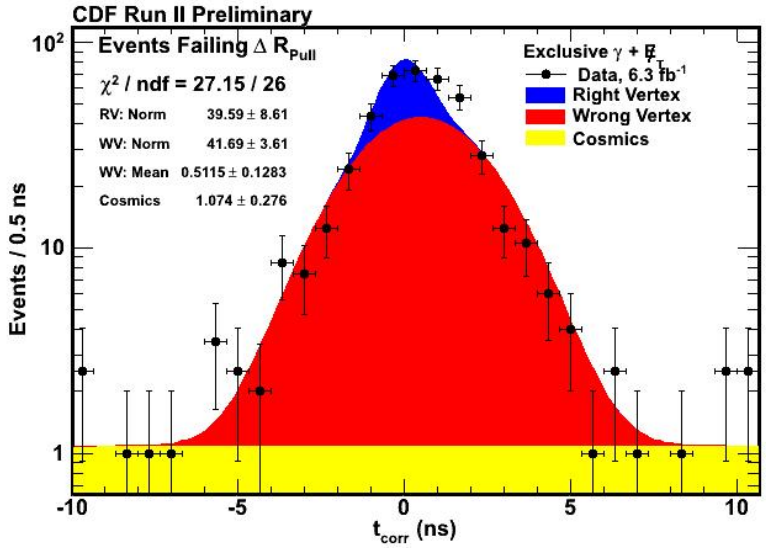

(a)

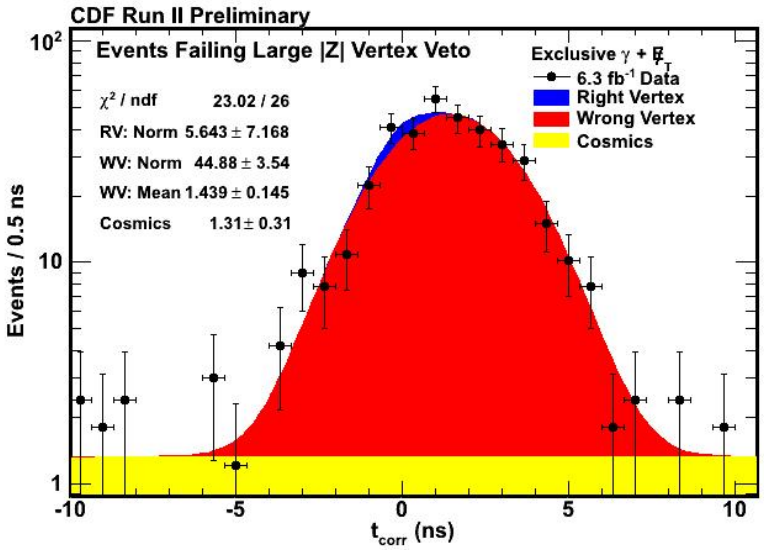

(b)

Figure 6.11: (a) The t_{corr} distribution for exclusive $\gamma + \not\!\!E_T$ events in data passing all requirements in Table 4.6 but failing the $\Delta R_{\rm pull}$ requirement. These events are likely to be fake photons and have a larger $\langle t^{WV}_{corr} \rangle$ than our final data sample. (b) The t_{corr} distribution for exclusive $\gamma + \not\!\!E_T$ data events passing all requirements in Table 4.6 but failing the large $|Z|$ veto. In addition, the $\Delta R_{\rm pull}$ requirement is not applied. These events have an extremely large $\langle t^{WV}_{corr} \rangle$.

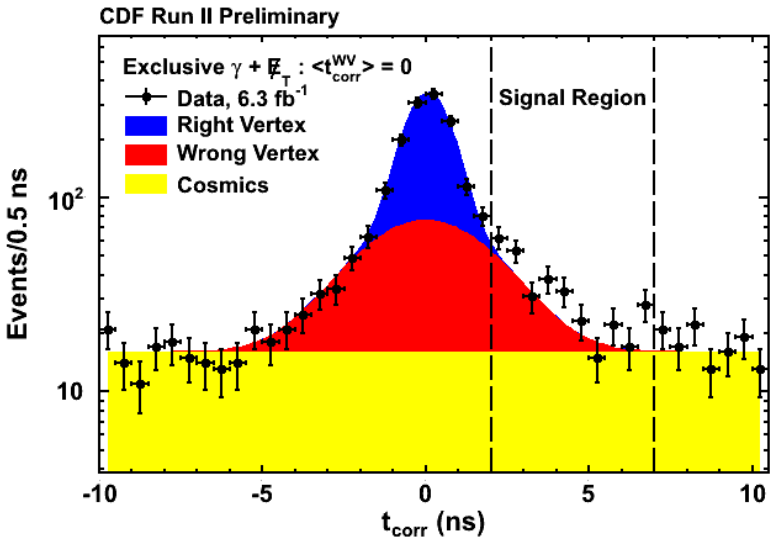

Figure 6.12: The t_{corr} distribution for exclusive $\gamma + \not\!\!E_T$ events fit using the new background estimation method except $\langle t^{WV}_{corr} \rangle$ is inappropriately fixed to be zero for illustrative purposes. This approximates the background estimation from the 2008 preliminary result. Using this method yields an inappropriately high significance of 3.0σ.

7. CONCLUSIONS

7.1 Summary of the Search

This dissertation has presented an investigation of an excess of events with delayed photons in the exclusive $\gamma + \not\!\!E_T$ final state as observed in proton anti-proton collisions with a center-of-mass energy of 1.96 TeV. We have determined that the most difficult to understand backgrounds in this final state are Standard Model collision background sources because they are capable of producing reconstructed photons with large corrected times due to timing biases in events where the wrong vertex is selected. We have developed new requirements which minimize, but do not eliminate, these biases. To account for the remaining biases, we developed a new background estimation technique which measures the wrong-vertex mean using an orthogonal sample, events with no reconstructed vertex. We analyzed data taken from December 2004 to June 2010 with an integrated luminosity of 6.3 ± 0.4 fb^{-1} and observed 322 events in the signal while our new background estimation method predicted 287 ± 24 events. While the events in the signal region all appear to be above expectations, we simply use a counting experiment to quantify the significance of this excess to be only 1.2σ.

We conclude that the bulk of the excess seen in the 2008 preliminary analysis was primarily due to not rejecting the most biased collision backgrounds as well as using its incorrect assumptions in performing the background estimation. Despite the low significance of our result, we note that the shape of the excess is consistent with the presence of an exponentially distributed signal. Therefore, we believe there is value in revisiting this final state with the full Tevatron dataset and using more sophisticated techniques for comparing data and backgrounds in the future.

If this is done, there are several potential analysis improvements. First, no attempt was made to optimize selection requirements for $h^0 \to \widetilde{\chi}_1^0\widetilde{\chi}_1^0 \to \gamma\widetilde{G}\gamma\widetilde{G}$ production since we were investigating a previous excess. Some options are increasing acceptance through lowering the photon E_T^0 threshold or allowing the presence of an additional calorimeter cluster as long as it was consistent with a photon to allow for the possibility that the second $\widetilde{\chi}_1^0$ decayed inside the detector. Preliminary studies indicate this would increase acceptance, although no studies exist on what it would do to the background rate.

Another option is to raise the ΣP_T requirement for space-time vertices as this could improve the analysis in a number of ways. The vertex chosen for wrong-vertex events and cosmic ray events typically comes from a minimum bias collision. Such collisions have lower ΣP_T on average than hard collisions; therefore, increasing the ΣP_T requirement would reduce the wrong vertex and cosmic ray rates. Moreover, the events with newly rejected vertices would enter the no-vertex sample where they would assist in improving the estimate of the wrong-vertex mean. However, before undertaking such an analysis, an estimate of what this would do to any expected signal would need to be understood.

Finally, we note that almost all bins in the signal region are above expectations; however, the total number of events in the signal region is dominated by the region very close to 2 ns. This indicates that the counting experiment combining all information about the signal region into a single bin is not fully sensitive to the consistent excess across bins. This suggests comparing the data in the signal region to the expectations using a shape significance instead of a counting significance.

Ultimately, the excess of delayed photons in the exclusive $\gamma + \not\!\!E_T$ final state is a tantalizing hint, but it is not large enough to claim evidence of any physics. We encourage others to follow up on this result with more data and improved techniques.

We also believe that there is value in studying how to do this search at the LHC. Only time will tell if this was just a fluctuation, a mis-measurement, or the first indication of new physics.

REFERENCES

[1] D. Griffiths, *Introduction to Elementary Particles* (WILEY-VCH Verlag GmbH, Weinheim, Germany, 2008), 2nd ed.

[2] T. Aaltonen, V. M. Abazov, B. Abbott, B. S. Acharya, M. Adams, et al. (CDF and DØ Collaborations), Phys. Rev. Lett. **109**, 071804 (2012).

[3] G. Aad, T. Abajyan, B. Abbott, J. Abdallah, S. A. Khalek, et al. (ATLAS Collaboration), Phys. Lett. **B 716**, 1 (2012); S. Chatrchyan, V. Khachatryan, A. Sirunyan, A. Tumasyan, W. Adam, et al. (CMS Collaboration), Phys. Lett. **B 716**, 30 (2012).

[4] G. W. Bennett, Phys. Rev. Lett. **92**, 161802 (2004).

[5] Y. Fukuda, T. Hayakawa, E. Ichihara, K. Inoue, K. Ishihara, et al. (Super-Kamiokande Collaboration), Phys. Rev. Lett. **81**, 1562 (1998).

[6] E. Komatsu, K. M. Smith, J. Dunkley, C. L. Bennett, B. Gold, G. Hinshaw, N. Jarosik, D. Larson, M. R. Nolta, L. Page, et al., Astrophys. J. Suppl. **192**, 18 (2011); G. Bertone, D. Hooper, and J. Silk, Phys. Rept. **405**, 279 (2005).

[7] R. Blair, K. Byrum, J. Dawson, V. Guarino, S. Kuhlmann, et al. (CDF Collaboration), Fermilab Report FERMILAB-PUB-96-390-E (1996).

[8] S. Martin (1997), v6 revised 2011, `arXiv:hep-ph/9709356`.

[9] K. Lane (1994), `arXiv:hep-ph/9401324v2`; S. Martin, Phys. Rev. **D 46**, 2192 (1992), `arXiv:hep-ph/9204204v2`; M. Schmaltz and D. Tucker-Smith, Ann.Rev.Nucl.Part.Sci. **55**, 229 (2005).

[10] C. Kolda and H. Murayama, JHEP **07**, 035 (2000).

[11] H. Nishino, K. Abe, Y. Hayato, T. Iida, M. Ikeda, et al. (The Super-Kamiokande Collaboration), Phys. Rev. D **85**, 112001 (2012).

[12] J. Beringer, J.-F. Arguin, R. Barnett, K. Copic, O. Dahl, et al. (PDG), Phys. Rev. **D 86**, 010001 (2012).

[13] R. Arnowitt and P. Nath (1997), `arXiv:hep-ph/9708254`.

[14] F. Paige and J. Wells (2000), `arXiv:hep-ph/0001249`.

[15] C. Kolda, Nucl.Phys.Proc.Suppl. pp. 266–275 (1998).

[16] J. D. Mason and D. Toback, Phys. Lett. **B 702**, 377 (2011).

[17] D. Toback and P. Wagner, Phys. Rev. **D 70**, 114032 (2004).

[18] B. C. Allanach, M. Battaglia, G. A. Blair, M. Carena, A. D. Roeck, et al., Eur. Phys. J. **C 25**, 113 (2002).

[19] A. Heister, S. Schael, R. Barate, R. Bruneliere, I. D. Bonis, et al., Eur. Phys. J. **C 25**, 339 (2002), ISSN 1434-6044; M. Gataullin, S. Rosier, L. Xia, and H. Yang, AIP Conf. Proc. **903**, 217 (2007); G. Pasztor, PoS **HEP2005**, 346 (2005); J. Abdallah, P. Abreu, W. Adam, P. Adzic, T. Albrecht, et al. (DELPHI Collaboration), Eur. Phys. J. **C 38**, 395 (2005).

[20] T. Aaltonen, J. Adelman, B. Álvarez González, S. Amerio, D. Amidei, et al. (CDF Collaboration), Phys. Rev. Lett. **104**, 011801 (2010); V. M. Abazov, B. Abbott, M. Abolins, B. S. Acharya, M. Adams, et al. (D0 Collaboration), Phys. Rev. Lett. **105**, 221802 (2010).

[21] A. Abulencia, J. Adelman, T. Affolder, T. Akimoto, M. G. Albrow, et al. (CDF Collaboration), Phys. Rev. Lett. **99**, 121801 (2007).

[22] S. Chatrchyan, V. Khachatryan, A. M. Sirunyan, A. Tumasyan, W. Adam, et al. (CMS Collaboration), Phys. Rev. Lett. **106**, 211802 (2011); G. Aad, B. Abbott, J. Abdallah, A. A. Abdelalim, A. Abdesselam, et al. (ATLAS Collaboration), Phys. Rev. Lett. **106**, 121803 (2011).

[23] P. Meade, N. Seiberg, and D. Shih, Progr. Theoret. Phys. Suppl. **177**, 143 (2009); L. M. Carpenter, M. Dine, G. Festuccia, and J. D. Mason, Phys. Rev. **D 79**, 035002 (2009); M. Buican, P. Meade, N. Seiberg, and D. Shih, JHEP **2009**, 016 (2009); Z. Komargodski and N. Seiberg, JHEP **2009**, 072 (2009); A. Rajaraman, Y. Shirman, J. Smidt, and F. Yu, Phys. Lett. **B 678**, 367 (2009).

[24] J. D. Mason, D. E. Morrissey, and D. Poland, Phys. Rev. D **80**, 115015 (2009).

[25] T. Aaltonen, J. Adelman, B. Álvarez González, S. Amerio, D. Amidei, et al. (CDF Collaboration), Phys. Rev. **D 82**, 052005 (2010).

[26] M. Goncharov, T. Kamon, V. Khotilovich, V. Krutelyov, S. Lee, et al., Nucl. Instrum. Meth. **A565**, 543 (2006).

[27] T. A. Division, *Operations rookie books*, `http://www-bdnew.fnal.gov/operations/rookie_books/rbooks.html` (Accessed 2012).

[28] S. Holmes, R. S. Moore, and V. Shiltsev, J. Inst. **6**, T08001 (2011).

[29] R. Thurman-Keup, C. Bhat, W. Blokland, J. Crisp, N. Eddy, et al., Journal of Instrumentation **6**, T10004 (2011).

[30] A. Sill (CDF Collaboration), Nucl. Instrum. Meth. **A447**, 1 (2000).

[31] T. Affolder, D. Allspach, D. Ambrose, J. Bialek, W. Bokhari, et al., Nucl. Instrum. Meth. **A526**, 249 (2004).

[32] A. Bhatti, F. Canelli, B. Heinemann, J. Adelman, D. Ambrose, et al., Nucl. Instrum. Meth. **566**, 375 (2006).

[33] L. Balka, K. Coover, R. Diebold, W. Evans, N. Hill, et al., Nucl. Instrum. Meth. **A267**, 272 (1988).

[34] A. Elagin, P. Murat, A. Pranko, and A. Safonov (2012), submitted to Nucl. Instrum. Meth., `arXiv:1207.4780`.

[35] M. Martens and P. Bagley, *Luminosity distribution during collider Run II*, `http://www-ap.fnal.gov/~martens/luminosity/beam_size.html` (Accessed 2012).

[36] J. F. Arguin, B. Heinemann, and A. Yagil, CDFNote 6238 (2002), unpublished.

[37] D. Toback, Ph.D. thesis, University of Chicago (1997); J. Berryhill, Ph.D. thesis, University of Chicago (2000); Y. Liu, Ph.D. thesis, Université de Genève (2004).

[38] S. Dube, J. Zhou, and S. Somalwar, CDFNote 8321 (2006), unpublished.

[39] M. Goncharov, V. Krutelyov, D. Toback, and P. Wagner, CDFNote 8015 (2006), unpublished.

[40] A. P. Dempster, N. M. Laird, and D. B. Rubin, J. R. Stat. Soc. Ser. B Stat. Methodol. **39**, pp. 1 (1977).

[41] J. Asaadi, A. Aurisano, D. Goldin, J. Nett, and D. Toback, CDFNote 10607 (2012), unpublished.

[42] J. Asaadi, Ph.D. thesis, Texas A&M University, College Station, Texas (2012).

[43] S. D'Auria, A. Dominguez, J. Nielsen, P. Murat, F. Prakoshyn, et al., CDFNote 7055 (2004), unpublished.

[44] T. Sjostrand, P. Eden, C. Friberg, L. Lonnblad, G. Miu, et al., Comput. Phys. Commun. **135**, 238 (2001).

[45] U. Baur, T. Han, and J. Ohnemus, Phys. Rev. **D 57**, 2823 (1998).

[46] R. Brun, F. Bruyant, M. Maire, A. McPherson, and P. Zanarini, CERN Report CERN-DD-EE-84-1 (1987).

[47] M. Goncharov, D. Toback, P. Wagner, and V. Krutelyov, CDFNote 7928 (2006), unpublished.

[48] M. Goncharov, V. Krutelyov, D. Toback, P. Wagner, R. Culbertson, and A. Pronko, CDFNote 7960 (2006), unpublished; M. Goncharov, V. Krutelyov, D. Toback, P. Wagner, R. Culbertson, and A. Pronko, CDFNote 8409 (2006), unpublished.

[49] G. Cowan, *Statistical Data Analysis* (Oxford University Press, New York, NY, 1998).

[50] J. Conway (2011), `arXiv:1103.0354v1`.

APPENDIX A

TIMING CORRECTIONS

Because the number of events in the signal region is highly sensitive to the wrong-vertex mean, it is very important to have well calibrated timing. It is necessary to calibrate t_0 for tracks to be used by space-time vertexing, the t_i of vertices themselves, and the EMTiming system that measures the time of arrival. The full t_{corr} calculation must have systematic deviations that are small compared to the overall wrong-vertex mean. We derive calibrations using $e + \not\!\!E_T$ data events which can mimic the $\gamma + \not\!\!E_T$ final state when the electron track is ignored during vertexing with requirements listed in Table A.1. To ensure we are calibrating the sample using the correct vertex, we use the electron track to help us identify events where the right vertex has the highest ΣP_T using the requirements $|Z_{trk} - Z_{vtx}| < 3.0$ cm and $|t_{trk} - t_{vtx}| < 1.8$ cm.

Requirement	**Selection Cut**
Trigger and good run	See Tables 2.1 and 2.2
Good electron requirements	See Table 2.7
E_T^0	> 30 GeV
$\not\!\!E_T^0$	> 30 GeV
Beam halo veto	See Table 3.4

Table A.1: The set of requirements to create the $W \to e\nu \to e + \not\!\!E_T$ calibration and validation sample. Space-time vertices are reconstructed ignoring the electron track. This sample uses inclusive requirements to increase statistics.

A.1 Track Timing and Calibration

We find that tracks deemed good for vertexing (Table 2.4) after the standard calibration procedures have large systematic variations in the average track time as a function of various track parameters. This has the potential to cause problems in two ways. First, badly calibrated tracks can cause the time of the vertex to be mismeasured and cause a systematic bias of the t_{corr} measurements. An equally important problem is that if the collision which produced the reconstructed photon produces many tracks and there are large systematic variation in the average track times, the vertexing algorithm can split those tracks into two separate, small ΣP_T space-time vertices. Because of this, neither vertex is likely to not be chosen as the highest ΣP_T vertex. If this happens often, it increases the fraction of events with wrong vertices, and thus increasing the number of background events in the signal region. Second, if such a split happens, even if one of the vertices is chosen as the highest ΣP_T vertex, it will have a mis-measured time on average.

As Figure A.1 shows, the COT has a different timing response for positive and negative tracks. This can be seen even more dramatically in Figure A.2, which shows the mean track time for positive and negative tracks separately as a function of track parameters and run number. The track parameters found by performing a helical fit are z_0, the origin of the track along the beam line; t_0, the start time of the track; η, the pseudo-rapidity of the track relative to its own starting point; $1/P_T$, a parameter related to the curvature of the helix; ϕ_0, the initial azimuthal angle of the track; and d_0, the point of closest approach to the beam line in the transverse plane. We do not consider z_0 because it is known that z_0 and t_0 are linearly correlated due to differing widths of the proton and antiproton bunches [21]. We also consider the parameter $T_0\sigma$, the estimated uncertainty on the t_0 measurement. Since the fitter measures

t_0 by using assuming that the particle is a pion, the larger the mass of the particle relative to the pion mass, the worse the t_0 estimate will be and the larger $T_0\sigma$ will be. Therefore, $T_0\sigma$ can be used to help calibrate or reject slow protons which are mis-measured due to being non-relativistic.

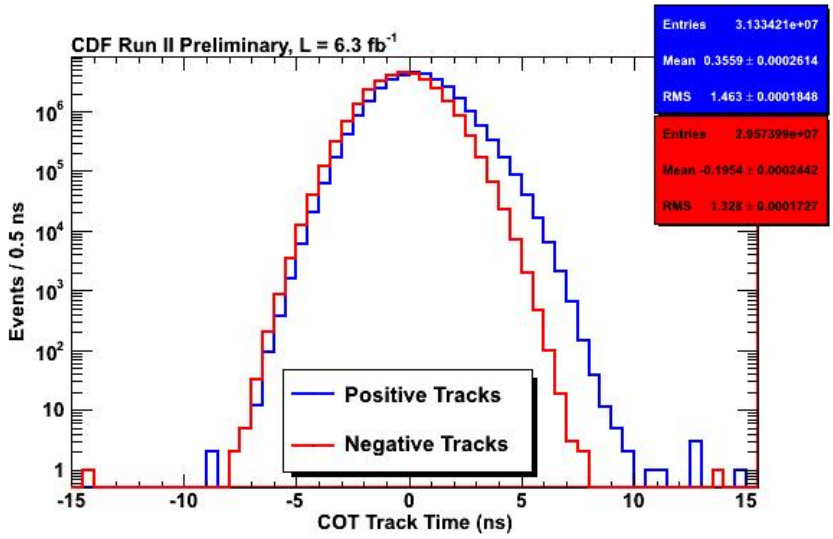

Figure A.1: The uncorrected t_0 for tracks with positive (blue) and negative (red) charges.

To perform this calibration, we perform a fit of the track t_0 to polynomials of $1/P_T$, η, ϕ_0, d_0, and $T_0\sigma$ with cross terms for positive and negative tracks separately in a given run. The overall track t_0 distribution after calibrations is shown in Figure A.3, and the average track t_0 as a function of the fit parameters is shown in Figure A.4. The calibration procedure clearly has reduced the systematic variations to less than 100 ps.

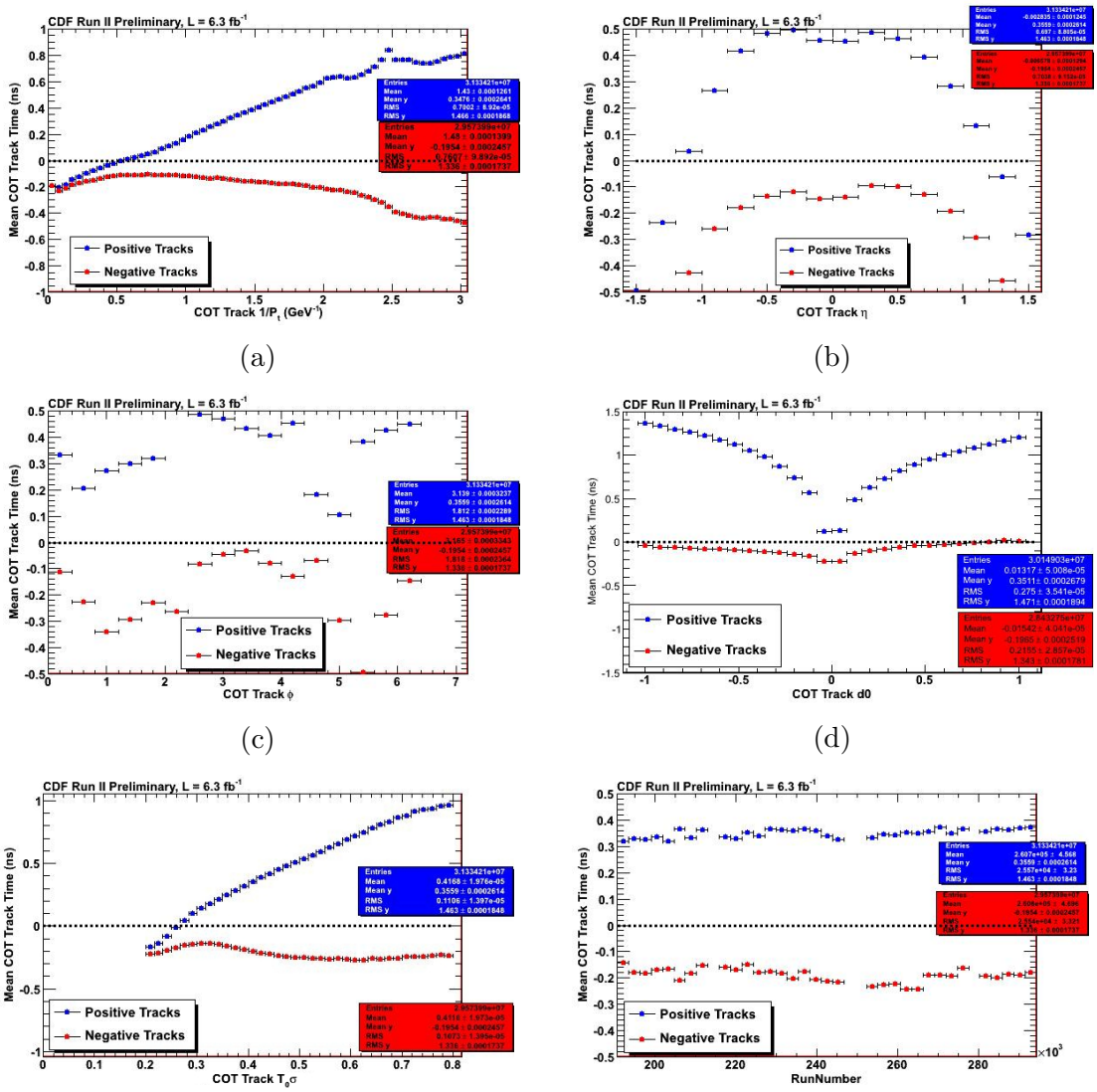

Figure A.2: The average uncorrected time for tracks with positive (blue) and negative (red) charges as a function of: (a) $1/P_T$, (b) η, (c) ϕ_0, (d) corrected d_0, (e) estimated t_0 uncertainty, and (f) run number.

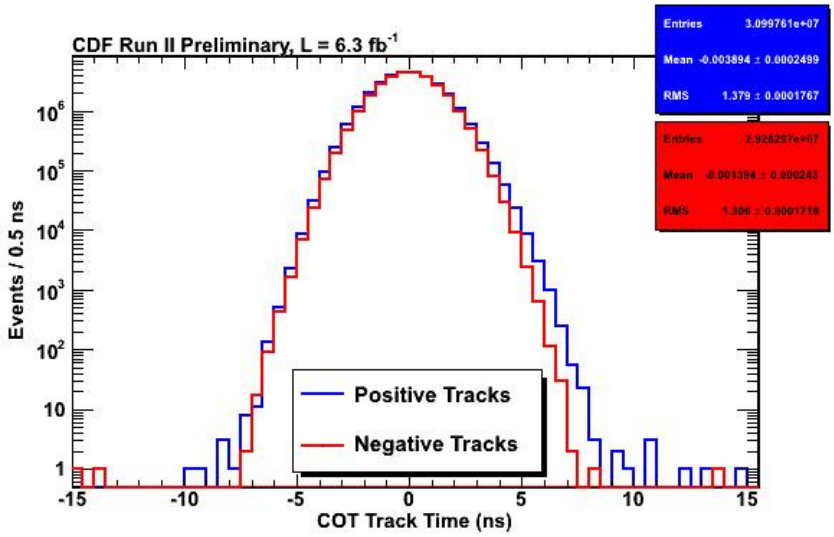

Figure A.3: The corrected time for tracks with positive (blue) and negative (red) charges.

A.2 Vertex Timing and Corrections

As described in Section 5.1.2, the mean t_{corr} of wrong-vertex events can be measured using the no-vertex sample. However, from Equation 5.8, we wee that this technique only works if we are confident that average vertex time for wrong vertices is zero. Even though we have calibrated track times, the clustering process could create a slight bias. Figure A.5 shows the vertex time for right vertices as well as the average vertex time for right vertices as a function of run number and vertex ΣP_T after track calibrations. Although the vertex time distribution appears Gaussian and well centered, we do find that there is some systematic variation in the mean.

We find that only correcting the mean vertex time as a function of run number is sufficient to remove all systematic variation. To do this, we simply calculate the mean vertex time for all right-vertex events in each run. Since the selection of right-vertex events depends both on the track time and the vertex time, after the first correction, we reselect all right-vertex events using the newly corrected track and

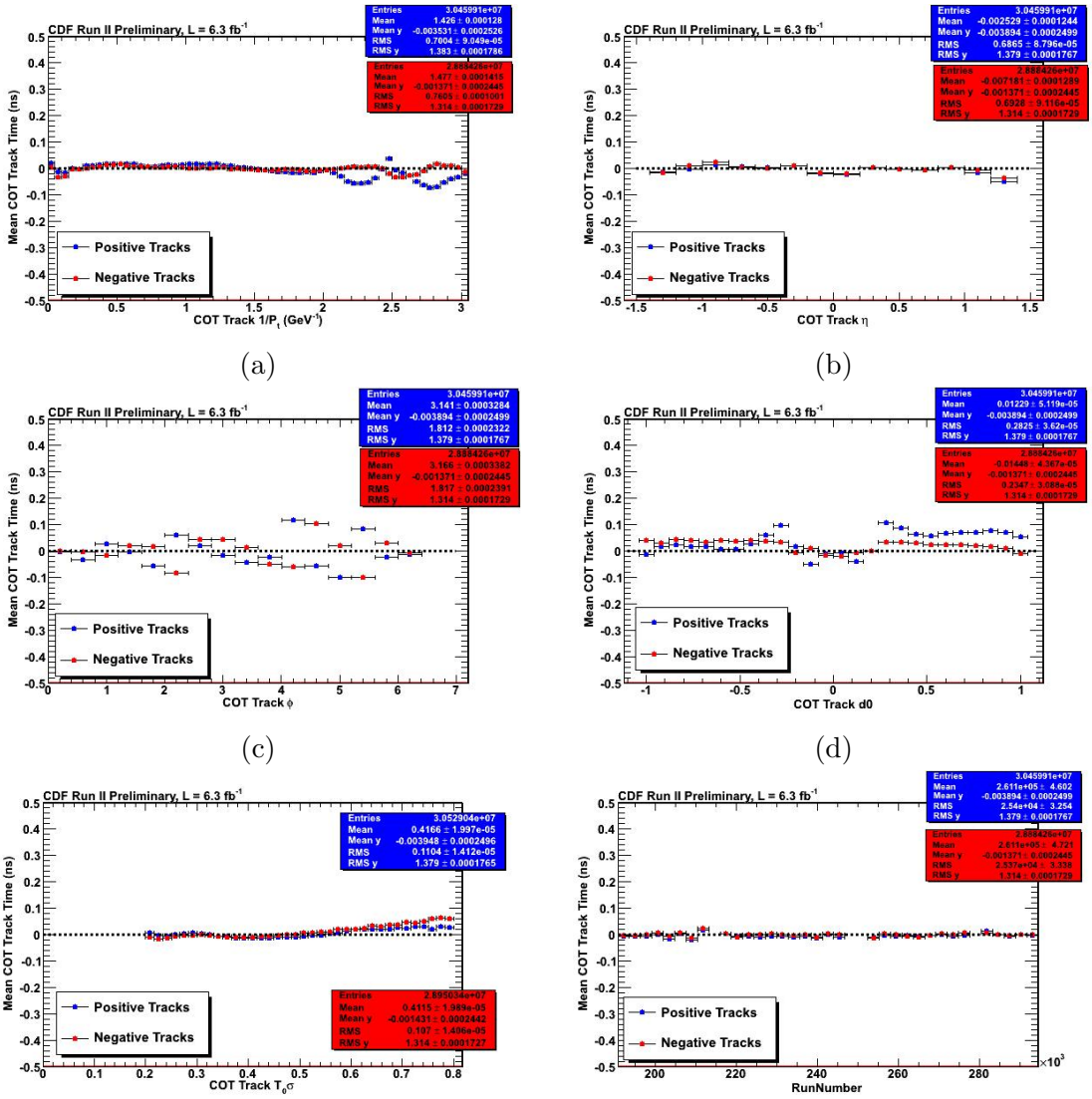

Figure A.4: The average corrected time for tracks with positive (blue) and negative (red) charges as a function of: (a) $1/P_T$, (b) η, (c) ϕ_0, (d) corrected d_0, (e) estimated t_0 uncertainty, and (f) run number. Note that the y-axis range here is much smaller than in Figure A.2.

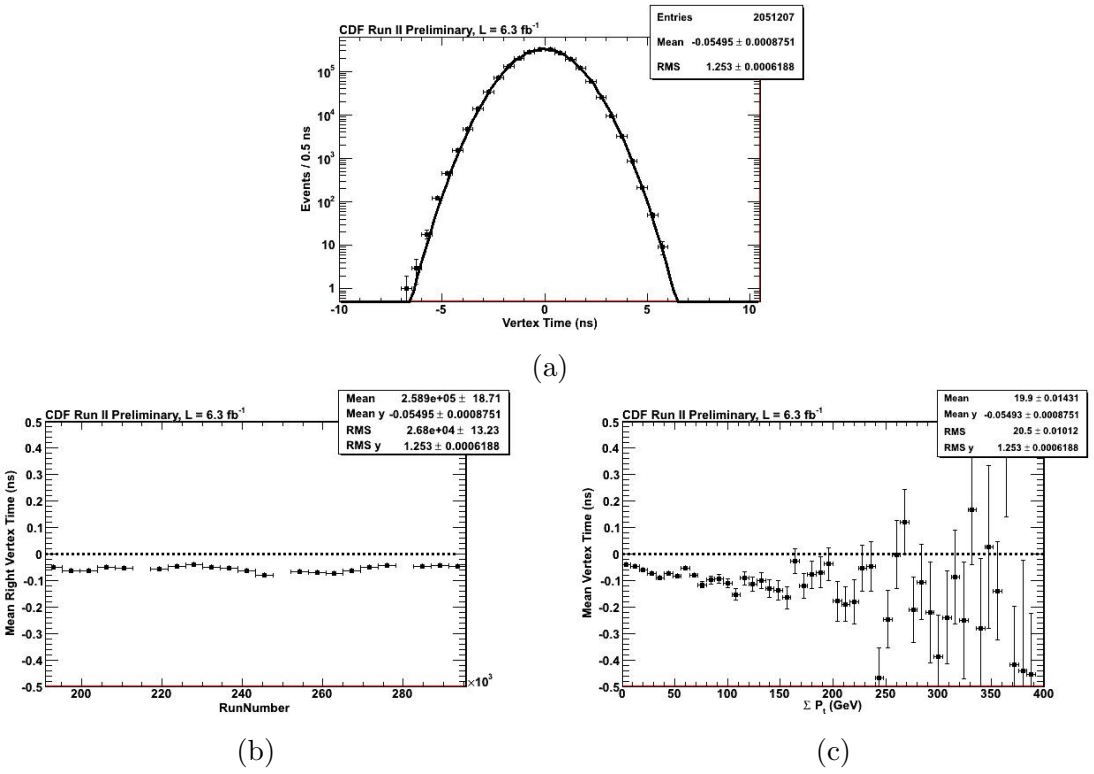

Figure A.5: (a) The distribution of t_0 for vertices after track corrections but before vertex corrections. (b) The average value as a function of run number. (c) The average value as a function of vertex ΣP_T.

vertex times. We iterate this process until the no run has an deviation of the average vertex time from zero of more than 100 ps. The results in Figure A.6 show that they systematic variations are significantly reduced, and the RMS is also slightly reduced.

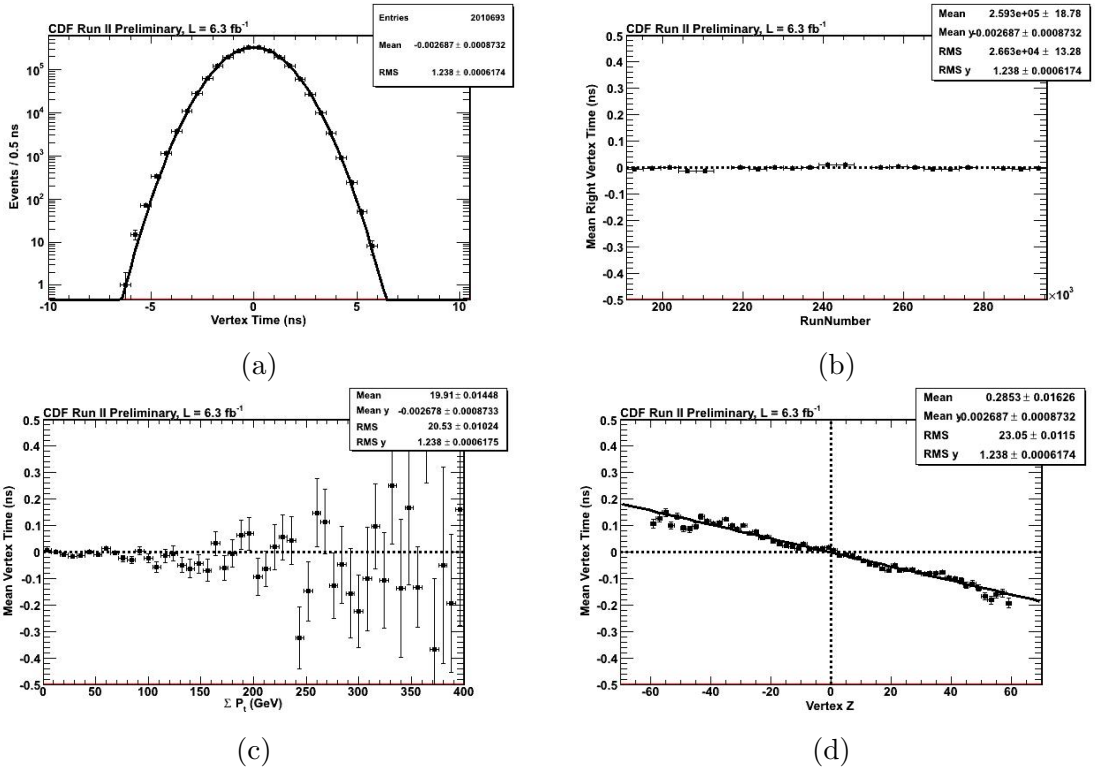

Figure A.6: (a) The distribution of the vertex time, t_0, after vertex corrections. (b) The average value as a function of run number. (c) The average value as a function of vertex ΣP_T. (d) The average corrected vertex time as a function of vertex Z. This dependence is a real effect due to the unequal widths of proton and anti-proton bunches.

A.3 EMTiming Measurements and Corrections

Finally, we calibrate the EMTiming system using our improved vertex measurement. Since we just modified the vertex timing, the vertex times and the photon

times are no longer calibrated relative to each other; however, calibrating EMTiming is a sensitive issue. While previous calibrations of the EMTiming system calibrated on t^0_{corr} to be vertex independent, we now know (Chapter 5) that $\langle t^0_{corr} \rangle$ has physical meaning and cannot be safely used to calibrate the detector. Therefore, we calibrate on t^{RV}_{corr} as it only involves detector effects, not physics effects.

Figure A.7 shows the average t_{corr} for right-vertex events as a function of electron energy, run number, and tower (a proxy for η but represents the physical tower in which a measurement is made) after the preliminary standard calibrations and the new track and vertex corrections. There are a number of effects that are readily observed.

The first issue is in the calibration of the EMTiming tower as a function of energy. The pulse emitted by the PMTs when an electron or photon deposit energy in the calorimeter has a finite rise time and a peak proportional to the amount of energy deposited. Because the EMTiming system uses a fixed-height discriminator, high energy deposits trigger the discriminator earlier than lower energy deposits. This is known as slewing, and the initial calibrations already account for it [26]; however, it is clear that the dependence is not fully removed.

A second effect is that the zero time that the EMTiming system begins counting from is distributed via a clock signal from the Fermilab main control room using a fiber optic connection. A drift in timing as a function of run number is believed to be due to the temperature dependence of the arrival time of the clock signal. A third effect is the variation as a function of detector η, or more specifically, the physical tower. The tower dependence is due to the fact that the initial calibrations use t^0_{corr} which assumes that the average collision that produced the sample of events that the tower was calibrated on had a vertex time and position of zero; however, the further the tower is from the center of the detector, the less likely the true collision occurred

at zero for geometric reasons.

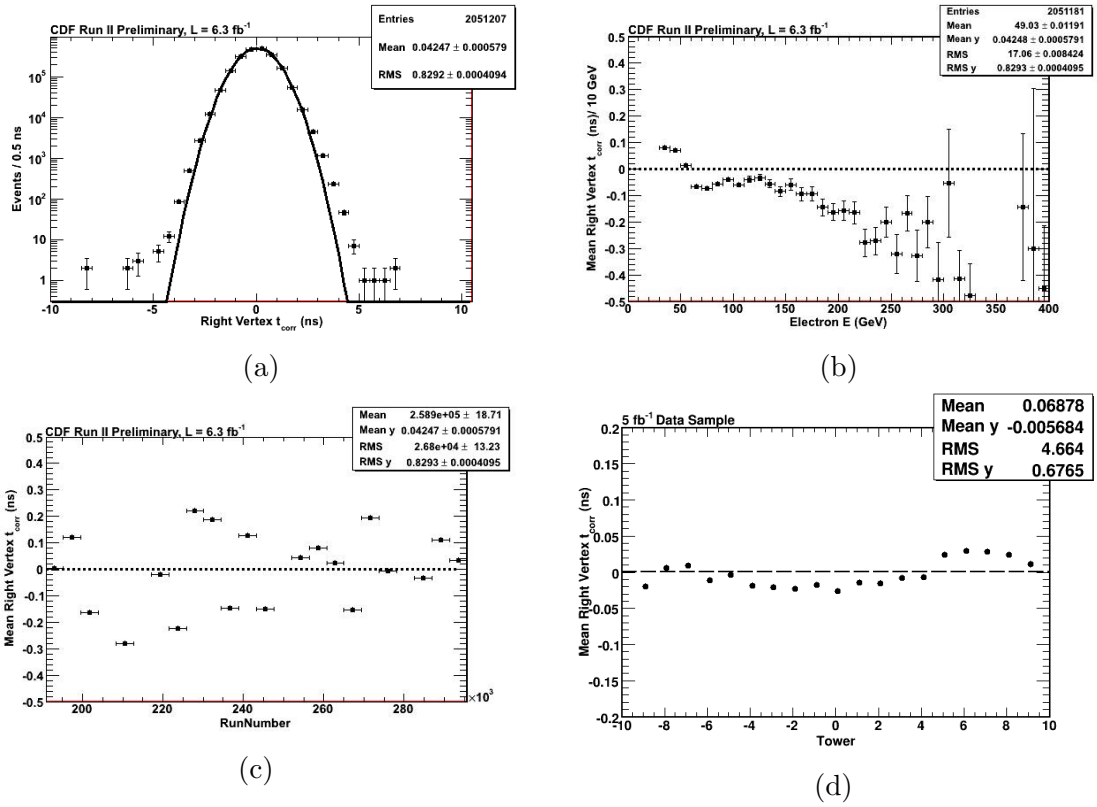

Figure A.7: (a) The uncorrected t_{corr} distribution. (b) The averaged uncorrected t_{corr} as a function of electron energy. (c) The averaged uncorrected t_{corr} as a function of run number. (d) The averaged uncorrected t_{corr} as a function of tower.

Each of these effects is fixed by selecting right-vertex events and generating a set of corrections as a function of electron energy, run number and tower, each in succession. We continue iterating through these three corrections until there are no deviations greater than 100 ps. The results of these corrections are shown in Figure A.8a. Figure A.9 shows the average t_{corr} after corrections as a function of vertex Z. This distribution is flat even though we did not calibrate as a function of

vertex Z which gives us confidence that our system is well calibrated and ready for use in searches.

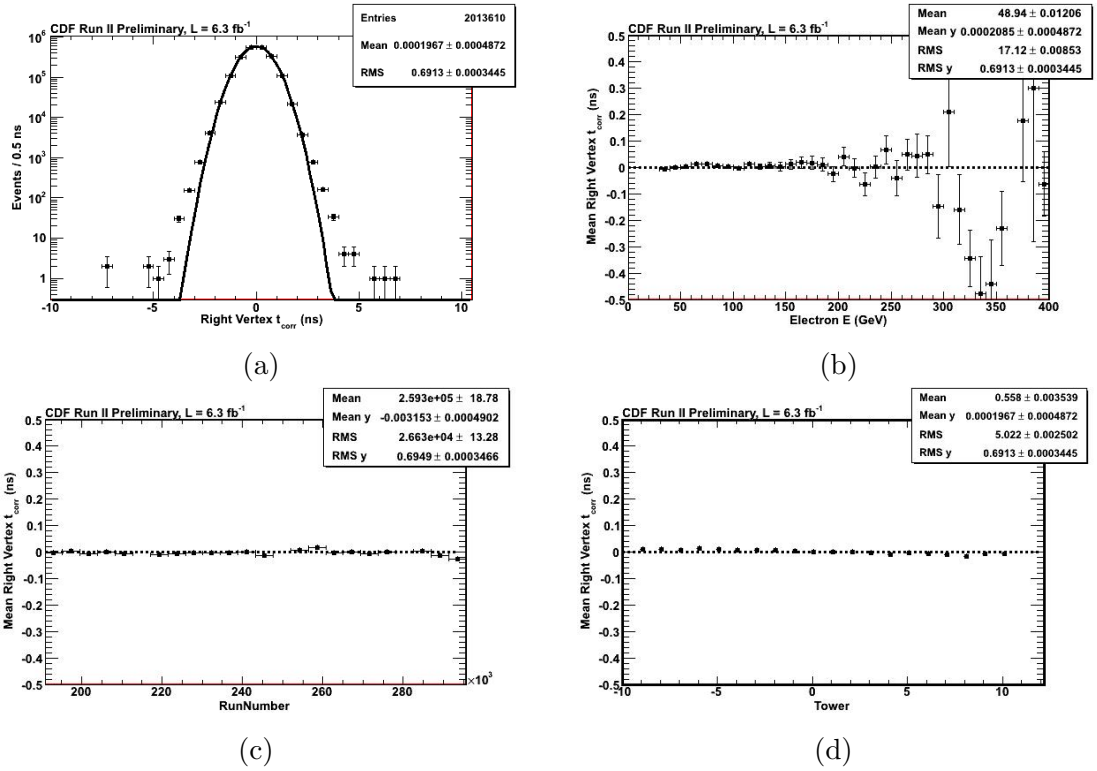

Figure A.8: (a) The corrected t_{corr} distribution. (b) The averaged corrected t_{corr} as a function of electron energy. (c) The averaged corrected t_{corr} as a function of run number. (d) The averaged corrected t_{corr} as a function of tower.

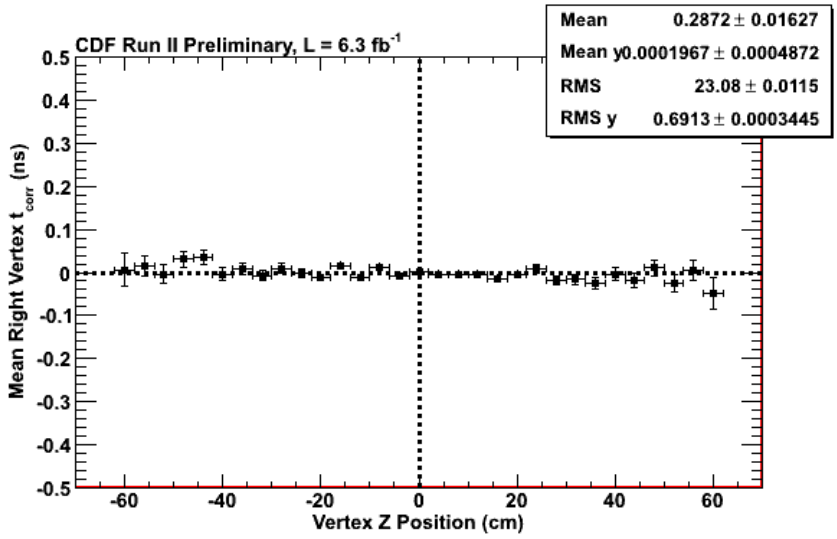

Figure A.9: The average corrected t_{corr} as a function of vertex Z.